

Sheffield Hallam University

Measurement of gas bubbles in a vertical water column using optical tomography.

IBRAHIM, Sallhuddin.

Available from the Sheffield Hallam University Research Archive (SHURA) at:

<http://shura.shu.ac.uk/19852/>

A Sheffield Hallam University thesis

This thesis is protected by copyright which belongs to the author.

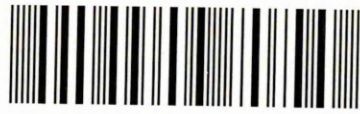
The content must not be changed in any way or sold commercially in any format or medium without the formal permission of the author.

When referring to this work, full bibliographic details including the author, title, awarding institution and date of the thesis must be given.

Please visit <http://shura.shu.ac.uk/19852/> and <http://shura.shu.ac.uk/information.html> for further details about copyright and re-use permissions.

LEARNING CENTRE
CITY CAMPUS, POND STREET,
SHEFFIELD S1 1WB.

101 651 881 1



REFERENCE

ProQuest Number: 10697158

All rights reserved

INFORMATION TO ALL USERS

The quality of this reproduction is dependent upon the quality of the copy submitted.

In the unlikely event that the author did not send a complete manuscript and there are missing pages, these will be noted. Also, if material had to be removed, a note will indicate the deletion.



ProQuest 10697158

Published by ProQuest LLC (2017). Copyright of the Dissertation is held by the Author.

All rights reserved.

This work is protected against unauthorized copying under Title 17, United States Code
Microform Edition © ProQuest LLC.

ProQuest LLC.
789 East Eisenhower Parkway
P.O. Box 1346
Ann Arbor, MI 48106 – 1346

**Measurement of gas bubbles in a vertical water
column using optical tomography**

Sallehuddin Ibrahim

A thesis submitted in partial fulfilment of the
requirements of
Sheffield Hallam University
for the degree of Doctor of Philosophy

November 2000



level 1

Dedication

To my beloved parents,

My late father Ibrahim and my mother Siti Hawa who made enormous sacrifice in order to educate and guide me.

To my beloved wife,

Nurul Ilm who was extremely patient and provided valuable ideas throughout my research.

To my brothers and sister,

Shaharuddin, Fauziah and Shahabuddin.

To my nieces,

Hafsah, Nadiyah, Nurul Najuwa and Muhammad Fauzi.

To my dearest friends,

Abdul Hameed, Arshad, Khairuddin, Pazir, Rashad, Sayid, Parviz, Salim, Zubair, Asil, Mahmud and others who provide a lot of motivation to me.

My appreciation to all of you for providing me assistance and encouragement throughout my research at Sheffield Hallam University.

Acknowledgements

I would like to express my deepest gratitude to my supervisors Professor Bob Green, Dr Ken Dutton and Dr Ruzairi for their invaluable guidance, excellent supervision as well as constructive criticisms throughout the research.

I would like to thank Mr Alan Goude who assisted in developing the hybrid reconstruction algorithm. My gratitude to Mr Brett Naylor who provided the inspiration for the lens forming temperature platform and to Mr Karl Evans who kindly checked my thesis.

Thanks also to the technicians Ken Duty, Brian Palmer, Richard Wainwright and David Allen who helped to construct the flow rig and the printed circuit boards.

The financial assistance from Universiti Teknologi Malaysia is greatly appreciated and without it this research could not have been carried out.

Abstract

This thesis presents an investigation into the application of optical fibre sensors to a tomographic imaging system for use with gas/water mixtures. Several sensing techniques for measurement of two component flow using non-intrusive techniques are discussed and their relevance to tomographic applications considered. Optical systems are shown to be worthy of investigation.

The interaction between a collimated beam of light and a spherical bubble is described. Modelling of different arrangements of projections of optical sensing arrays is carried out to predict the expected sensor output voltage profiles due to different flow regimes represented by four models. The four flow models investigated are: a single pixel flow, two pixels flow, half flow and full flow models.

The response of the sensors is based on three models: optical path length, optical attenuation and a combination of optical attenuation model and signal conditioning. In the optical path length model, opaque solids or small bubbles, which are conveyed, may totally or partially interrupt the optical beams within the sensing volume. In the optical attenuation model, the Lambert-Beer's Law is applied to model optical attenuation due to the different optical densities of the fluids being conveyed. The combination of optical attenuation model and signal conditioning is designed to improve the visual contrast of the tomograms compared with those based on the optical attenuation model.

Layergram back-projection (LYGBP) is used to reconstruct the image. A hybrid reconstruction algorithm combining knowledge of sensors reading zero flow with LYGBP is tested and shown to improve the image reconstruction. The combination of a two orthogonal and two rectilinear projections system based on optical fibres is used to obtain the concentration profiles and velocity of gas bubbles in a vertical column.

The optical fibre lens is modelled to determine the relationships between fibre parameters and collimation of light into the receiver circuit. Modelling of the flow pipe is also carried out to investigate which method of mounting the fibres minimises refraction of the collimated light entering the pipe and the measurement cross-section. The preparation of the ends of the optical fibre and design of the electronics, which process the tomographic data, are described.

Concentration profiles obtained from experiments on small bubbles and large bubbles flowing in a hydraulic conveyor are presented. Concentration profiles are generated using the hybrid reconstruction algorithm. The optical tomographic system is shown to be sensitive to small bubbles in water of diameter 1-10 mm and volumetric flow rates up to 1 l/min, and large bubbles in water of diameter 15-20 mm and volumetric flow rates up to 3 l/min. Velocity measurements are obtained directly from cross correlation of upstream and downstream sensors' signals as well as from upstream and downstream pixel concentration values.

Suggestions for further work on optical tomographic measurements are made.

Contents

DEDICATION	ii
ACKNOWLEDGEMENTS	iii
ABSTRACT	iv
CONTENTS	v

Chapter 1

Introduction.....	1
1.1 Process tomography.....	1
1.2 Multiphase and fluid flows.....	3
1.3 Aims and objectives of the thesis	5
1.4 Organisation of the thesis	6

Chapter 2

Brief review of tomographic sensors for fluid conveying.....	8
2.1 Electrical capacitance tomography.....	9
2.2 Electrical impedance tomography (special case ERT).....	10
2.3 Ultrasonic acoustic tomography	11
2.4 Nuclear magnetic resonance tomography	12
2.5 X-ray tomography	13
2.6 Gamma ray tomography	14
2.7 Positron emission tomography	16
2.8 Optical tomography	17
2.8.1 The proposed optical tomography system	18

Chapter 3

Mathematical Modelling	19
3.1 Introduction	19
3.2 Model for single spherical bubble	21
3.2.1 Bubble size	23
3.2.2 Moving bubble	36
3.3 Projection geometry	37

3.4	Optical path length model	40
3.4.1	Forward problem for the optical path length model	41
3.4.2	Inverse problem for the optical path length model	42
3.5	The optical attenuation model	42
3.5.1	Forward problem for the optical attenuation model	43
3.5.2	Inverse problem for the optical attenuation model	46
3.6	Models of flowing objects	46
3.6.1	Single pixel flow model	46
3.6.1.1	Path length model	47
3.6.1.2	Optical attenuation model	49
3.6.2	Two pixels flow model	51
3.6.2.1	Path length model	51
3.6.2.2	Optical attenuation model	53
3.6.3	Half flow model	54
3.6.3.1	Path length model	54
3.6.3.2	Optical attenuation model	56
3.6.4	Full flow model	57
3.6.4.1	Path length model	57
3.6.4.2	Optical attenuation model	59
3.7	Basic layergram back-projection technique.....	60
3.8	Modelling of optical fibre	64
3.9	Modelling of flow pipe	67
3.9.1	Light entering a transparent cylindrical flow pipe	68
3.9.2	Light entering a cylindrical flow pipe enclosed by a transparent perspex square	69
3.9.3	Light entering a hollow perspex square moulded onto the flow pipe	70
3.10	Cross correlation	71
3.11	Results of LYGBP using the path length model	74
3.11.1	Results for two orthogonal projections system	74
3.11.2	Results for a combination of two orthogonal and two rectilinear projections system	77
3.11.3	Results for three fan-beam projections system	78

3.12	Results of LYGBP using the optical attenuation model	78
3.12.1	Results for two orthogonal projections system	79
3.12.2	Results for a combination of two orthogonal and two rectilinear projections system	80
3.12.3	Results for three fan-beam projections system.....	81
3.13	Results of LYGBP using combination of optical attenuation model and signal conditioning	82
3.13.1	Results for two orthogonal projections system	82
3.13.2	Results for combination of two orthogonal and two rectilinear projections system	83
3.13.3	Results for three fan-beam projections system	84
3.14	Hybrid reconstruction algorithm	85
3.15	General discussion on the results obtained using the LYGBP and hybrid algorithms	87

Chapter 4

	The measurement system	92
4.1	Introduction	92
4.2	The light source	92
4.3	The receiving system	93
4.3.1	Preparation of the optical fibre	93
4.3.1.1	Polishing	93
4.3.1.2	Construction of lens	95
4.3.1.3	Emission pattern measurement	97
4.3.2	The receiver circuit	100
4.3.3	Calibration and tests on the receiver circuit	105
4.4	Design of the overall optical tomography system	108
4.5	The data acquisition system	109
4.6	The hydraulic flow rig	110

Chapter 5

	Concentration measurement	113
5.1	Introduction	113

5.2	Average concentration measurement	113
5.3	Concentration profiles	115
5.3.1	Concentration profiles of small bubbles	116
5.3.1.1	Flow rate of 0.5 l/min	116
5.3.1.2	Flow rate of 3 l/min	118
5.3.1.3	Flow rate of 5 l/min	118
5.3.1.4	Flow rate of 7 l/min	119
5.3.2	Concentration profiles of large bubbles	120
5.3.2.1	Flow rate of 0.5 l/min	120
5.3.2.2	Flow rate of 3 l/min	121
5.3.2.3	Flow rate of 5 l/min	122
5.3.2.4	Flow rate of 7 l/min	122
5.3.3	Concentration profiles of small bubbles at higher frequency ..	123
5.4	Discussion on concentration measurement	124
5.4.1	Gas flow rate calibration	124
5.4.2	Small bubbles	125
5.4.3	Large bubbles	127

Chapter 6

	Velocity measurements	128
6.1	Introduction	128
6.2	Sensor-to-sensor correlation	128
6.3	Pixel-to-pixel correlation	130
6.3.1	Pixel-to-pixel correlation on large bubbles	131
6.3.2	Pixel-to-pixel correlation on small bubbles	136

Chapter 7

	Conclusions and suggestions for future work	138
7.1	Conclusions	138
7.2	Contribution to the field of process tomography.....	139
7.3	Suggestions for future work	139

REFERENCES	145
------------------	-----

Publications relating to the thesis.....	150
APPENDICES	152
Appendix A Results obtained using LYGBP algorithm based on the path length model	153
Appendix B Results obtained using LYGBP algorithm based on the the optical attenuation model	156
Appendix C Results obtained using LYGBP algorithm based on combination of optical attenuation model and signal conditioning	159
Appendix D Tables of estimated reconstruction errors for two pixels flow, half flow and full flow models	163
Appendix E MATLAB program to reconstruct image using layergram back-projection.....	167
Appendix F C program for hybrid reconstruction algorithm	174

Chapter 1

Introduction

1.1 Process Tomography

Direct analysis of the internal characteristics relating to multicomponent flow in a process plant is vital in order to improve the design and operation of the production and control equipment. In such applications, the measuring instruments should employ robust, non-invasive sensors that can be used in aggressive and fast moving fluids and multi-phase mixtures [Beck, 1997].

Process tomography is a technique still in its infancy, but it has the potential for enabling great improvements in efficiency and safety in process industries, while minimising waste and pollution in a range of applications. It can be used to obtain both qualitative and quantitative data needed in modelling a multi-fluid flow system. In tomography, multiple projections are used to obtain sets of data from various views (typically, across a pipeline or a process vessel). These data are used to provide tomographic images representing the contents of the pipeline or vessel. The tomographic imaging of objects provides an opportunity to unravel the complexities of structure without invading the object [Plaskowski et al,1995].

Process tomography involves the use of instruments which provide cross-sectional profiles of the distribution of materials in a process vessel or pipeline. By analysing two suitably spaced images it is also feasible to measure the vector velocity profile [Abdullah et al, 1992]. From this knowledge of material distribution and movement, internal models of the process can be derived and used as an aid to optimising the

design of the process. This promises a substantial advance on present empirical methods of process design, often based on input/output measurements, with only a limited amount of information about the detailed internal behaviour of the process [Dickin, 1992].

Process tomography should enhance an understanding of particle dynamics for both steady and unsteady flow and further, assist in the validation of fundamental design equations through accurate determination of parameters such as phase mass flowrate and flow velocity. The spatial variation of solids concentration and velocity should be readily determined, along with concentration profiles as a function of concentration, particle size distribution and flow velocity [Bidin, 1993].

The operation and design of processes handling multi-component mixtures can be improved with the application of process tomography by enabling boundaries between different components in a process to be imaged, often in real-time using non-intrusive sensors [Beck et al, 1997]. Identification of phase sizes and boundaries within process vessels will provide significant information in the elucidation of fundamental reaction kinetics and for optimum geometric design of large-scale equipment. The advances in sensor technology and related computation can be combined with tomographic techniques in order to enhance component discrimination in complex process mixtures. For example, tomography can be used to distinguish the relative proportions as well as the velocities of oil, water and gas in a pipe bringing up oil from an undersea production well [Beck et al, 1997].

Information obtained from tomography will enable concentration, velocity and flowrate to be determined over a wide range of flow regimes by providing better averaging in time and space through multi-projections of the same observation [Abdul Rahim, 1996]. Tomography will provide an increase in the quantity and quality of information when compared to many earlier measurement techniques [Abdul Rahim, 1996].

1.2 Multiphase and fluid flows

Multiphase specifically refers to two or more phases of a substance, however, in the process industry it is used more generally to refer to mixtures of substances in the gaseous, liquid, or solid state. Hence air in water, or water in oil is called two phase flows [Dugdale, 1994]. The traditional approach to multiphase flow measurement has been to separate the mixture first, and then measure the individual components using conventional flowmeters. This solution may be both expensive and inconvenient. However, an industrial multiphase meter may currently cost £ 150,000.

Fluid flows are widespread in the oil industry, chemical engineering, energy and biological engineering, where the operating efficiency of such a process is closely concerned with flow regime [Fordham et al, 1999]. When two immiscible fluid components are mixed, the boundary between the phases is affected by the motion of the two fluids. The flow pattern generated as a result of the motion of the two fluids is a function of the velocity of the flow constituents, the viscosities of the components, and the dimensions and the cross-section of the flow pipe [Govier & Aziz, 1970]. The operating conditions in a fluid flow for various applications may vary widely. For example, the pressure can vary from as low as a few bar in water transportation, to as

high as up to 1000 bar in slurry conveying operations. Characteristics of the fluids may range from clean water to highly abrasive cement slurries, viscous gel suspensions, or erosive and dangerous chemical solutions. In such conditions, accurate measurement and on-line monitoring of processes are extremely difficult [Hou et al, 1999].

Offshore oil production platforms produce oil, water, gas and sediment in the form of a suspended multiphase mixture [Southern and Deloughry, 1993]. This mixture is fed to oil separation vessels to recover the oil and gas. Water and sediment are removed and can be returned to the environment when there is a minimum of oil contamination. This ensures maximum extraction of the oil and minimum pollution of the environment [Southern and Deloughry, 1993]. It is important that the sampling method employed to measure the percentage of water contained in the crude oil be as accurate as possible in order to optimise oil production and separation. This will reduce the operating cost and enable the early detection of faults in the process ensuring safer operation [King et al, 1983].

In measuring flowrate, the flowmeters which are currently available commercially cannot operate independently of the properties of the fluid [Hou et al, 1999]. Most of the meters require a homogenous mixture of components in the measurement section in order to obtain measurement stability and the required accuracy whereas in reality, it is usually impossible to obtain such a mixture, especially in horizontal or inclined pipes. Mixers are sometimes utilised in the pipes (one out of three in the market) but these result in a pressure drop [Hammer & Johansen, 1997]. Several types of meters are based on vertically upwards flows and utilise the natural mixing of such flows. However, at

high gas fractions, the gas bubbles tend to collect in the centre of the pipe resulting in measurement error [Hammer & Johansen, 1997].

The performance of turbine flowmeters can be seriously affected by the viscosity changes and the presence of solid particles in the flow. Similar degradation also happens when differential pressure instruments are used [Hou et al, 1999]. Electromagnetic flowmeters, which are widely applied, cannot be operated if the conductivity of the fluid drops below 10^{-4} S/m [Bevir, 1970]. As most sensors currently used in multiphase flowmeters are affected by the distribution of components in the mixture, tomographic imaging may possibly improve the accuracy and provide a wider measurement range.

1.3 Aims and objectives of the thesis

This project aims to investigate the use of tomographic measurement for on-line monitoring of gas bubbles or oil droplets having low concentration when being conveyed by a liquid. A typical example is the measurement of crude oil being discharged by tankers flushing their oil storage tanks. This project aims to combine the sensitivity of optical sensors with the area monitoring potential of process tomography.

The specific objectives of this thesis are to:-

- (1) Investigate the interaction between a collimated beam of light and a spherical bubble. Develop mathematical models of the optical system using optical path length and optical attenuation models.

- (2) Investigate a range of projections using the models from (1) and basing reconstructions on the layergram back-projection algorithm.
- (3) Investigate the use of a hybrid reconstruction algorithm using knowledge of sensors reading zero flow and the layergram back-projection algorithm.
- (4) Model and construct optical fibre lenses.
- (5) Specify, design and construct an optical tomography measurement system consisting of a combination of two orthogonal and two rectilinear projections.
- (6) Test this system on a hydraulic flow conveyor by injecting small and large gas bubbles into a water column and then determine the gas concentration profiles for a range of flow rates.
- (7) Investigate the use of sensor-to-sensor correlation and pixel-to-pixel correlation in order to obtain the velocity of gas bubbles flowing in water.
- (8) Consider the work presented in this thesis and provide suggestions for further research.

1.4 Organisation of the thesis

Chapter one presents an introduction to process tomography and multiphase flow.

Chapter two presents a brief review of several sensing mechanisms for use with fluid conveying such as capacitance, ultrasonic, nuclear magnetic resonance and optical tomography.

Chapter three presents an investigation on the interaction between a collimated beam of light and a spherical bubble. Modelling of the optical system is also described using the optical path length and the optical attenuation methods. Image reconstruction using the layergram back-projection and hybrid reconstruction algorithms is discussed. This is

followed by modelling of lensed optical fibres and includes a brief discussion on velocity measurement by cross correlation.

Chapter four discusses the design of the complete optical tomographic measurement system, including preparation of the optical fibre and design of the receiver circuit.

Chapter five presents results of concentration measurements for a range of gas volume flow rates.

Chapter six presents results of velocity measurement using sensor-to-sensor and pixel-to-pixel cross correlation.

Lastly, chapter seven discusses the conclusions to be drawn from this work and makes suggestions for future research.

Brief Review of Tomographic Sensors for Fluid Conveying

A process tomography system can be subdivided into three main sub-systems: the sensor, the data acquisition system and the image reconstruction and display (figure 2.1). The sensor is probably the most critical part. There are many sensing methods for tomography based on transmission and diffraction of sound and radiation, and electrical measurement. Several methods of sensing are discussed in this chapter.

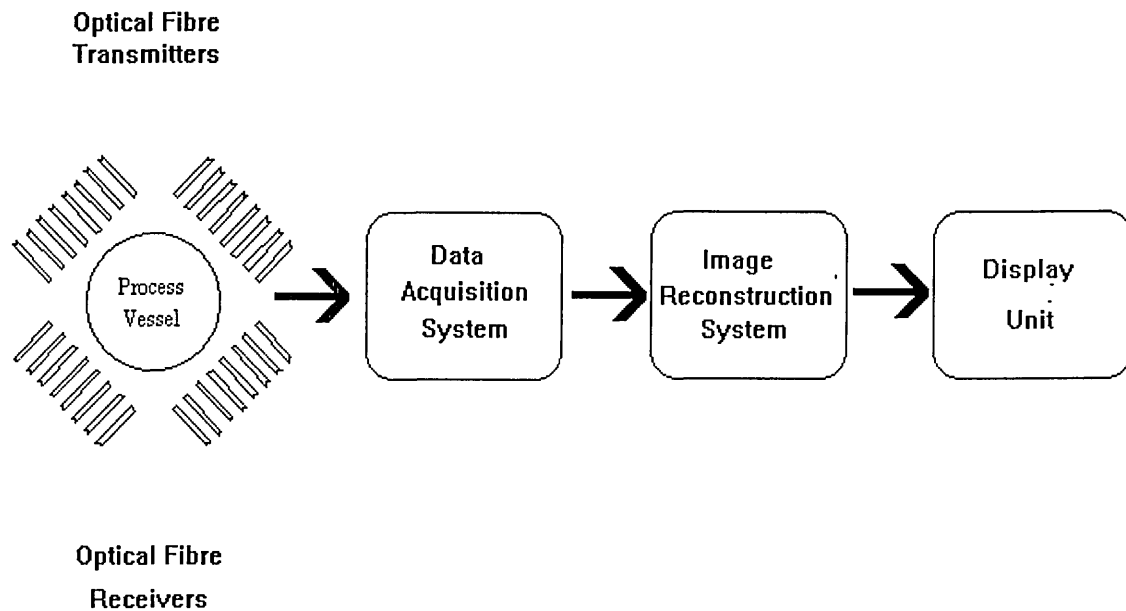


Figure 2.1 A process tomography system employing two arrays of optical fibre transducers

2.1 Electrical capacitance tomography

In an electrical capacitance tomography (ECT) system, a number of electrodes are mounted around the process of interest. These electrodes can be mounted either inside or outside the vessel depending on the wall material and the conveying fluid. The measured capacitance between two electrodes depends on the dielectric constant of the medium in between. The changes in the capacitive value are due to the variations in the permittivity of the material inside the process vessel [Beck et al, 1997].

ECT is suitable for imaging industrial multi-component processes involving non-conducting fluids, or mixtures of conducting and non-conducting fluids, where the major carrier is non-conducting, e.g. water droplets in oil, however it is difficult to obtain accurate quantitative information [Williams & Beck, 1995]. The electrode length required to provide measurable capacitances means that its resolution is limited and it results in 'smearing' and 'averaging' effects [Daniels, 1996]. It cannot produce meaningful images when the conveyed component loading decreases below approximately 5% due to the relatively low signal to noise ratio of the capacitance to voltage transducer and non-uniform sensing fields [Xie et al, 1992]. Its relatively low spatial bandwidth also restricts its application in velocity determination [Rahmat, 1996]. The number of independent readings obtained using ECT is small (less than 100) in existing capacitive systems because the electrode size cannot be decreased without limit, due to the field fringe effects [Isaksen and Nordtvedt, 1992]. However, Process Tomography Limited has produced many ECT system for the industry.

2.2 Electrical impedance tomography (special case ERT)

Electrical Impedance Tomography (EIT) generates a cross-sectional image of the impedance profile of a process. An electric field is produced if a potential difference is induced between two electrodes on the external boundary of a conductive medium. Other electrodes located around the boundary measure the intensity of this field which is a function of the impedance profile of the enclosed medium. The distinction between EIT and Electrical Resistance Tomography (ERT) is that the former uses both magnitude and phase components of the measured electrodes whereas the latter uses only the magnitudes [Daniels, 1996].

Generally, most projects have simplified the investigation to measurement of resistance. For example, Daniels [Daniels, 1996] investigated both the resistance and impedance of a conducting carrying fluid. In that project, the complex impedance was very much smaller than the resistive component of the circuit. Excitation sources for use with ERT systems are generally at frequencies below 5 MHz [Dyakowski, 1996].

The ERT technique is of great potential in industry process monitoring because of its advantages, such as visualisability, high temporal resolution, low cost, no radiation hazard, etc. ERT has been employed as a visualisation tool for mixing processes, multi-phase flow and aqueous-based separation in chemical engineering [Wang, 1999]. For example, it has been applied to measure solid concentration profile and stability of the air core in a 20 mm industrial separator [Williams et al, 1995], leakage detection from nuclear waste storage tanks [Daily et al, 1995], and gasoline plume imaging [Daily et al, 1995].

The accuracy of the technique is restricted by its complexity in sensor modelling and image reconstruction. The fact that the electrodes make electrical contact with the fluid limits the type of material from which they can be fabricated. The limited number of measurements and the presence of electrical noise cause difficulties in obtaining images. Additionally, the applied electrical fields are 'soft' so that complex (e.g. iterative) reconstruction algorithms may be needed to reduce image distortion. Compensation may be needed to increase sensitivity near the centre of the image [Dyakowski, 1996].

Several designs of ERT sensors have been adapted for different applications in the University of Manchester Institute of Science and Technology (UMIST). They comprise from one to eight sensing planes sized from 6 to 1500 mm in diameter. The ERT could achieve spatial resolution, conductivity resolution and distinguishability of 5%, 10% and 20% respectively for a system with a pre-error of 1% using an adjacent sensing strategy with a 16 electrode ring [Wang et al, 1997].

2.3 Ultrasonic acoustic tomography

Ultrasound waves are acoustic waves of the order of 1 to 100 MHz. Wherever there is an interface between one substance and another, the ultrasound wave is strongly reflected. Ultrasound has been successfully used for ocean tomography at the scale of hundreds of kilometres [Menemenlis et al, 1997].

Ultrasonic waves are difficult to collimate and problems occur due to reflections within enclosed spaces, such as metal pipes. The use of ultrasound to identify solids within sewage flows is restricted because the conveying liquid cannot be distinguished from

some of the solid material such as rubber and paper [Daniels, 1996]. Other problems arise due to the mismatch between the low acoustic impedance of the continuous (liquid) component of the flow and conventional piezoceramic material which results in significantly reduced performance of the transducer [Rahmat, 1996]. It may produce erroneous results if not used properly, since reflection and/or diffraction effects may dominate, depending on the properties of the object being interrogated and on the operating frequencies of the ultrasonic waves.

An ultrasound reflection tomographic system with a circular array of 36 transducers which can generate reconstructed images at an average of 30 frames per second has been developed. To achieve this speed of image reconstruction intensive use of processing resources was required. The system has a resolution of 100×100 pixels [Schlaberg et al, 1997].

2.4 Nuclear magnetic resonance tomography

The Nuclear Magnetic Resonance Tomography (NMRT), also called magnetic resonance tomography, is widely used in medicine for diagnostic purposes and has also been applied in process and biochemical engineering. In NMRT, an external magnetic field is imposed on the atomic nuclei. This will result in the oscillation of the nuclei due to their magnetic nature. The relationship between the magnetic field and the frequency of the nuclei oscillation can be expressed as :-

$$\omega = \gamma \beta$$

in which $\omega = 2 \pi f$

f = the Larmor frequency (Hz)

γ = magnetogyric ratio ($\text{rad T}^{-1} \text{s}^{-1}$)

β = the strength of external magnetic field (T)

The main advantage of NMRT is its specificity to chemical composition and the high resolution of images obtained. Problems can arise in applying NMRT directly to the process industry due to sensor volume and its inability to function if significant quantities of iron are present. The sensors also have a slower dynamic response and are more complicated to manufacture compared to the sensors used in electrically-based tomographic techniques such as resistive and capacitance tomography. In addition, the cost of the NMRT system is expensive due to the cost of magnets and presently it is only suitable for laboratory investigations and not suitable for imaging flows in large process vessels or pneumatic conveyors [McKee, 1995].

In two-phase flow measurements, there has been a lot of research applying NMRT in investigating solid-fluid suspensions, where there is a need to understand suspension rheology and flow-induced microstructural changes [Gladden and Alexander, 1996]. For example, non-uniform velocity and concentration distributions have been reported for suspensions of small, negatively buoyant particles suspended in a 80 W gear lubricant oil of density 0.875 gcm^{-3} and flowing in a horizontal acrylic plastic tube of inside diameter 2.54 cm and length 1.82 m [Altobelli et al, 1991].

2.5 X-Ray tomography

X-ray transmission tomography is widely used in diagnostic medicine, but it is bulky and the presence of its ionising radiation is dangerous. Images of a section or thin slices

through an object at different depths are obtained by carefully computed and controlled relative motion of the X-ray source and the detector during the exposure. This technique is known as computerised tomography (CT).

Heavy shielding is required for safety and to collimate the beam. As such, it is not a suitable tool for flow imaging in an industrial setting [Williams & Beck, 1995]. It is also bulky, expensive and not suitable for real-time industrial processes, but it does offer a very high resolution. The slow rate of data acquisition associated with conventional X-ray systems makes them unsuitable for flow visualisation.

An x-ray tomography system consisting of a 60 keV x-ray source and an x-ray detector has been developed to investigate flow structures of circulating fluidized beds. The system can measure average solids concentration up to 20 Vol-% in a tube with 0.19 m inner diameter with a minimum spatial resolution of 0.2mm. The results obtained are reliable within an error range of about 5% [Grassler et al, 1999].

2.6 Gamma ray tomography

Gamma ray tomography is based on the measurement of the attenuation of photon beams traversing in various directions through an object. The gamma ray densitometer has been increasingly used in the oil industry to determine flow regime and void fraction [Abro et al, 1999]. The transmitted gamma rays are usually detected by a scintillation counter or a lithium germanium detector. The following formula describes the attenuation of gamma rays

$$I = I_0 e^{-\mu N}$$

where

I = transmitted intensity (Wm^{-2})

I_0 = initial incident intensity (Wm^{-2})

N = thickness of the absorbing material (m)

μ = linear absorption coefficient (m^{-1})

The transmitted signal is heavily dependent on the flow regime because of the narrow beam (compared with the pipe diameter) utilised in these densitometers. This can probably be solved by using a multi-detector system. The frequency response is quite poor (typically 0.05 Hz) due to the required counting statistics needed for the detector to obtain accurate measurement of the transmitted beam intensity. The frequency response can be increased by increasing the source intensity and a frequency response of 50 Hz can be obtained with a reduction in counting statistics frequency [Hammer, 1983]. However, careful screening and handling have to be implemented for high intensity gamma radiation source.

A gamma-ray tomography system with five radiation sources and eighty-five compact detectors has been used to discriminate between the gas and liquid phases for an 82mm inner diameter perspex pipe. The system is used along with an 8-electrode capacitance tomography system (used to distinguish between oil and water) as part of a dual mode tomograph for three-component flow imaging [Johansen et al, 1994]. Another multi-beam gamma-ray tomography system with four detectors has been used to determine the void fraction in two- and multi-phase pipe flows in an aluminium pipe having an inner and outer diameter of 80mm and 90mm respectively. The system which made use of a

neural network trained by simulated data was able to determine the void fraction with an average error of 3 % [Abro et al, 1999].

2.7 Positron emission tomography

In positron emission tomography (PET), tracer species are added into the process under investigation. These tracers emit an appropriate and detectable signal to the sensor(s) installed at the periphery of the vessel. A function of position and time in relation to the emitters is obtained from external coincidence measurements. The fundamental measurement is the coincidence detection of two almost anti-parallel photons, which are emitted due to the annihilation of a positron with an electron. The imaging systems make use of either circular geometry, with rings of sensors around the flow to be imaged, or position sensitive detectors, such as gamma cameras or multiwire proportion chambers. The use of positron-emitting radiolabels for flow imaging in engineering studies has been pioneered at the University of Birmingham [Clarke et al, 1997].

The advantage of PET imaging is that it pinpoints the locations of individual particles in the medium, and not bulk masses as in X-ray tomography. The drawbacks include health hazards which arise from the use of radioactive isotopes needed to produce the positron emissions as well as the cost and the size of the detectors. Although a major strength of positron-based imaging is that studies can be performed on actual plant, provided sufficient access is possible for the detection equipment, to date its application has been restricted to that of a research tool, rather than for process monitoring, mainly due to the capital cost of current positron cameras.

A PET system has been developed to follow the trajectories of individual particles in a laboratory-scale jig. The system employs two detectors. The jig has a dimension of $150 \times 100 \times 250$ mm and contains more than 300,000 particles [Clarke et al, 1997].

2.8 Optical tomography

Optical tomography is an attractive method since it is conceptually straightforward and relatively inexpensive, has a better dynamic response and can be more portable for routine use in process plant than other radiation-based tomographic techniques such as positron emission, gamma photon emission and X-ray tomography [Hartley et al, 1992]. It is better than many other approaches to tomographic imaging by dint of being an active, linear system whose reconstructed images should relate directly to visual images seen in transparent sections of the process vessel. It has negligible response time relative to the process variations, has high resolution due to its small wavelengths, and emitters and detectors which have good immunity to electrical noise and interference are readily available [Jackson, 1995]. It makes use of the 'hard field' sensor principle, which is similar to gamma ray tomography in which the sensing field is based on the measurement of the attenuation or absorption of radiation. Optical fibre sensors provide a very wide bandwidth which enables measurements to be performed on high speed flowing particles.

Three methods of detecting particles can be used: light absorption, light attenuation and light scattering. Scattering of light is complex to describe mathematically due to the random positioning of the particles responsible [Daniels, 1996], but absorption and attenuation may be quantified by relatively simple mathematical models (sections 3.3

and 3.4). Absorption occurs when incident light energy passes through a medium and is converted to heat causing attenuation; some materials exhibit selective absorption to specific frequencies of light [Daniels, 1996]. Attenuation arises because opaque material interrupts the beam. Different materials cause varying levels of attenuation and scattering and it is this fact that forms the basis of optical tomography [Daniels, 1996]. For bigger particles i.e. equal to and greater than 1 μm , light extinction is employed when the detector is aligned directly into the light source and the size of the particle shadow is measured as it crosses the light path. For particles less than 1 μm , light scattering is employed in which the detector looks at the light ray from the side of the flow channel [HIAC-ROYCO, 1998]. In both methods of detection, the fluctuation in the light intensity is measured by the detector and converted to an electrical signal.

2.8.1 The proposed optical tomography system

This project aims to investigate the use of optical fibre detectors arranged in multiple projections around a vertical transparent flow pipe for measurement of gas bubbles being conveyed by water. Light is injected through the measurement section and detected by fibre optic sensors, which transfer the light energy to photodiodes. These provide an electrical output, which is amplified, signal processed and fed to a PC for further analysis. The sensors measure the changes in absorption or attenuation of the conveyed material and information obtained in this way allows an image of the cross-section of the flow to be reconstructed by a computer. Details of the optical tomographic measurement system are described in chapter four. The next chapter investigates a series of possible optical projection arrays, two methods of optical modulation and four flow models.

Chapter 3

Mathematical Modelling

3.1 Introduction

Modelling is carried out to predict the spatial and temporal behaviour of a process and it becomes more significant as the inherent complexity of a process increases [Mann, 1995]. Generally, the following three important stages are involved in sensor modelling [Khan et al, 1995].

- (a) Identify the mathematical model of the sensor, and determine the governing equations and associated boundary conditions.
- (b) Establish the geometric model of the sensor taking into consideration the significant aspects and special features of the problem domain so as to minimise the amount of data.
- (c) Choose an efficient numerical method (discretisation scheme) so as to realise a computer solution of the problem.

In practice, several projections are needed to reduce aliasing which occurs when two particles intercept the same view [Nordin, 1995]. The forward problem for the individual sensors is modelled to solve the inverse problem and derive the layergram back-projection algorithm [Rahmat, 1996].

Modelling is carried out based on 2 parameters affecting the measured output of the sensor:-

- (a) Optical attenuation due to changes in optical density within the pipeline.

(b) Path length of the sensing beam within the pipeline projections [Burns, 1994].

In a gas/liquid system for large bubbles, when the incident beam passes through the centre of the bubble, the major effect is optical attenuation, because the bubble, being gas, attenuates the optical energy less than water. In this model, the measurement section consists of a square, thin walled clear plastic section containing water (figure 4.15a). The plastic wall is 2mm thick and is neglected in all the following calculations. The path length between the incident beam entering the measurement section to the receiver is 100mm. The path length for the beam when no gas bubble is present is 80mm in water (ie water in pipe of diameter 80mm) and 20mm in air (the length of the aperture stop) (figure 4.15a). The output beam is attenuated according to Lambert-Beer's law,

$$V_m = V_{in} \exp[-\alpha_w l_w - \alpha_a l_a]$$

where:

V_m = voltage of the receiving sensor (V)

V_{in} = voltage of the receiver when no gas bubble present (V)

α_a = absorption coefficient of air (mm^{-1})

α_w = absorption coefficient of water (mm^{-1})

l_a = path length of air (mm)

l_w = path length of water (mm)

l_b = path length through bubble (mm)

and $l_w + l_a = 100$ mm.

When a bubble is present in the path, then $l_a = l_b + 20$ (mm) where l_b is the path length through the bubble and the path length in water l_w becomes $l_w = 80 - l_b$ (mm).

Hence,

$$V_m = V_{in} \exp[-(80-l_b)\alpha_w - (20+l_b)\alpha_a] \quad (3.a)$$

However, in general, the interaction between the beam of light and a spherical bubble involves reflection, refraction and optical attenuation [Dugdale, 1994].

The optical path length model was originally developed for solid, opaque particles [Abdul Rahim, 1996]. He showed empirically that the output voltage from an optical fibre sensor was proportional to the optical path length of the sensor within the conveyor and the volume flow rate of uniformly distributed solids. As the bubble size decreases and reduces the amount of light it directly transmits, it behaves in a similar manner to the solid particle i.e. it prevents light energy arriving at the sensor.

However, small bubbles (say 2mm or less in diameter (section 3.2.1)) will often reflect or refract the optical beam away from the receiver completely. In this case the system is similar to the path length model. The overall model should combine both principles (see chapter seven). In previous projects, Abdul Rahim [Abdul Rahim, 1996] concentrated on the path length model whereas Ramli [Ramli, 1998] focussed effort on the optical attenuation model. This project investigates both models, which enables a comparison between the performance of both methods to be made.

3.2 Model for single spherical bubble

This section investigates how the position and size of a single gas bubble will affect the amount of light energy being received by the detector. The incident light consists of a 1mm collimated beam, which travels 100mm between source and detector (which consists of a 1mm diameter sensor).

When a collimated beam of light is directed through a medium, the reduction in the intensity of the beam is due to absorption, scattering and dispersion. All media show absorption, some absorb all wavelengths equally (general absorption), others show selective absorption. Lambert Beer's law states that equal paths in the same absorbing media absorb equal fractions of the radiation that enters them. The scattering of light by a bubble that is large compared to its wavelength, consists of a mixture of diffraction, diffused reflection (reflection in all directions) and refraction. Scattering from a cloud of such bubbles is independent of wavelength, unlike the scattering of light by very small bubbles (Rayleigh scattering) [Dugdale, 1994] which is proportional to the square of the bubbles' volume and $1/\lambda^4$. Since gas/liquid flow regimes involve bubbles with dimensions much larger than the wavelength of radiation incident on them, the majority of attenuation is caused by wavelength independent scattering [Dugdale, 1994].

Interfaces between phases can present many boundaries in the path of the radiation. On crossing such boundaries Fresnel [Jalie, 1977] has shown that the fraction of radiation reflected at normal incidence, irrespective of polarisation is ρ where

$$\rho = \left[\frac{n' - n}{n' + n} \right]^2$$

where n is the refractive index of the first medium and n' the refractive index of the second. Thus for water and gas

$$\rho = \left[\frac{1 - 1.33}{1 + 1.33} \right]^2 \approx 0.02 \text{ or } 2 \%$$

At the other extreme when light is incident at the polarising angle, 15% of the component perpendicular to the plane of incidence is reflected and none of the parallel component [Longhurst, 1967].

All the optical processes described above play a part in attenuating the radiation so a method of predicting their combined effect is useful in determining the response to be expected when measurements are made in gas/liquid flows. The following section describes several models relating to a single spherical bubble.

3.2.1 Bubble size

The model of two phase flow starts with the case of a single gas bubble moving vertically up the pipe of the laboratory flow rig. The effect of the size and position of the bubble on the transducer in the measurement cross-section is to be determined. This section investigates the effect of a spherical gas bubble in water when a collimated beam of light, 1 mm in cross section, is incident on it. Four conditions are considered :-

- (i) bubble diameters greater than 1.33 mm diameter and the light beam passing through the optical centre of the bubble (no total internal reflection).
- (ii) bubble diameter between 1.33 mm and 1 mm diameter and the light beam passing through the optical centre of the bubble (outer edge of incident beam attenuated by total internal reflection).
- (iii) bubble diameters less than 1 mm diameter and the light beam passing through the optical centre of the bubble.
- (iv) bubble of various diameters and the light beam off the principal axis.

For all these cases, the bubble acts effectively as a gas lens in water. Since the bubble is spherical it must be considered as a thick lens [Tunnecliffe & Hirst, 1981]. A gas bubble in water behaves as a diverging lens (figure 3a.2) when a beam of light passes through it. For a thin diverging lens, a beam of light parallel to the principal axis, appears to come from the principal focus of the lens after refraction. A spherical gas bubble in

water forms a thick diverging lens. To analyse how collimated light is refracted by the bubble, it is convenient to determine the equivalent thin lens power and equivalent thin lens focal length of the bubble. The model (figure 3a.1) allows the equivalent thin lens power/focal length to be calculated.

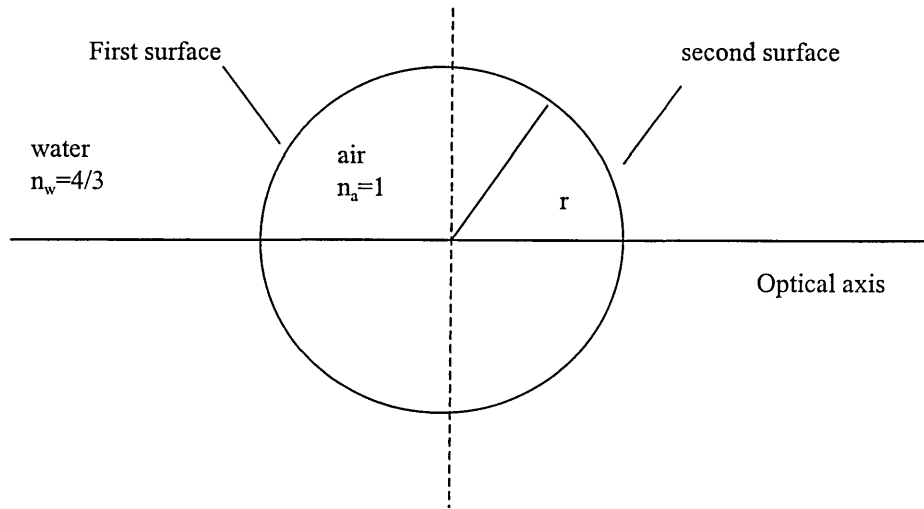


Figure 3a.1 The bubble as a thick lens.

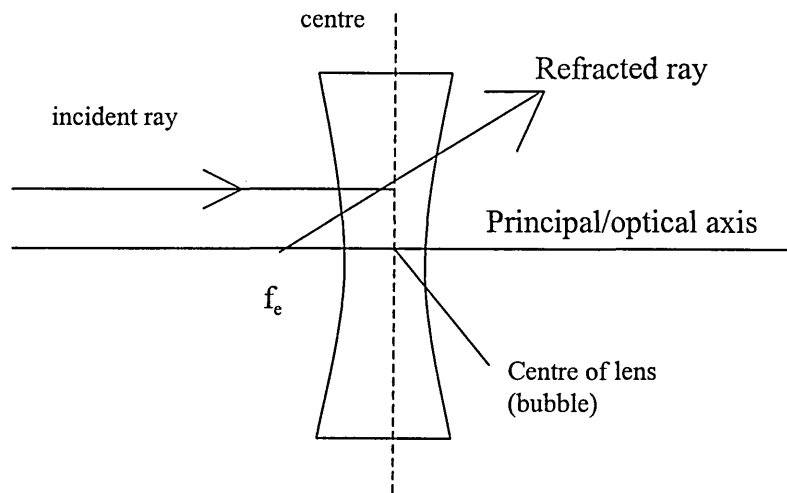


Figure 3a.2 Equivalent thin lens

The focal length, $f(m)$, and the power of a spherical surface F (dioptries) [Tunnecliffe & Hirst, 1981] is

$$\frac{1}{f} = F = \frac{n_2 - n_1}{r}$$

where n_2 is the refractive index of the second medium, n_1 the refractive index of the first and r is the radius of the bubble.

For the first surface,

$$F_1 = \frac{n_a - n_w}{r} = \frac{1 - 4/3}{r} = -\frac{1}{3r} \text{ (it has a diverging power)}$$

Using the sign convention shown in Tunnecliffe & Hirst [Tunnecliffe & Hirst, 1981],

$$F_2 = \frac{n_w - n_a}{-r} = \frac{4/3 - 1}{-r} = -\frac{1}{3r} \text{ (also diverging)}$$

The equivalent thin lens power, F_e , is

$$F_e = F_1 + F_2 - tF_1F_2$$

where t is the axial separation between the first and second surfaces.

$$F_e = -\frac{1}{3r} - \frac{1}{3r} - \left[2r \left(-\frac{1}{3r} \right) \left(-\frac{1}{3r} \right) \right] = -\frac{8}{9r}$$

The equivalent thin lens focal length, f_e , is

$$f_e = 1/F_e = -9r/8 = -1.125r \quad (3.b)$$

The thin lens is positioned at the centre of the bubble [Tunnecliffe & Hirst, 1981], so the equivalent thin lens focal point lies $1.125r$ to the left of the centre of the bubble (figure 3a.3).

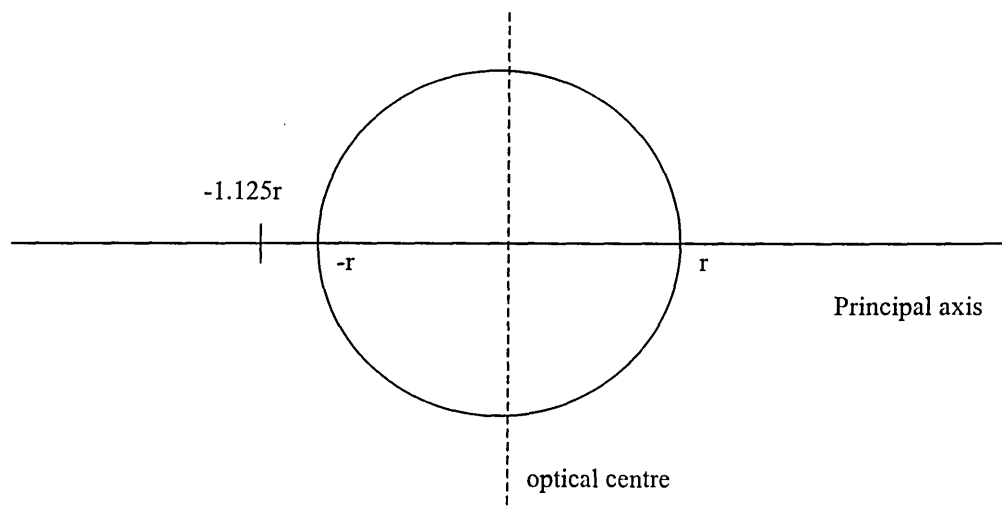


Figure 3a.3

Now consider rays passing through the bubble. All the incident beams are 1mm in cross-section (because of the system design (section 4.4)) and are parallel to the principal axis of the bubble. For a diverging lens, a ray initially parallel to the principal axis appears to come from the equivalent thin lens focal point (figure 3a.4).

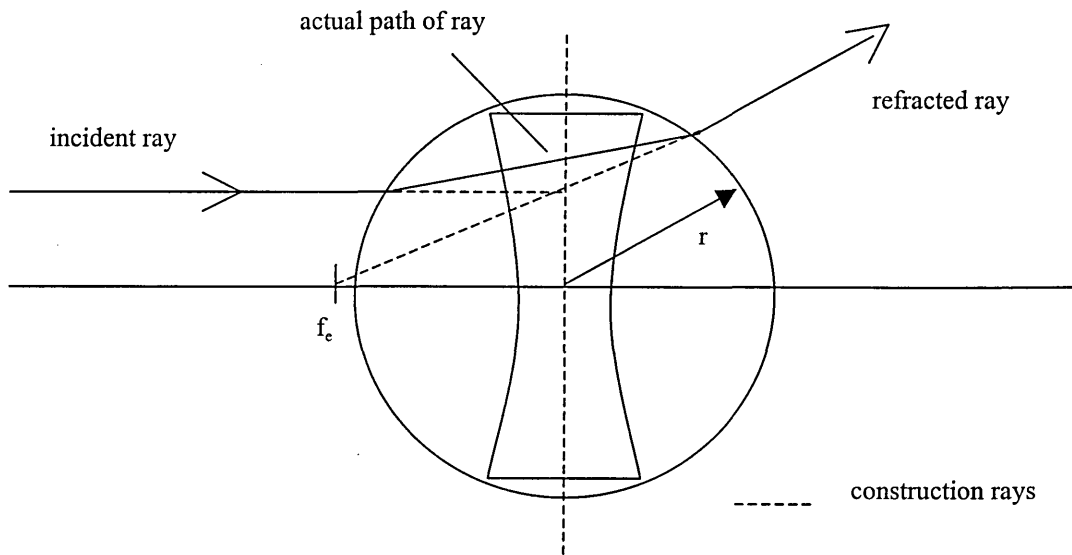


Figure 3a.4 Refraction by a bubble

This construction is important, because all the light rays entering the bubble with the optical system used in this thesis must be parallel to the principal axis.

The optical system used in this thesis is arranged to accept collimated beams of 1 mm diameter. The sensor spacing of 8mm, combined with the aperture stop, prevents light beams that arrive at the conveyor exit wall (figure 3a.5) which have been deviated through an angle θ_a (greater than 2.9°) from the principal axis from entering the sensor, because of the geometry of the aperture stop, which is 1mm in diameter by 20mm long. The acceptance angle of the stop is

$$\theta_a = \tan^{-1} \frac{1}{20} = 2.9^\circ \quad (3.b.1)$$

From figure 3a.5, for the light beam, initially incident at sensor 2, to be refracted to reach the aperture containing sensor 1 it must be deviated by a minimum of

$$\theta = \tan^{-1}(8/80) = 5.7^\circ$$

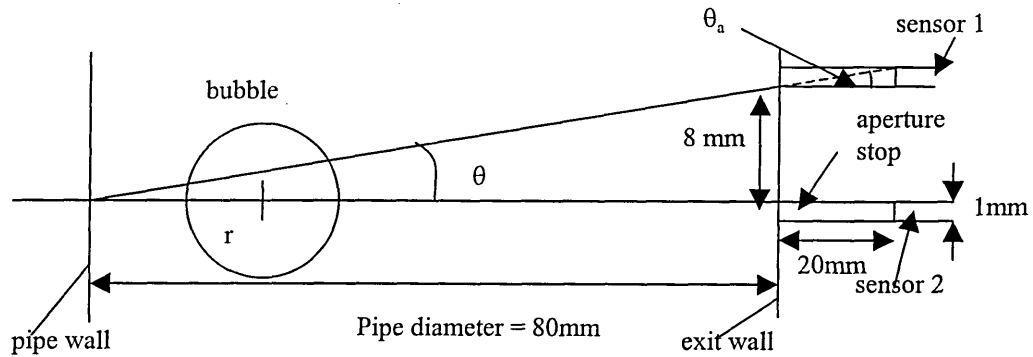


Figure 3a.5 Angular deviation of beam by refraction

For all bubbles, when the angle of the incident ray to the bubble reaches the critical angle, θ_c , the ray is totally internally reflected (figure 3a.6). Total internal reflection occurs when a light ray goes from an optically more dense medium (water) to an optically less dense medium (air) [Tunnecliffe & Hirst, 1981]. At the critical angle, part of the incident beam is refracted and passes along the surface of the interface just inside the bubble and the remainder of the incident beam is reflected. When the incident angle exceeds the critical angle, all the light is reflected (total internal reflection) [Tunnecliffe & Hirst, 1981].

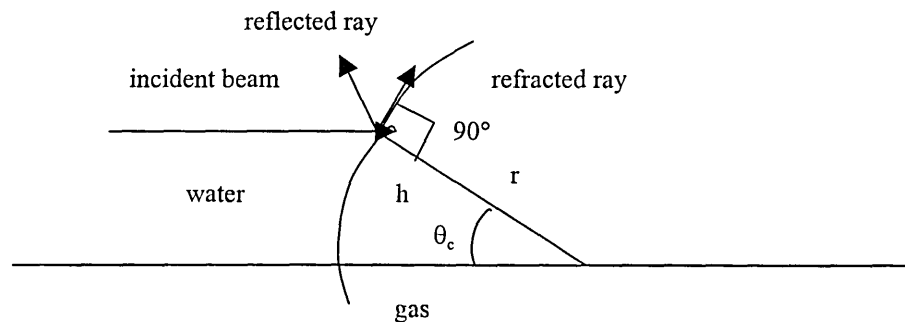


Figure 3a.6 Total internal reflection at the surface of the bubble

According to Snell's law, $n_w \sin \theta_c = n_a \sin 90^\circ$

where n_w = refractive index of water = $4/3$ and n_a = refractive index of air = 1 .

Hence, $\sin \theta_c = 1/n_w = 3/4 = 0.75$. $\theta_c = 48.6^\circ$ (3.c)

Also, in terms of the bubble radius, $\sin \theta_c = h/r = 0.75$. Hence, $h = 0.75r$.

If $h=0.5$ mm, $r= 2/3$ mm and the diameter of the bubble is $2r = 4/3 = 1.33$ mm.

This means that for the 1mm diameter incident beam if the bubble is centred on the beam and greater than 1.33mm in diameter the beam will not suffer total internal reflection from the surface of the bubble.

Case (i) : Bubble amplitudes greater than 1.33 mm diameter and the light beam passes through the optical centre of the bubble

Now consider case (i) where the diameter of the bubble is greater than 1.33 mm and the light beam passes through the optical centre of the bubble (figure 3a.7). For these bubbles no total internal reflection occurs.

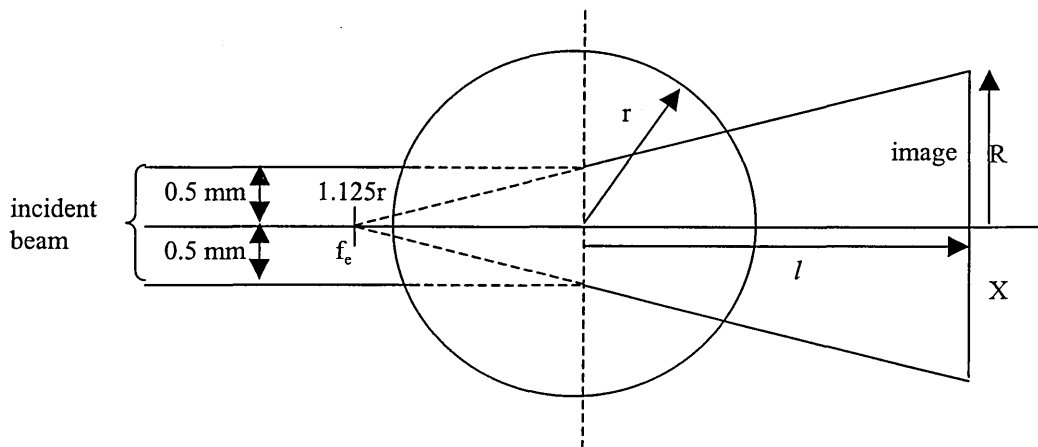


Figure 3a.7 Refraction of beam

Neglecting losses due to reflection, the energy in the incident beam at X is now spread over an area πR^2 . By similar triangles,

$$\frac{1.125r}{1.125r + l} = \frac{0.5}{R}$$

$$R = \frac{0.5(1.125r + l)}{1.125r}$$

Then the ratio of initial beam area to final beam area equals the fractional loss of intensity due to refraction (δr).

$$\delta r = \frac{\pi 0.5^2}{\pi R^2} = \frac{0.5^2 (1.125r)^2}{0.5^2 (1.125r + l)^2} = \left[\frac{1.125r}{1.125r + l} \right]^2$$

The loss of intensity at each air/water boundary, assuming normal incidence is 2%. For a single bubble there are two boundaries. So the correcting factor due to crossing boundaries is $\delta b = 0.96$. (It should be noted that some of the incident beam will not strike the bubble normally, so more light energy than 2% will be lost by reflection. This change in loss will depend upon bubble size but is neglected in this model.)

For the change in absorption due to the path lengths in water (l_w) and air (l_a) refer to figure 3a.8.

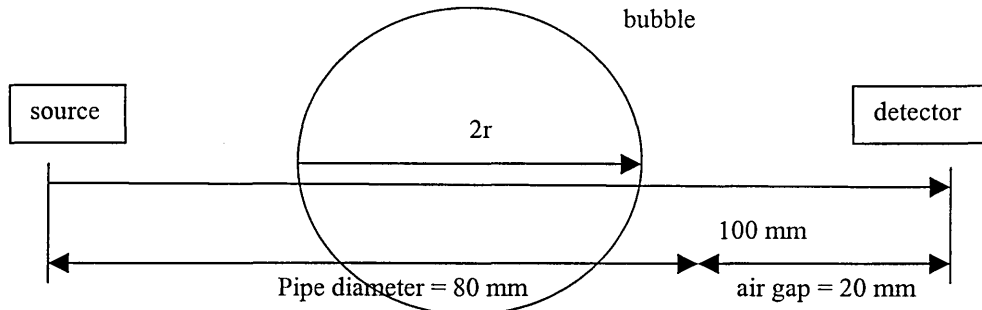


Figure 3a.8 Absorption path lengths

The intensity due to path length absorption, I is related to the initial intensity I_0 by,

$$I = I_0 \exp[-\alpha_w l_w - \alpha_a l_a]$$

Where α_a and α_w are absorption coefficients of air and water. From experimental work [Dugdale, 1994], these were found to be 0.0142/mm and 0.0287/mm respectively. So

the detected intensity if the beam travels 100 mm between source and detector (80mm in water and 20mm in air) (figure 3a.8 and figure 4.15a) as on the flow rig is,

$$I = I_0 \exp -(80 \times 0.0287 + 20 \times 0.0142) = 0.0758 I_0$$

This is the initial intensity at the sensor as a fraction of the radiation from the source when no bubble is present.

The correcting factor for the decrease in absorption caused by a bubble of radius r is,

$$\delta a = \frac{I_0 \exp -(0.0287l_w + 0.0142l_a)}{0.0758I_0}$$

but $l_a = 2r + 20$ and $l_w = 80 - 2r$.

Hence, $\delta a = 13.2 \exp -[0.0287(80 - 2r) + 0.0142(2r + 20)] = 13.2 \exp -(2.58 - 0.029r)$

The ratio of the detected intensity to the emitted intensity for case (i) is,

$$\begin{aligned} \frac{I_d}{I_e} &= \delta r \times \delta b \times \delta a = \left[\frac{1.125r}{1.125r + l} \right]^2 (0.96)(13.2 \exp -[2.58 - 0.029r]) \\ &= 12.67 \left[\frac{1.125r}{1.125r + l} \right]^2 \exp -(2.58 - 0.029r) \end{aligned}$$

Thus the fraction of the original beam arriving at the sensor is a function of both bubble size, r , and the distance between the exit wall and the centre of the bubble, l .

The graph in figure 3a.9 shows the relative intensity I_d/I_e of bubbles of various radii for various values of l for case (i).

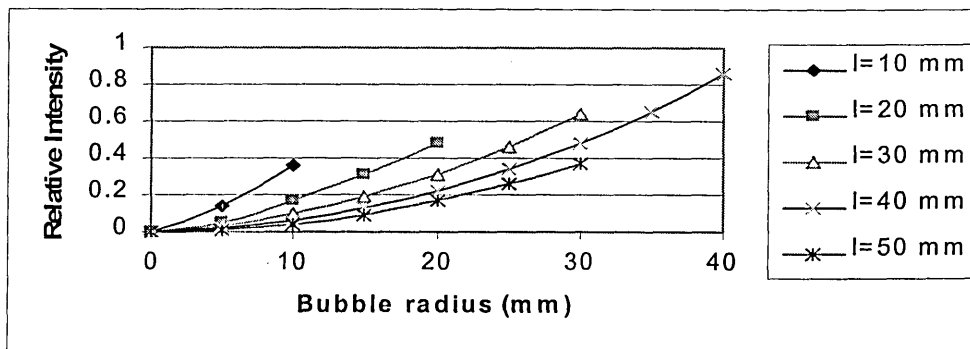


Figure 3a.9 Relationship between relative intensity, bubble radius and bubble position

Case (ii): Bubble amplitude between 1.33mm and 1mm diameter and the light beam passes through the optical centre of the bubble (outer edge of incident beam attenuated by total internal reflection)

For bubbles between 1.33 mm and 1 mm in diameter (case (ii)), refer to figure 3a.10, the edges of the bubble produce total internal reflection.

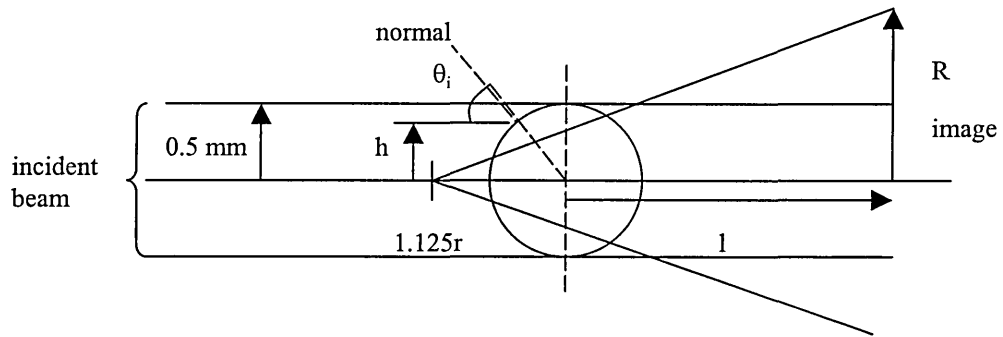


Figure 3a.10 Beam spread by a 1 mm diameter bubble

So when the bubble diameter equals the beam diameter, from (3.b),

$$f_c = 1.125r = 1.125 \times 0.5 = 0.5625.$$

From equation (3.c) and figure 3a.10, for the critical angle, θ_i ,

$$\sin \theta_i = 3/4 = h/0.5. \text{ Hence, } h = 0.375 \text{ mm.}$$

Parts of the beam between $r=0.375\text{mm}$ and $r=0.5\text{mm}$ are totally internally reflected and cannot arrive at the sensor. The part of the incident beam where r is less than 0.375mm passes through the bubble and is refracted.

$$\text{Then, by similar triangles, } R / 0.375 = (1.125 \times 0.5 + l) / 0.5625.$$

$$R = (1.125 \times 0.5 + l) 0.375 / (1.125 \times 0.5) = 0.67 (0.5625 + l)$$

The fractional loss of intensity due to refraction (δr) is

$$\delta r = \frac{\pi 0.5^2}{\pi R^2} = \frac{\pi 0.5^2}{\pi [0.67(0.5625 + l)]^2} = \frac{0.56}{(0.5625 + l)^2}$$

As in the previous model, the correcting factor due to crossing air/water boundary $\delta b = 0.96$ and the correcting factor for the decrease in absorption caused by a bubble of radius r is $\delta a = 13.2 \exp(-2.58 - 0.029r)$

Since $r=0.5$, $\delta a = 1.01$

Hence, the ratio of the detected intensity to the emitted intensity for bubbles 1 mm in diameter is

$$I_d/I_e = \delta r \times \delta b \times \delta a$$

$$= \frac{0.56}{(0.5625 + l)^2} (0.96)(1.01) = \frac{0.54}{(0.5625 + l)^2}$$

The graph in figure 3a.11 shows the relative intensity I_d/I_e of bubbles of 1 mm diameter for various values of l .

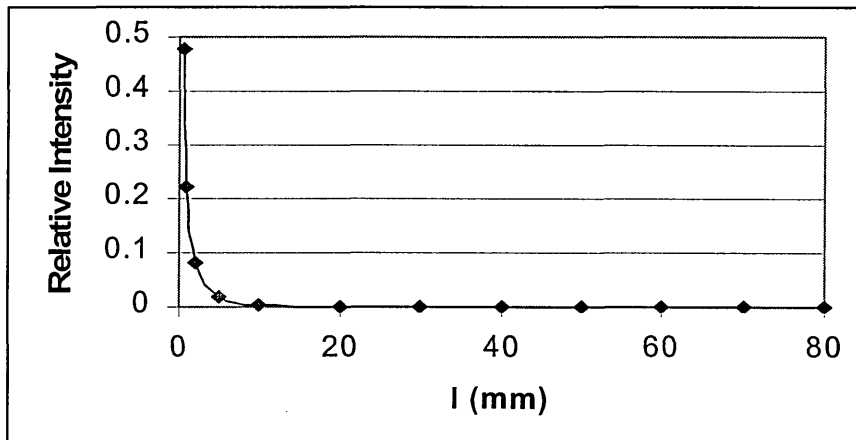


Figure 3a.11 Variation in relative intensity with bubble position for 1 mm bubble

Case (iii): Bubble amplitudes less than 1mm diameter and the light beam passes through the optical centre of the bubble

In the case of bubbles less than 1 mm in diameter, refer to figure 3a.12.

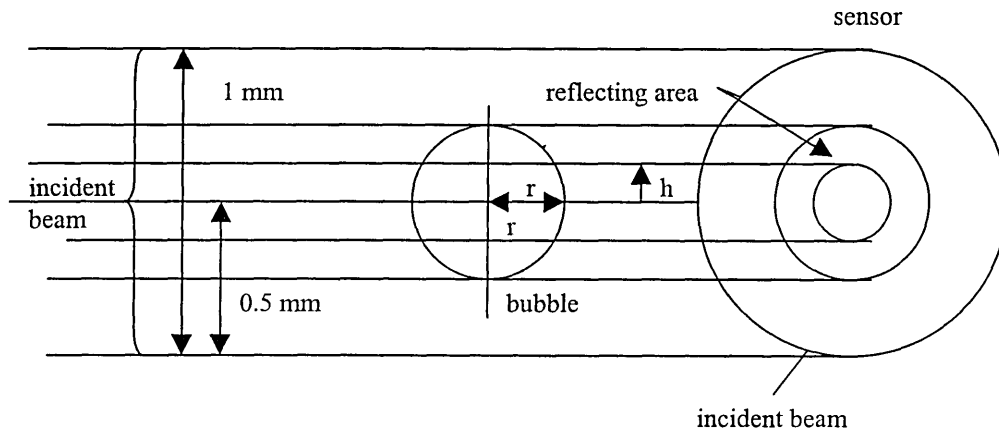


Figure 3a.12 Diagram of axial bubble of diameter less than 1mm with image of bubble projected onto sensor surface

The beam (1mm diameter) is wider than the bubble (diameter < 1mm) so part of the beam is not intercepted by the bubble. Hence some of the light passes the bubble without any interaction. The unmodified beam area is $\pi(0.5^2-r^2)$. The intensity of this part of the beam is altered only by absorption.

With no bubble present, the correction factor for the change in absorption of the radiation from the source is one. But, because of the reduced area caused by the bubble,

$$\delta a' = 1 - \frac{\pi(0.5^2-r^2)}{\pi \cdot 0.5^2} = 4 \cdot (0.5^2-r^2)$$

The light striking the periphery of the bubble is reflected. The area of the reflected beam is $\pi[r^2-(0.75r)^2]$. The light passing through the centre of the bubble is diverged.

From figure 3a.13,

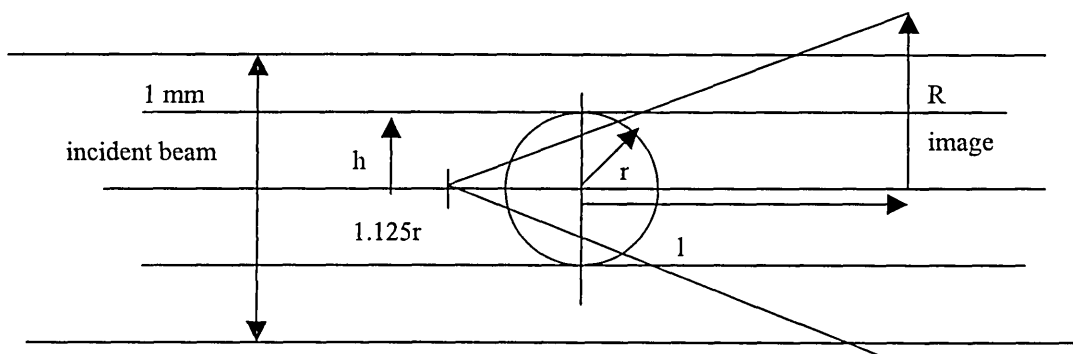


Figure 3a.13 Beam spread by small bubble

Using similar triangles,

$$\frac{R}{h} = \frac{l + 1.125r}{1.125r}$$

$$R = (l + 1.125r)0.75r / 1.125r = 0.67(l + 1.125r)$$

For the light passing through the bubble, the fractional loss of intensity due to refraction is

$$\delta r = \frac{\pi h^2}{\pi R^2} = \frac{\pi(0.75r)^2}{\pi[(l + 1.125r) / 0.67]^2} = \frac{1.25r^2}{(l + 1.125r)^2}$$

As in the previous model, the correcting factor due to crossing air/water boundary $\delta b = 0.96$ and the correcting factor for the decrease in absorption caused by a bubble of radius r is $\delta a = 13.2 \exp(-2.58 - 0.029r)$

Hence, the ratio of the detected intensity to the emitted case for bubbles less than 1 mm in diameter consists of two parts, one due to the part of the beam that misses the bubble and the second due to the effects of the bubble.

$$I_d/I_e = \delta r \times \delta b \times \delta a + \delta a \quad (3.d)$$

$$= \frac{1.25r^2}{(l + 1.125r)^2} (0.96)13.2 \exp(-2.58 - 0.029r) + 4(0.5^2 - r^2)$$

The graph in figure 3a.14 shows the relative detected intensity I_d/I_e of bubbles of various radii for $l = 50\text{mm}$,

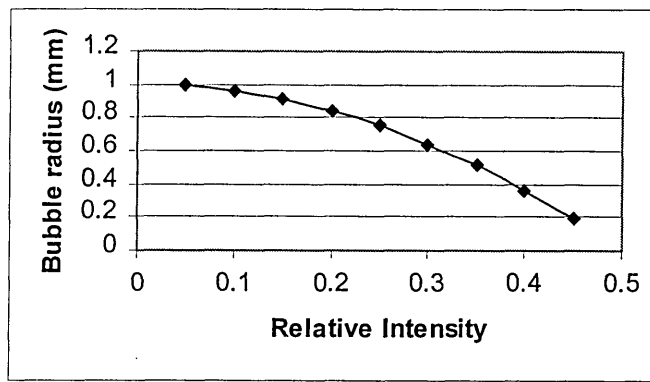


Figure 3a.14 Effect on relative intensity for bubbles less than 1 mm diameter.

Case (iv): Bubble of various amplitudes and the light beam off the principal axis

For off axis beams the model is shown in figure 3a.15. When the collimated incident beam is displaced parallel to principal axis, the two rays defining the boundary of the beam still appear to come from the equivalent principal focus of the bubble.

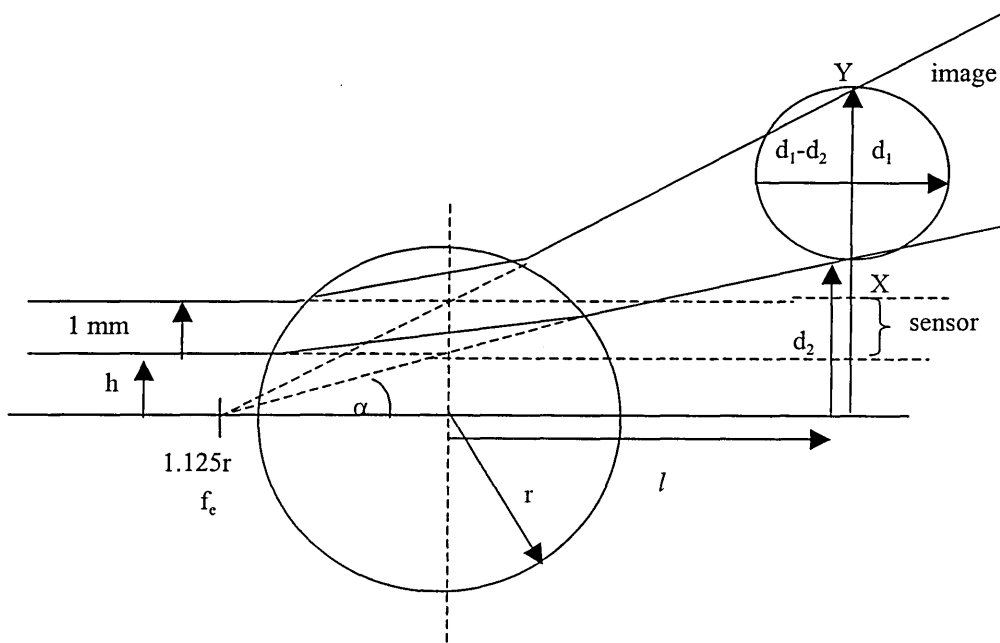


Figure 3a.15 Off axis bubble

This model will prevent any light arriving at the bubble, because all sensors have an aperture which will only accept approximately 2.9° off axis light.

$$\sin \alpha = h/r$$

and if α exceeds 2.9°, no sensor will accept the light beam (equation (3.b.1)).

3.2.2 Moving bubble

This section briefly discusses what happens at the sensor as the bubble crosses the light beam. Two cases are outlined :-

1. Bubbles less than 1mm diameter.

As described earlier small bubbles never totally prevent light energy arriving at the sensor. As the bubble crosses the light beam, the light level is reduced, reaches a minimum (equation 3.d) and then increases again.

2. Bubbles greater than 1mm diameter.

For convenience it is assumed that the optical centre of the bubble will pass through the centre of the incident beam. As the bubble rises into the beam, the top of the bubble will totally reflect the light incident on it reducing transmission to zero. As this part of the beam clears the reflecting area, the light intensity will grow until the centre of the bubble passes through the beam. The process will then reverse (figure 3a.16).

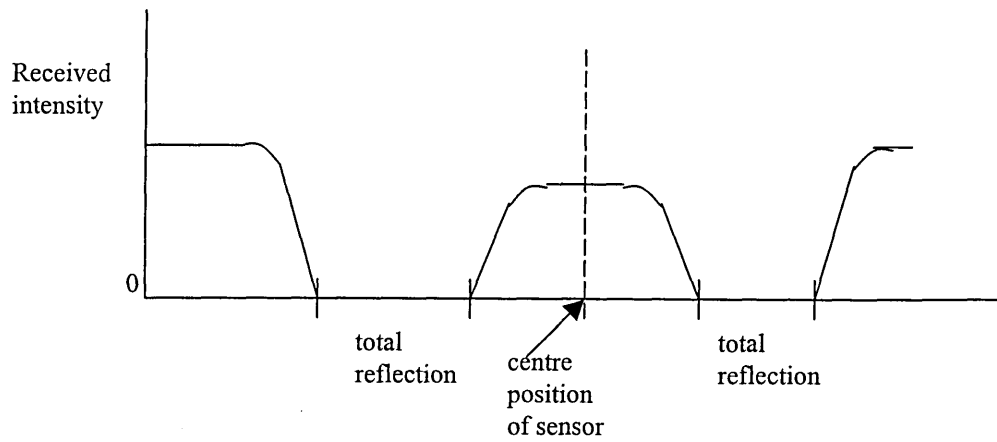


Figure 3a.16 Typical signal arriving at sensor due to moving bubble

The maximum value of the received intensity depends on the bubble diameter. For large bubbles the intensity may exceed eighty percent of the intensity when water alone is present and is shown in figure 3a.9.

3.3 Projection geometry

Different arrangements of the fibre sensors are considered for different types of projections. These consist of :-

- (a) two orthogonal projections consisting of several parallel views (figure 3.1).
- (b) two rectilinear projections consisting of several parallel views inclined at 45° to a horizontal axis (figure 3.2).
- (c) a combination of one orthogonal and two rectilinear projections (figure 3.3).
- (d) a combination of two orthogonal and two rectilinear projections (figure 3.4).
- (e) three fan-beam projections (figure 3.5).
- (f) four fan-beam projections (figure 3.6).

In figures 3.1 to 3.6, s_i stands for sensor i and p_k stands for projection k . For example; s_{21} , p_3 corresponds to sensor 21 which is located in the third projection.

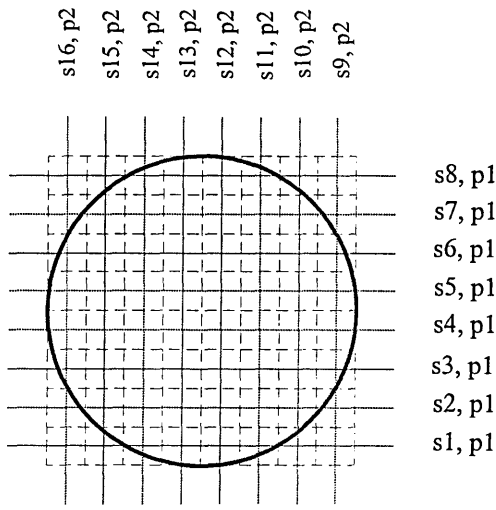


Figure 3.1 Two orthogonal projections

s8, p1
s7, p1
s6, p1
s5, p1
s4, p1
s3, p1
s2, p1
s1, p1

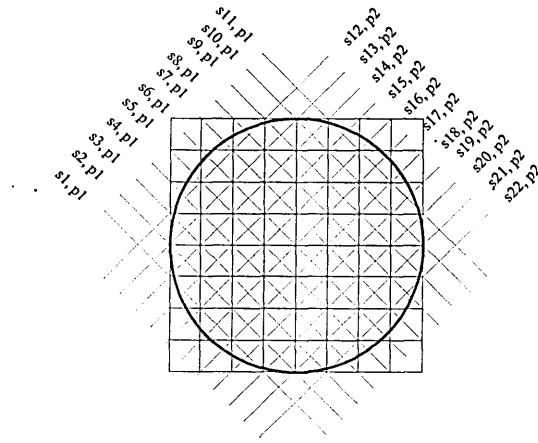


Figure 3.2 Two rectilinear projections

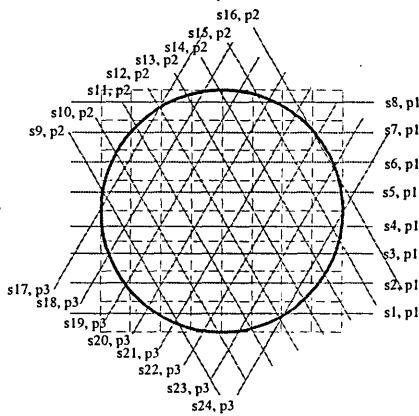


Figure 3.3 Combination of one orthogonal and two rectilinear projections

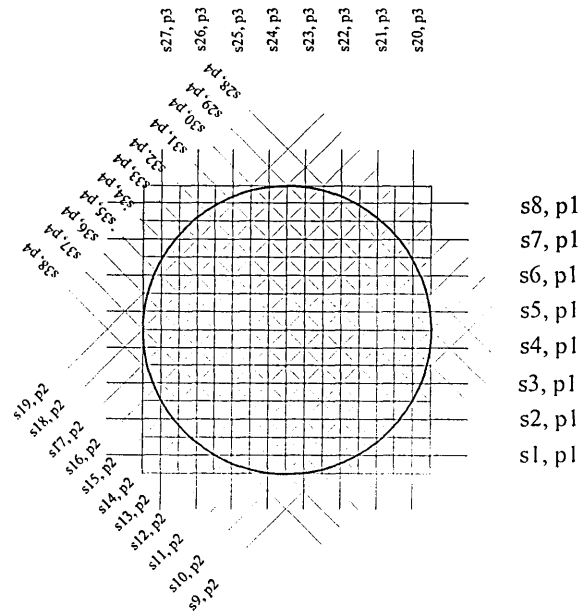


Figure 3.4 Combination of two orthogonal and two rectilinear projections

s8, p1
s7, p1
s6, p1
s5, p1
s4, p1
s3, p1
s2, p1
s1, p1

For the two orthogonal projections, each projection provides eight light beams (views) which are parallel and equally spaced to each other. The light emitters and detectors are arranged in a one-to-one basis i.e. each emitter has a corresponding detector. Similarly in the rectilinear projections, the emitters and detectors are also positioned on a one-to-one basis. In the case of the two rectilinear projections, the projections are inclined at

45° to the horizontal whereas in the case of the combination of one orthogonal and two rectilinear projections several parallel views are inclined at 120° to one another.

In cases (e) and (f) above, a series of angular projections of the light source and detectors are used to interrogate the measurement section; these are termed fan beam projections. In the case of three fan-beam projections, three light sources are used. Each light source will supply twelve light beams which are spaced at 10° intervals. This results in the cross-section of the pipe being interrogated by a total of thirty six light beams as shown in figure 3.5.

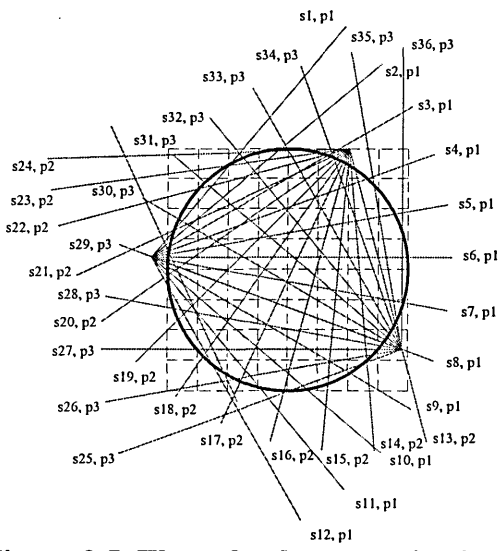


Figure 3.5 Three fan-beam projections

In the case of four fan-beam projections, four light sources are utilised and the light sources are placed 90° apart as shown in figure 3.6 resulting in a total of forty eighth light beams.

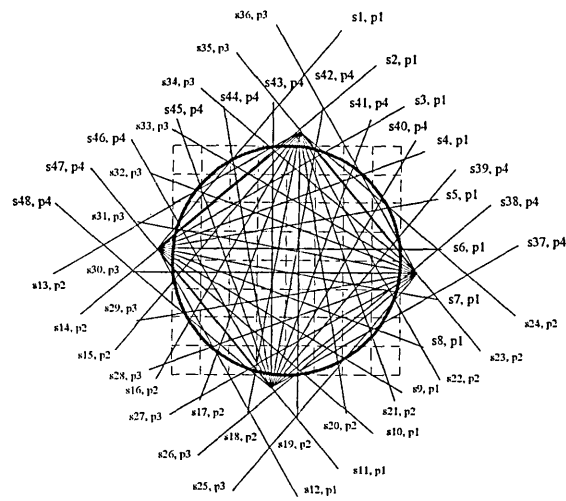


Figure 3.6 Four fan-beam projections

All the projection geometries are investigated for both the path length and the optical attenuation models.

3.4 Optical path length model

This model is based on the length of the optical sensing beam within the conveyor, the greater the active length (section 3.1), the greater the probability of an effectively opaque small bubble intercepting the beam [Abdul Rahim, 1996]. Empirically, it has been shown that the relationship between particle/bubble concentration and sensor voltage is linear for low conveyed material flow rates [Abdul Rahim, 1996]. The voltage of each individual path length sensor increases with increased bubble flow rate or in other words the more bubbles that intersect a light beam the greater the output voltage [Abdul Rahim et al, 1995]. It is assumed that the relationship between the number of small bubbles passing through a beam and the corresponding sensor output voltage is linear; tests by Abdul Rahim [Abdul Rahim, 1996] support this assumption. The output voltage from the sensors in this thesis are conditioned to be proportional to the rate at which the beam is intercepted by small bubbles (section 4.3.2). For a given uniform flow rate the output voltage from each sensor will be directly proportional to its optical

path length. A cross section of the pipe is considered and a rectangular array consisting of 8×8 equal size pixels projected onto it. Some pixels lie outside the pipe, some are intersected by it, but the majority are located within the pipe cross section (figure 3.7).

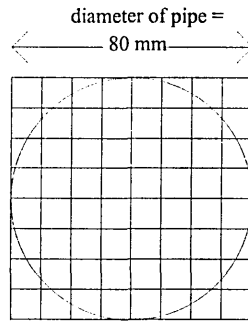


Figure 3.7 A cross-section of the pipe fitted into a rectangular array of 8×8 pixels

3.4.1 Forward problem for the optical path length model

The forward problem provides the theoretical output of each sensor under no-flow and flow conditions, when the sensing area is considered to be two dimensional. Solution of the forward problem generates a series of sensitivity matrices. Each matrix is associated with a specific sensor and relates to the sensor output under flow conditions.

To simplify the model, it is assumed that light beams travel in straight lines. It is assumed that for each light beam, the distance between emitter and detector is 100 mm and the beam width is 1 mm (i.e. the model neglects beam spread). It is also assumed that the beam in each pixel has a rectangular shape which simplifies the calculation of the area of the light beam in each pixel. Each pixel is designated as P_{ij} , where i is the row number and j is the column number. The dimension of each pixel is 10mm x 10mm.

The area of each pixel enclosed by the circle is calculated. Then the area occupied by a specific light beam in each pixel is determined. Pixels outside the circle (representing

the flow pipe) and pixels through which the specified light beam does not pass are assumed to contain air. Based on this *a priori* knowledge all such pixels will be assigned zero sensitivity values [Abdul Rahim, 1996]. The sensitivity matrix for each light beam (or for each sensor) is formed by calculating the ratio of the area of the light beam in each pixel to the area of the corresponding pixel. Each pixel is evaluated separately and the contribution from each pixel forms the sensitivity map [Abdul Rahim, 1996]. Each sensor is considered separately. As an example, for the two orthogonal projections system, the sensitivity matrix, s_7 , for sensor 7 (figure 3.5) is

$$s_7 = \begin{bmatrix} 0 & 0 & 0 & 0 & 0 & 0 & 0 & 0 \\ 2.5/18 & 10/91.45 & 10/100 & 10/100 & 10/100 & 10/100 & 10/91.45 & 2.5/18 \\ 0 & 0 & 0 & 0 & 0 & 0 & 0 & 0 \\ 0 & 0 & 0 & 0 & 0 & 0 & 0 & 0 \\ 0 & 0 & 0 & 0 & 0 & 0 & 0 & 0 \\ 0 & 0 & 0 & 0 & 0 & 0 & 0 & 0 \\ 0 & 0 & 0 & 0 & 0 & 0 & 0 & 0 \\ 0 & 0 & 0 & 0 & 0 & 0 & 0 & 0 \end{bmatrix}$$

Matrix 3.1

3.4.2 Inverse Problem for the optical path length model

The inverse problem estimates the distribution of material within the pipe which provides the measured sensor outputs. Due to the limited number of views (i.e. 36 for the three projection system) and the larger number of pixels inside the pipe (i.e. 60), an analytic solution is not possible, so a layergram (LYG) back-projection (LYGBP) is used to solve the inverse problem (section 3.6).

3.5 The optical attenuation model

The optical attenuation model assumes both conveyed and conveying mediums are transparent, but possess different optical attenuation coefficients.

3.5.1 Forward problem for the optical attenuation model

As in the optical path length model (section 3.3.1), the forward problem for the optical attenuation model is that of mapping a set of theoretical ‘parameters’ into a set of experimentally measured ‘results’. Solution of the forward problem generates a series of sensitivity matrices. Each matrix is associated with a specific sensor and relates to the sensor output under flow conditions. The same assumptions are made as in the case of the optical path length model in that it is assumed that light beams travel in straight lines. It is assumed that for each light beam, the distance between emitter and detector is 100 mm and the beam width is 1 mm (i.e. the model neglects beam spread).

In the optical attenuation model the output value of the sensor is a function of the medium which the light traverses en route from the emitter. This model neglects light scattering and beam divergence. It is based on absorption of the beam by the medium within the pipe as defined by equation (3.1) (Lambert-Beer’s law) [Ramli, 1998]

$$V_m = V_{in} \exp[-\alpha_w l_w - \alpha_a l_a]$$

but $l_a = 2r + 20$ (mm) and $l_w = 80 - 2r$ (mm). Note that the pipe diameter is 80 mm, the aperture stop has a length of 20 mm and $r =$ radius of bubble.

Hence,

$$V_m = V_{in} \exp[-0.0287(80-2r) + 0.0142(2r + 20)] \quad (3.1)$$

where:

V_m = voltage of the receiving sensor (V)

V_{in} = voltage of the receiver when there is no beam attenuation (empty pipe) (V)

α_a = absorption coefficient of air (mm^{-1})

α_w = absorption coefficient of water (mm^{-1})

l_a = path length of air (mm)

l_w = path length of water (mm)

Assuming the attenuation coefficient of air, $\alpha_a = 0.0142 \text{ mm}^{-1}$ [Daniels, 1996] and the attenuation coefficient of water, $\alpha_w = 0.0287 \text{ mm}^{-1}$ [Daniels, 1996], the path length traversed by the light in air and water, $l_a + l_w = 100 \text{ mm}$, and when there are no bubbles in the water, $r = 0 \text{ mm}$, the voltage of the sensor when no bubble flows through the pipe is,

$$V_m = V_{in} \exp -(0.0287 \times 80 + 0.0142 \times 20) = 0.0758 V_{in} \quad (3.2)$$

Now consider one pixel to contain a bubble with an attenuation coefficient of 0.0142 mm^{-1} . The output voltage for each sensor is calculated. This process is repeated until all pixels within the pipe have been considered. As an example, consider the two orthogonal projections (figure 3.1) case. For sensor 7 the calculation is as follows :-

Light going to sensor 7 passes through pixels $P_{21}, P_{22}, P_{23}, P_{24}, P_{25}, P_{26}, P_{27}$ and P_{28} .

Pixel P_{21} is assumed to contain bubbles with $\alpha_o = 0.0142 \text{ mm}^{-1}$ whereas all other pixels contain water ($\alpha_w = 0.0287 \text{ mm}^{-1}$). Hence for pixel P_{21} , the path length of the light in the bubbles is 2.5 mm and the resulting voltage is

$$V_m = V_{in} \exp -[0.0287(80 - 2.5) + 0.0142 (20 + 2.5)] = 0.0786 V_{in} \quad (3.3)$$

Now pixel P_{21} is filled with water and pixel P_{22} with bubbles. Hence for pixel P_{22} , the path length of the light in the bubbles is 10 mm and the resulting voltage is

$$V_m = V_{in} \exp [0.0287(80 - 10) + 0.0142 (20 + 10)] = 0.0876 V_{in} \quad (3.4)$$

This process is repeated for the remaining pixels in the path to sensor 7 as shown in the following calculations.

For pixels $P_{23}, P_{24}, P_{25}, P_{26}$ and P_{27} the path length of the light in the bubbles is 10 mm in each pixel and the resulting voltage is

$$V_m = V_{in} \exp[0.0287(80 - 10) + 0.0142(20 + 10)] = 0.0876 V_{in} \quad (3.5)$$

For pixel P_{28} , the path length of the light in the bubbles is 10 mm and the resulting voltage is

$$V_m = V_{in} \exp[-0.0287(80 - 2.5) + 0.0142(20 + 2.5)] = 0.0786 V_{in} \quad (3.6)$$

The other pixels, which the light to sensor 7 does not traverse, are neglected at this time.

The voltages calculated for sensor 7 are normalised by dividing each calculated value by the sensor output with no bubble present e.g.

$0.0758V_{in}$ is the unattenuated voltage with no bubble present. $0.0786V_{in}$ is the calculated voltage for pixel P_{21} filled with gas. The sensitivity term for P_{21} i.e. $S_{21} = 0.0786V_{in} / 0.0758V_{in}$. Similarly for pixel P_{22} , the calculated voltage is $0.0876V_{in}$ and the corresponding sensitivity term, S_{22} , is $S_{22} = 0.0876V_{in} / 0.0758V_{in}$.

This means for each pixel in the sensitivity matrix, the value in each pixel is the ratio of the attenuated voltage due to a bubble in that pixel to the sensor voltage when no bubble flows in the pipe. The resulting sensitivity matrix, s_7 , for sensor 7 in the two orthogonal projections system is,

$$s_7 = \begin{bmatrix} 0 & 0 & 0 & 0 & 0 & 0 & 0 & 0 \\ \frac{0.0786}{0.0758} & \frac{0.0876}{0.0758} & \frac{0.0876}{0.0758} & \frac{0.0876}{0.0758} & \frac{0.0876}{0.0758} & \frac{0.0876}{0.0758} & \frac{0.0876}{0.0758} & \frac{0.0786}{0.0758} \\ 0 & 0 & 0 & 0 & 0 & 0 & 0 & 0 \\ 0 & 0 & 0 & 0 & 0 & 0 & 0 & 0 \\ 0 & 0 & 0 & 0 & 0 & 0 & 0 & 0 \\ 0 & 0 & 0 & 0 & 0 & 0 & 0 & 0 \\ 0 & 0 & 0 & 0 & 0 & 0 & 0 & 0 \\ 0 & 0 & 0 & 0 & 0 & 0 & 0 & 0 \end{bmatrix}$$

which is independent of V_{in} .

The output voltage for each sensor is calculated for each pixel in turn. This process is repeated until all pixels within the pipe have been considered. This process is also

repeated for all the sensors resulting in $n \times 8 \times 8$ matrices, where n is the number of views (sensors).

3.5.2 Inverse problem for the optical attenuation model

The solution to the inverse problem involves the process of combining the computed sensitivity maps with the measured data (sensors' readings) to obtain an image of the material concentration distribution within the conveyor. The layergram back-projection calculations for the optical attenuation model are similar to those for the path length model (section 3.3.2).

3.6 Models of flowing objects

In order to investigate the effectiveness of the reconstruction algorithms, four flow models are considered :-

- (a) A single pixel within the pipe is assumed to be affected by the flowing medium.
- (b) Two pixels within the pipe are assumed to be affected by the flowing medium. This model can be used to test aliasing effect.
- (c) Half flow where all the pixels on one side of the pipe diameter are assumed to be equally affected by the flowing medium where as the remaining pixels are unaffected.
- (d) Full flow where all the pixels within the pipe are equally affected.

3.6.1 Single pixel flow model

In this model, only a single pixel contains an object. The pixel chosen for this model is P_{33} as shown in figure 3.8.

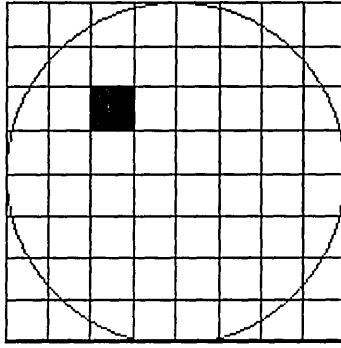


Figure 3.8

3.6.1.1 Path length model

The sensor readings for various projections for the path length model in the case of the single pixel model are tabulated in table 3.1. The sensor voltage is calculated from the following expression,

$$V_r = \frac{l_p}{l_t} \times V_s \quad (3.8)$$

where

l_p = length of light beam in the pixel occupied by the bubble

l_t = total beam length (i.e. 100 mm)

V_r = sensor voltage

V_s = supply voltage = 5V.

Sensor Number	Estimated sensor's reading (V)					
	2 Orthogonal	2 Rectilinear	1 Orthogonal/ 2 Rectilinear	2 Orthogonal /2 Rectilinear	3 fan-beam	4 fan-beam
s1	0	0	0	0	0	0
s2	0	0	0	0	0	0
s3	0	0	0	0	0.15	0.15
s4	0	0	0	0	0.475	0.475
s5	0	0	0	0	0.025	0.025
s6	0	0.7	0.5	0.5	0	0
s7	0	0	0	0	0	0
s8	0	0	0	0	0	0
s9	0	0	0	0	0	0
s10	0	0	0	0	0	0
s11	0.5	0	0.15	0	0	0
s12	0	0	0.25	0	0	0
s13	0	0	0	0	0	0
s14	0.5	0.7	0	0	0	0
s15	0	0	0	0	0	0.3
s16	0	0	0	0	0	0.55
s17	-	0	0	0.5	0	0
s18	-	0	0.25	0	0	0
s19	-	0	0.15	0	0.5	0
s20	-	0	0	0	0	0
s21	-	0	0	0	0	0
s22	-	0	0	0	0	0
s23	-	-	0	0	0	0
s24	-	-	0	0	0	0
s25	-	-	-	0.5	0	0
s26	-	-	-	0	0	0
s27	-	-	-	0	0	0
s28	-	-	-	0	0.625	0
s29	-	-	-	0	0	0.525
s30	-	-	-	0	0	0
s31	-	-	-	0	0	0
s32	-	-	-	0	0	0
s33	-	-	-	0.5	0	0
s34	-	-	-	0	0	0
s35	-	-	-	0	0	0
s36	-	-	-	0.7	0	0
s37	-	-	-	0	-	0
s38	-	-	-	0	-	0
s39	-	-	-	-	-	0
s40	-	-	-	-	-	0
s41	-	-	-	-	-	0.5
s42	-	-	-	-	-	0
s43	-	-	-	-	-	0
s44	-	-	-	-	-	0
s45	-	-	-	-	-	0
s46	-	-	-	-	-	0
s47	-	-	-	-	-	0
s48	-	-	-	-	-	0

Table 3.1 Estimated sensor readings for single pixel flow model based on the path length model

3.6.1.2 Optical attenuation model

The sensor readings for various projections for the optical attenuation model in the case of the single pixel model are tabulated in table 3.2. The sensor voltage is calculated from equation (3.1):

$$V_m = V_{in} \exp[-100\alpha_w + 1_a(\alpha_w - \alpha_a)] \quad (3.1)$$

in which

the attenuation coefficient of air, $\alpha_a = 0.0142 \text{ mm}^{-1}$, and

the attenuation coefficient of water, $\alpha_w = 0.0287 \text{ mm}^{-1}$.

V_{in} is assumed to be 5 V.

Sensor Number	Estimated sensor's reading (V)					
	2 Ortho-gonal	2 Recti-linear	1 Orthogonal/2 Rectilinear	2 Orthogonal/2 Rectilinear	3 fan-beam	4 fan-beam
s1	0.2835	0.2835	0.2835	0.2835	0.2835	0.2835
s2	0.2835	0.2835	0.2835	0.2835	0.2835	0.2835
s3	0.2835	0.2835	0.2835	0.2835	0.2961	0.2961
s4	0.2835	0.2835	0.2835	0.2835	0.3254	0.3254
s5	0.2835	0.2835	0.2835	0.2835	0.2856	0.2856
s6	0.3277	0.3473	0.3277	0.3277	0.2835	0.2835
s7	0.2835	0.2835	0.2835	0.2835	0.2835	0.2835
s8	0.2835	0.2835	0.2835	0.2835	0.2835	0.2835
s9	0.2835	0.2835	0.2835	0.2835	0.2835	0.2835
s10	0.2835	0.2835	0.307	0.2835	0.2835	0.2835
s11	0.3277	0.2835	0.294	0.2835	0.2835	0.2835
s12	0.2835	0.2835	0.2835	0.2835	0.2835	0.2835
s13	0.2835	0.2835	0.2835	0.2835	0.2835	0.2835
s14	0.2835	0.3473	0.2835	0.2835	0.2835	0.2835
s15	0.2835	0.2835	0.2835	0.2835	0.2835	0.3093
s16	0.2835	0.2835	0.2835	0.2835	0.2835	0.3325
s17	-	0.2835	0.2835	0.2835	0.2835	0.2835
s18	-	0.2835	0.2835	0.2835	0.2835	0.2835
s19	-	0.2835	0.2835	0.2835	0.3277	0.2835
s20	-	0.2835	0.3349	0.2835	0.2835	0.2835
s21	-	0.2835	0.2835	0.2835	0.2835	0.2835
s22	-	0.2835	0.2835	0.3473	0.2835	0.2835
s23	-	-	0.2835	0.2835	0.2835	0.2835
s24	-	-	0.2835	0.2835	0.2835	0.2835
s25	-	-	-	0.2835	0.2835	0.2835
s26	-	-	-	0.2835	0.2835	0.2835
s27	-	-	-	0.2835	0.2835	0.2835
s28	-	-	-	0.2835	0.3398	0.2835
s29	-	-	-	0.2835	0.2835	0.3301
s30	-	-	-	0.3473	0.2835	0.2835
s31	-	-	-	0.2835	0.2835	0.2835
s32	-	-	-	0.2835	0.2835	0.2835
s33	-	-	-	0.2835	0.2835	0.2835
s34	-	-	-	0.2835	0.2835	0.2835
s35	-	-	-	0.2835	0.2835	0.2835
s36	-	-	-	0.2835	0.2835	0.2835
s37	-	-	-	0.2835	-	0.2835
s38	-	-	-	0.2835	-	0.2835
s39	-	-	-	-	-	0.2835
s40	-	-	-	-	-	0.2835
s41	-	-	-	-	-	0.3048
s42	-	-	-	-	-	0.2835
s43	-	-	-	-	-	0.2835
s44	-	-	-	-	-	0.2835
s45	-	-	-	-	-	0.2835
s46	-	-	-	-	-	0.2835
s47	-	-	-	-	-	0.2835
s48	-	-	-	-	-	0.2835

Table 3.2 Estimated sensor readings for single pixel flow model based on the optical attenuation model

3.6.2 Two pixels flow model

In this model, two pixels contain objects. The pixels chosen for this model are P_{33} and P_{66} as shown in figure 3.9.

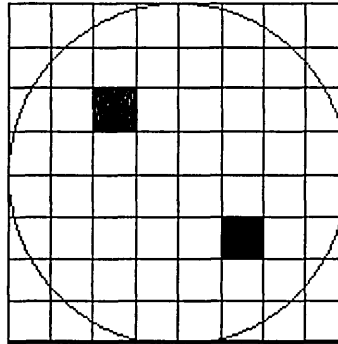


Figure 3.9

3.6.2.1 Path length model

The sensor readings based on equation (3.8) for various projections for the path length model in the case of the two pixels flow model are tabulated in table 3.3.

Sensor Number	Estimated sensor's reading (V)					
	2 Ortho-gonal	2 Recti-linear	1 Orthogonal/ 2 Rectilinear	2 Orthogonal /2 Rectilinear	3 fan-beam	4 fan-beam
s1	0	0	0	0	0	0
s2	0	0	0	0	0	0
s3	0.5	0	0.5	0.5	0.15	0.15
s4	0	0	0	0	0.48	0.48
s5	0	0	0	0	0.03	0.03
s6	0.5	1.4	0.5	0.5	0	0
s7	0	0	0	0	0	0
s8	0	0	0	0	0	0
s9	0	0	0	0	0	0
s10	0	0	0	0	0	0
s11	0.5	0	0.15	0.7	0	0
s12	0	0	0.3	0	0	0
s13	0	0	0.4	0	0	0
s14	0.5	0.7	0	0	0	0
s15	0	0	0	0	0	0.3
s16	0	0	0	0	0	0.55
s17	-	0	0	0.7	0	0
s18	-	0	0.25	0	0	0
s19	-	0	0.15	0	0.5	0
s20	-	0.7	0	0	0	0
s21	-	0	0	0	0	0
s22	-	0	0.15	0.5	0	0
s23	-	-	0.25	0	0	0
s24	-	-	0	0	0	0
s25	-	-	-	0.5	0	0
s26	-	-	-	0	0	0
s27	-	-	-	0	0	0
s28	-	-	-	0	0.63	0
s29	-	-	-	0	0	0.53
s30	-	-	-	0	0	0
s31	-	-	-	0	0	0
s32	-	-	-	0	0	0
s33	-	-	-	1.4	0	0
s34	-	-	-	0	0	0
s35	-	-	-	0	0	0
s36	-	-	-	0	0	0
s37	-	-	-	0	-	0
s38	-	-	-	0	-	0
s39	-	-	-	-	-	0
s40	-	-	-	-	-	0
s41	-	-	-	-	-	0.5
s42	-	-	-	-	-	0
s43	-	-	-	-	-	0
s44	-	-	-	-	-	0
s45	-	-	-	-	-	0
s46	-	-	-	-	-	0
s47	-	-	-	-	-	0
s48	-	-	-	-	-	0

Table 3.3 Estimated sensor readings for two pixels flow model based on path length model

3.6.2.2 Optical attenuation model

The sensor readings based on equation (3.1) for various projections for the optical attenuation model in the case of the two pixels flow model are tabulated in table 3.4.

Sensor Number	Estimated sensor's reading (V)					
	2 Ortho-gonal	2 Recti-linear	1 Orthogonal/ 2 Rectilinear	2 Orthogonal /2 Rectilinear	3 fan-beam	4 fan-beam
s1	0.2835	0.2835	0.2835	0.2835	0.2835	0.2835
s2	0.2835	0.2835	0.2835	0.2835	0.2835	0.2835
s3	0.3277	0.2835	0.3277	0.3277	0.2961	0.2961
s4	0.2835	0.2835	0.2835	0.2835	0.3254	0.3254
s5	0.2835	0.2835	0.2835	0.2835	0.2856	0.2856
s6	0.3277	0.4255	0.3277	0.3277	0.2835	0.2835
s7	0.2835	0.2835	0.2835	0.2835	0.2835	0.2835
s8	0.2835	0.2835	0.2835	0.2835	0.3301	0.3301
s9	0.2835	0.2835	0.2835	0.2835	0.2835	0.2835
s10	0.2835	0.2835	0.307	0.2835	0.2835	0.2835
s11	0.3277	0.2835	0.294	0.3277	0.2835	0.2835
s12	0.2835	0.2835	0.2835	0.2835	0.2835	0.2835
s13	0.2835	0.2835	0.2835	0.2835	0.2835	0.2835
s14	0.3277	0.3473	0.2961	0.3277	0.2835	0.2835
s15	0.2835	0.2835	0.307	0.2835	0.2835	0.3093
s16	0.2835	0.2835	0.2835	0.2835	0.2835	0.3325
s17	-	0.2835	0.2835	0.2835	0.3254	0.2835
s18	-	0.2835	0.2835	0.2835	0.3349	0.2835
s19	-	0.2835	0.2835	0.2835	0.3398	0.2835
s20	-	0.3473	0.2835	0.2835	0.2835	0.3277
s21	-	0.2835	0.3349	0.2835	0.2835	0.2835
s22	-	0.2835	0.2835	0.4255	0.2835	0.2835
s23	-	-	0.2835	0.2835	0.2835	0.2835
s24	-	-	0.2835	0.2835	0.2835	0.2835
s25	-	-	-	0.2835	0.2835	0.2835
s26	-	-	-	0.2835	0.2835	0.2835
s27	-	-	-	0.2835	0.2835	0.2835
s28	-	-	-	0.2835	0.3398	0.2835
s29	-	-	-	0.2835	0.2835	0.3301
s30	-	-	-	0.3473	0.2835	0.2835
s31	-	-	-	0.2835	0.2835	0.2835
s32	-	-	-	0.2835	0.2835	0.2835
s33	-	-	-	0.2835	0.3277	0.3301
s34	-	-	-	0.2835	0.2835	0.294
s35	-	-	-	0.2835	0.2835	0.2835
s36	-	-	-	0.3473	0.2835	0.2835
s37	-	-	-	0.2835	-	0.2835
s38	-	-	-	0.2835	-	0.2835
s39	-	-	-	-	-	0.2835
s40	-	-	-	-	-	0.2835
s41	-	-	-	-	-	0.3277
s42	-	-	-	-	-	0.2835
s43	-	-	-	-	-	0.2835
s44	-	-	-	-	-	0.2835
s45	-	-	-	-	-	0.3349
s46	-	-	-	-	-	0.3026
s47	-	-	-	-	-	0.2835

Table 3.4 Estimated sensor readings for two pixels flow model based on optical attenuation model

3.6.3 Half flow model

In this model, the left-hand side of the pipe is filled with particles as shown in figure 3.10.

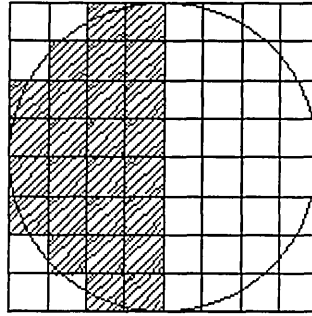


Figure 3.10

3.5.3.1 Path length model

The sensor readings based on equation (3.8) for various projections for the path length model in the case of the half flow model are tabulated in table 3.5.

Sensor Number	Estimated sensor's reading (V)					
	2 Ortho-gonal	2 Recti-linear	1 Orthogonal/ 2 Rectilinear	2 Orthogonal/ /2 Rectilinear	3 fan-beam	4 fan-beam
s1	0.95	1.85	1.3	0.95	1.425	1.425
s2	1.55	2.8	1.75	1.55	2.400	2.400
s3	1.75	2.725	1.85	1.75	2.2750	2.2750
s4	1.9875	2.55	1.95	1.9875	2.125	2.125
s5	1.9875	2.3	1.95	1.9875	2.0250	2.0250
s6	1.75	1.975	1.85	1.75	2.000	2.000
s7	1.55	1.6	1.75	1.55	2.050	2.050
s8	0.95	1.15	1.3	0.95	2.1250	2.1250
s9	1.9	0.625	2.55	0	2.3250	2.3250
s10	3.1	0	3.4	0	2.6000	2.6000
s11	3.5	0	2.85	0.65	2.3000	2.3000
s12	3.975	1.85	2.05	1.2	1.6000	1.6
s13	0	2.8	1.15	1.6	0	1.5
s14	0	2.725	0.1	2	0.8250	2.5
s15	0	2.55	0	2.1	1.4750	3.075
s16	0	2.3	0	2.6	1.9000	3.475
s17	-	1.975	1.75	2.75	2.1250	3.475
s18	-	1.6	3.15	2.9	2.1250	2.8
s19	-	1.15	3.15	2	1.8250	0
s20	-	0.625	2.4	0	1.2000	0
s21	-	0	1.55	0	0.0250	0
s22	-	0	0.55	0	0	0
s23	-	-	0	0	0	0
s24	-	-	0	4	0	0
s25	-	-	-	3.5	0.8750	0
s26	-	-	-	3.1	1.5750	0
s27	-	-	-	1.9	2.1000	0.425
s28	-	-	-	0	2.4500	1.2
s29	-	-	-	0	2.5500	1.7
s30	-	-	-	0.65	2.4250	1.95
s31	-	-	-	1.2	1.8500	1.975
s32	-	-	-	1.6	0.2500	1.8
s33	-	-	-	2	0	1.4
s34	-	-	-	2.1	0	0.725
s35	-	-	-	2.6	0	0
s36	-	-	-	2.75	0	0
s37	-	-	-	2.9	-	1.425
s38	-	-	-	2	-	2.325
s39	-	-	-	-	-	2.95
s40	-	-	-	-	-	3.425
s41	-	-	-	-	-	3.75
s42	-	-	-	-	-	3.95
s43	-	-	-	-	-	0.9
s44	-	-	-	-	-	0.3
s45	-	-	-	-	-	0.1
s46	-	-	-	-	-	0
s47	-	-	-	-	-	0
s48	-	-	-	-	-	0

Table 3.5 Estimated sensor readings for half flow model based on the path length model

3.6.3.2 Optical attenuation model

The sensor readings based on equation (3.1) for various projections for the optical attenuation model in the case of the half flow model are tabulated in table 3.6.

Sensor Number	Estimated sensor's reading (V)					
	2 Ortho-gonal	2 Recti-linear	1 Orthogonal/ 2 Rectilinear	2 Orthogonal /2 Rectilinear	3 fan-beam	4 fan-beam
s1	0.3734	0.4848	0.3734	0.3734	0.4286	0.4286
s2	0.4444	0.6385	0.4444	0.4444	0.5686	0.5686
s3	0.4848	0.6248	0.4848	0.4848	0.5484	0.5484
s4	0.5027	0.5939	0.5027	0.5027	0.5250	0.525
s5	0.5027	0.5524	0.5027	0.5027	0.51	0.51
s6	0.4848	0.5027	0.4848	0.4848	0.5063	0.5063
s7	0.4444	0.4509	0.4444	0.4444	0.5137	0.5137
s8	0.3734	0.3957	0.3734	0.3734	0.525	0.525
s9	0.4919	0.3398	0.499	0.4919	0.5564	0.5564
s10	0.6966	0.2835	0.7017	0.6966	0.6026	0.6026
s11	0.829	0.2835	0.7068	0.829	0.5524	0.5524
s12	0.8913	0.4848	0.5686	0.8913	0.4509	0.4509
s13	0.2835	0.6385	0.4444	0.2835	0.2835	0.438
s14	0.2835	0.6248	0.3301	0.2835	0.3601	0.5853
s15	0.2835	0.5939	0.2835	0.2835	0.4348	0.6916
s16	0.2835	0.5524	0.2835	0.2835	0.4919	0.7766
s17	-	0.5027	0.499	0.4848	0.525	0.7766
s18	-	0.4509	0.6966	0.6385	0.525	0.6385
s19	-	0.3957	0.829	0.6248	0.4813	0.2835
s20	-	0.3398	0.5686	0.5939	0.4015	0.2835
s21	-	0.2835	0.4444	0.5524	0.2856	0.2835
s22	-	0.2835	0.3301	0.5027	0.2835	0.2835
s23	-	-	0.2835	0.4509	0.2835	0.2835
s24	-	-	0.2835	0.3957	0.2835	0.2835
s25	-	-	-	0.3398	0.3654	0.2835
s26	-	-	-	0.2835	0.4476	0.2835
s27	-	-	-	0.2835	0.5212	0.3207
s28	-	-	-	0.4848	0.5769	0.4015
s29	-	-	-	0.6385	0.5939	0.4641
s30	-	-	-	0.6248	0.5727	0.499
s31	-	-	-	0.5939	0.4848	0.5027
s32	-	-	-	0.5524	0.3048	0.4778
s33	-	-	-	0.5027	0.2835	0.4255
s34	-	-	-	0.4509	0.2835	0.3498
s35	-	-	-	0.3957	0.2835	0.2835
s36	-	-	-	0.3398	0.2835	0.2835
s37	-	-	-	0.2835	-	0.4286
s38	-	-	-	0.2835	-	0.5564
s39	-	-	-	-	-	0.6669
s40	-	-	-	-	-	0.7654
s41	-	-	-	-	-	0.8411
s42	-	-	-	-	-	0.8913
s43	-	-	-	-	-	0.368
s44	-	-	-	-	-	0.3093
s45	-	-	-	-	-	0.2918
s46	-	-	-	-	-	0.2835

s47	-	-	-	-	-	0.2835
s48	-	-	-	-	-	0.2835

Table 3.6 Estimated sensor readings for half flow model based on the optical attenuation model

3.6.4 Full flow model

In this model, the whole pipe contains particles as shown in figure 3.11.

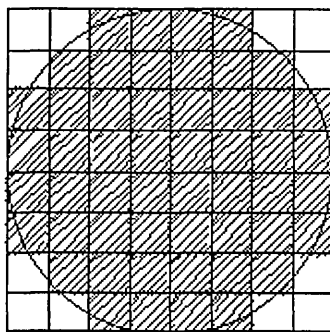


Figure 3.11

3.6.4.1 Path length model

The sensor readings based on equation (3.8) for various projections for the path length model in the case of the full flow model are tabulated in table 3.7.

Sensor Number	Estimated sensor's reading (V)					
	2 Ortho-gonal	2 Recti-linear	1 Orthogonal/ 2 Rectilinear	2 Orthogonal /2 Rectilinear	3 fan-beam	4 fan-beam
s1	1.9	1.85	2.6	1.9	1.425	1.425
s2	3.1	2.8	3.5	3.1	2.400	2.400
s3	3.5	3.35	3.7	3.5	3.025	3.025
s4	3.975	3.7	3.9	4	3.525	3.525
s5	3.975	3.9	3.9	4	3.725	3.725
s6	3.5	3.95	3.7	3.5	3.950	3.950
s7	3.1	3.9	3.5	3.1	3.625	3.625
s8	1.9	3.7	2.6	1.9	3.700	3.700
s9	1.9	3.35	2.55	1.95	3.450	3.450
s10	3.1	2.8	3.4	2.85	2.875	2.875
s11	3.5	1.85	3.85	3.4	2.300	2.300
s12	3.975	1.85	4	3.8	1.600	1.600
s13	3.975	2.8	3.85	3.95	1.075	1.5
s14	3.5	3.35	3.5	4	5.600	2.5
s15	3.1	3.7	2.85	3.95	2.950	3.1
s16	1.9	3.9	0.8	3.8	3.400	3.675
s17	-	3.95	1.75	3.4	3.750	3.925
s18	-	3.9	3.15	2.85	3.650	3.975
s19	-	3.7	3.7	1.95	4.0	3.95
s20	-	3.35	4	1.9	3.900	3.725
s21	-	2.8	3.95	3.1	3.375	3.45
s22	-	1.85	3.7	3.5	2.875	2.875
s23	-	-	3.1	4	2.150	1.75
s24	-	-	1.95	4	1.225	1.2
s25	-	-	-	3.5	1.400	1.525
s26	-	-	-	3.1	2.275	2.4
s27	-	-	-	1.9	2.950	3.075
s28	-	-	-	1.95	3.425	3.4
s29	-	-	-	2.85	3.850	3.45
s30	-	-	-	3.4	3.900	4.05
s31	-	-	-	3.8	3.975	3.95
s32	-	-	-	3.95	3.825	3.75
s33	-	-	-	4	3.650	3.4
s34	-	-	-	3.95	3.250	3.0
s35	-	-	-	3.8	2.650	2.325
s36	-	-	-	3.4	1.975	1.4
s37	-	-	-	2.85	-	1.425
s38	-	-	-	1.95	-	2.325
s39	-	-	-	-	-	2.95
s40	-	-	-	-	-	3.425
s41	-	-	-	-	-	3.75
s42	-	-	-	-	-	3.95
s43	-	-	-	-	-	3.85
s44	-	-	-	-	-	3.80
s45	-	-	-	-	-	3.575
s46	-	-	-	-	-	3.125
s47	-	-	-	-	-	2.425
s48	-	-	-	-	-	1.45

Table 3.7 Estimated sensor readings for full flow model based on the path length model

3.6.4.2 Optical attenuation model

The sensor readings based on equation (3.1) for various projections for the optical attenuation model in the case of the full flow model are tabulated in table 3.8.

<i>Sensor Number</i>	<i>Estimated sensor's reading (V)</i>					
	2 Ortho-gonal	2 Recti-linear	1 Orthogonal/2 Rectilinear	2 Orthogonal/2 Rectilinear	3 fan-beam	4 fan-beam
s1	0.4919	0.4848	0.4919	0.4919	0.4286	0.4286
s2	0.6966	0.6385	0.6966	0.6966	0.5686	0.5686
s3	0.829	0.749	0.829	0.829	0.6816	0.6816
s4	0.8913	0.829	0.8913	0.8913	0.788	0.788
s5	0.8913	0.8785	0.8913	0.8913	0.835	0.835
s6	0.829	0.8913	0.829	0.829	0.8913	0.8913
s7	0.6966	0.8785	0.6966	0.6966	0.8111	0.8111
s8	0.4919	0.829	0.4919	0.4919	0.829	0.829
s9	0.4919	0.749	0.499	0.4919	0.771	0.771
s10	0.6966	0.6385	0.7017	0.6966	0.6526	0.6526
s11	0.829	0.4848	0.829	0.829	0.5524	0.5524
s12	0.8913	0.4848	0.8978	0.8913	0.4509	0.4509
s13	0.8913	0.6385	0.9109	0.8913	0.3872	0.438
s14	0.829	0.749	0.823	0.829	0.5405	0.5853
s15	0.6966	0.829	0.7017	0.6966	0.6669	0.6916
s16	0.4919	0.8785	0.4919	0.4919	0.7599	0.7766
s17	-	0.8913	0.499	0.4848	0.8411	0.7766
s18	-	0.8785	0.6966	0.6385	0.817	0.6385
s19	-	0.829	0.829	0.749	0.9043	0.2835
s20	-	0.749	0.8978	0.829	0.8785	0.2835
s21	-	0.6385	0.9043	0.8785	0.7544	0.2835
s22	-	0.4848	0.829	0.8913	0.6526	0.2835
s23	-	-	0.7068	0.8785	0.5288	0.2835
s24	-	-	0.4919	0.829	0.4044	0.2835
s25	-	-	-	0.749	0.4044	0.2835
s26	-	-	-	0.6385	0.5484	0.2835
s27	-	-	-	0.4848	0.6669	0.3207
s28	-	-	-	0.4848	0.7654	0.4015
s29	-	-	-	0.6385	0.8658	0.4641
s30	-	-	-	0.749	0.8785	0.499
s31	-	-	-	0.829	0.8978	0.5027
s32	-	-	-	0.8785	0.8596	0.4778
s33	-	-	-	0.8913	0.817	0.4255
s34	-	-	-	0.8785	0.7276	0.3498
s35	-	-	-	0.829	0.6114	0.5564
s36	-	-	-	0.749	0.5027	0.4255
s37	-	-	-	0.6385	-	0.4286
s38	-	-	-	0.4848	-	0.5564
s39	-	-	-	-	-	0.6669
s40	-	-	-	-	-	0.7654
s41	-	-	-	-	-	0.8411
s42	-	-	-	-	-	0.8913
s43	-	-	-	-	-	0.8658
s44	-	-	-	-	-	0.8534
s45	-	-	-	-	-	0.7995
s46	-	-	-	-	-	0.7017
s47	-	-	-	-	-	0.5727

s48	-	-	-	-	-	0.4317
-----	---	---	---	---	---	--------

Table 3.8 Estimated sensor readings for full flow model based on the optical attenuation model

3.7 Basic layergram back-projection (LYGBP) technique

To produce a cross sectional image from the measurements of the object, a reconstruction process is needed. Many types of reconstruction techniques can be encountered in the papers and books on tomography [Plaskowski et al, 1995]. The layergram back-projection technique is a simple "layergram", where projections are back projected into the image plane from different angles and superimposed [Xie, 1993].

Suppose the object distribution on a cross section is as shown in figure 3.11a(i). The two projections of the object taken in perpendicular directions can be expressed by two one dimensional arrays $V_1(I)$ and $V_2(I)$, with the sample values in each projection as their components. To back project V_1 , each sample is painted as a straight strip running through the whole cross section in the direction of the projection being taken, and V_2 is back projected in the same way. Since the directions of the two projections are perpendicular, such a back-projection procedure produces an image composed of orthogonal grids (figure 3.11a (iii)). Similarly, this image can be expressed as two dimensional array $Img(U,V)$, where U is the line index of the grid and V the column, with the values of each grid as its components. By filtering $Img(U,V)$ with an appropriate threshold level, an image that is an approximation of the real field can be obtained (figure 3.11a (iv)).

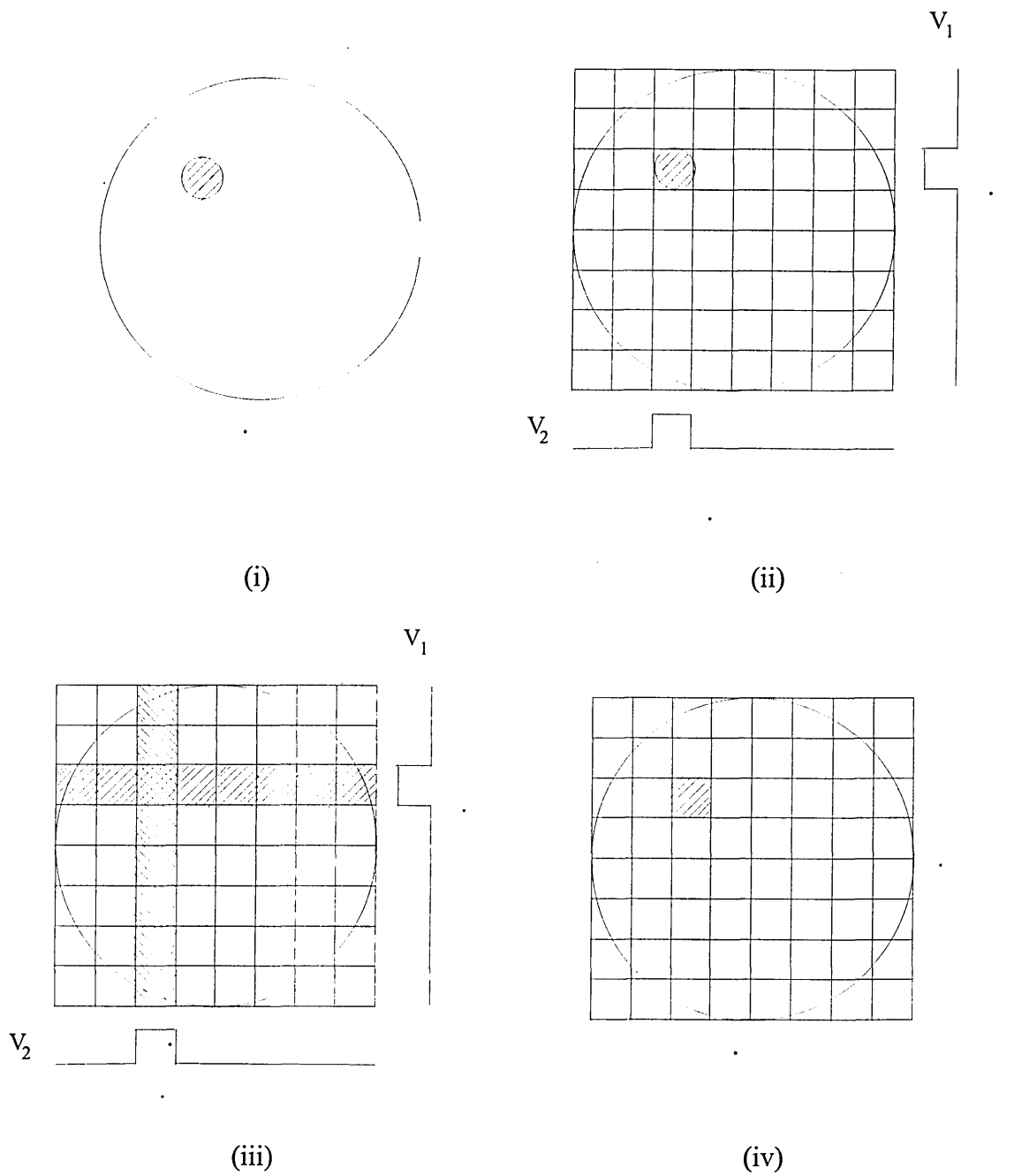


Figure 3.11a Basic layergram back-projection (LYGBP): (i) Original cross section; (ii) Two projections of object; (iii) Projection layergram; and (iv) Reconstructed cross section image.

For this project the back-projection algorithm is in the form of a "layergram" [Xie, 1993] where the concentration profile is generated by combining the voltage reading from each sensor (measured data) with its computed sensitivity map. To reconstruct the image, each sensitivity map matrix is multiplied by its corresponding sensor reading.

This results in $n \times 8 \times 8$ matrices, where n is the number of sensors. Corresponding terms in these matrices are summed and divided by the sum of the sensitivity coefficients to provide the back projected voltage distributions. This process can be expressed mathematically as shown in equation (3.9)

$$V_{ij} = \frac{\sum_{n=1}^{n=m} V_{s_n} S_n}{\sum_{n=1}^{n=m} S_n} \quad (3.9)$$

where

V_{ij} = voltage distribution in 8×8 matrix

V_{s_n} = voltage for n th sensor

s_n = sensitivity map for n th sensor in the form of an 8×8 matrix.

m = the total number of sensors used.

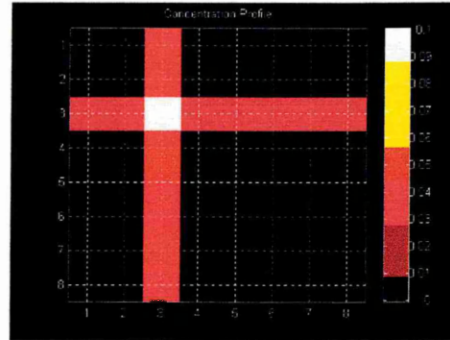
The voltage distributions, V_{ij} should be converted to concentration values. However, this has not been done for this section as it only requires rescaling of the voltage distributions. The voltage distributions are available as matrices (useful for quantitative information). The values in the matrix can be represented either on grey levels or in colour to provide an image. The resulting images are termed grey level images or pseudo colour images respectively [Plaskowski et al, 1995].

These images may be improved by filtering and thresholding. Thresholding causes problems since bubble amplitude varies and causes V_s to fluctuate. High pass filtering can improve the edges of the image. These filters may take the form of convolution-filter masks. A typical 3×3 high pass mask is shown below [Plaskowski et al, 1995]

$$\begin{bmatrix} -1 & -1 & -1 \\ -1 & 9 & -1 \\ -1 & -1 & -1 \end{bmatrix}$$

This filter is applied to the centre of the single pixel image shown in figure 3.11b (or figure 3.17a) and the results are shown in matrix 3.10.1.0 and figure 3.11c.

0	0	0.05	0	0	0	0	0
0	0	0.05	0	0	0	0	0
0.05	0.05	0.1	0.05	0.05	0.05	0.05	0.05
0	0	0.05	0	0	0	0	0
0	0	0.05	0	0	0	0	0
0	0	0.05	0	0	0	0	0
0	0	0.05	0	0	0	0	0
0	0	0.05	0	0	0	0	0



Matrix representing unfiltered LYGBP

Figure 3.11b Unfiltered LYGBP for two orthogonal projections: single pixel flow model

x	x	x	x	x	x	x	x
x	-0.3	0.2	-0.3	-0.15	-0.15	-0.15	x
x	0.2	0.7	0.2	0.35	-0.15	-0.15	x
x	-0.3	0.2	-0.3	-0.15	-0.15	-0.15	x
x	-0.15	0.35	-0.15	0	0	0	x
x	-0.15	0.35	-0.15	0	0	0	x
x	-0.15	0.35	-0.15	0	0	0	x
x	x	x	x	x	x	x	x

Matrix 3.10.1.0

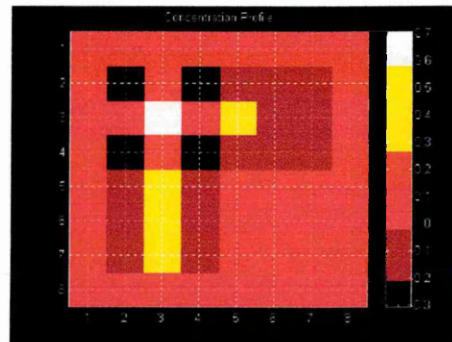


Figure 3.11c Filtered LYGBP for two orthogonal projections: single pixel flow model

The results of this filter show some improvement over the unfiltered LYGBP. Further filtering may be carried out on the resulting images and the filter may take other values, however, in this thesis a different approach is investigated.

This alternative approach is termed the hybrid algorithm. This is a hybrid algorithm because it combines knowledge of sensors which indicate zero with the normal

layergram technique. The reconstruction is as follows. All the sensors are sampled. If a sensor reads zero, then all pixels associated with it are fixed at zero until a new sample is taken. Calculations are then made using the layergram back-projection to determine the remaining pixel contents. This approach produces pixels with zero content without using either pixel thresholding or filtering. Compared to a filtered layergram, the hybrid algorithm uses less calculations which is necessary in order to do on line velocity correlation of pixel concentrations.

3.8 Modelling of optical fibre

For optical fibre sensors the way both ends of the fibre are terminated is important as the termination effects both the acceptance and emission angles of the light energy. A fibre collimator/focuser is a suitable tool to couple light in and out of optical devices by collimating light or focusing light exiting a fibre to a desired beam diameter or spot size [Fiber Collimators/Focusers, 1998]. However, the cost of a collimator/focuser is expensive and this project requires many collimators/focusers and hence, it was not utilised; an alternative method has to be developed which is cheaper and yet effective in collimating the light beam.

In a previous project carried out by Ramli [Ramli, 1998], the fibre optic lens was modelled for three combinations of fibre optic terminations: (a) flat - flat, (b) flat - lensed, and (c) lensed - lensed. In the lensed - lensed model, it was assumed that the radii for both ends are identical. In the following model (figure 3.12), the radii of the fibre optic lenses are different and only the receiver fibre is modelled as the transmitter utilises light projectors. The main objective is to determine the relationship between the lens curvature and the divergence of the output beam.

The maximum output divergence of the beam coming out of the fibre optic is represented by the emission angle, θ_0 . It is undesirable to have a large divergent beam, because it reduces the energy centred in the beam and can reduce the optical energy being transmitted to the individual receivers.

The fibre cladding is neglected in the modelling, as it is assumed that it is thin compared to the central fibre. However, it is noted that total internal reflection occurs inside the fibre due to the cladding material. The refractive index of the core is higher than that of the cladding, so light in the core that strikes the boundary with the cladding at an angle in excess of the critical angle is confined in the core by total internal reflection [Hecht, 1999].

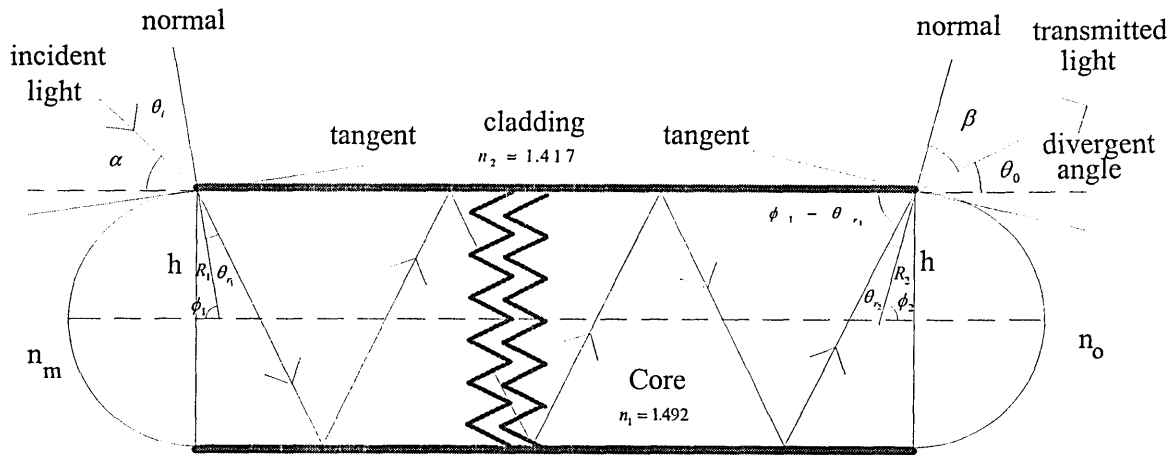


Figure 3.12 A side view of the fibre optic model

The following symbols are designated for various parameters associated with light and the properties of the optical fibre :

α = the angle between the incident light and the horizontal axis.

θ_i = the incident angle.

β = angle of transmitted light (emergent ray).

θ_0 = divergent angle or angle between the incident light and the horizontal axis.

n_m = refractive index of the medium (i.e. air) in front of the front end of the fibre = 1.

n_1 = refractive index of the optical fibre core.

n_2 = refractive index of the fibre cladding.

n_0 = refractive index of the medium (i.e. air) after the optical fibre = 1.

h = radius of the fibre optic core = 0.5 mm.

R_1 = radius of the lens at the front end of the fibre optic.

R_2 = radius of the lens at the back end of the fibre optic.

θ_{r_1} , θ_{r_2} , ϕ_1 and ϕ_2 are construction angles shown on figure 3.12.

Consider a ray of light incident on the edge of the fibre.

Applying Snell's law,

$$n_m \sin \theta_i = n_1 \sin \theta_{r_1}$$
$$\theta_{r_1} = \sin^{-1} \left(\frac{n_m \sin \theta_i}{n_1} \right) \quad (3.10)$$

The incident angle of the light, θ_i , must be smaller or equal to the acceptance angle of the fibre, 28° , to ensure that total internal reflection occurs. The refracted ray inside the optical fibre is continuously reflected along the fibre until it reaches the other end of the fibre.

$$\sin \phi_1 = \frac{h}{R_1}$$
$$\phi_1 = \sin^{-1} \left(\frac{h}{R_1} \right) \quad (3.11)$$

Applying Snell's law again,

$$n_1 \sin \theta_{r_2} = n_0 \sin \beta$$

$$\beta = \sin^{-1}\left(\frac{n_1}{n_0} \sin \theta_{r_2}\right) \quad (3.12)$$

$$\sin \phi_2 = \frac{h}{R_2}$$

$$\phi_2 = \sin^{-1}\left(\frac{h}{R_2}\right) \quad (3.13)$$

Divergent angle, $\theta_0 = \phi_2 - \beta$

$$\theta_0 = \sin^{-1}\left(\frac{h}{R_2}\right) - \sin^{-1}\left(\frac{n_1}{n_0} \sin \theta_{r_2}\right) \quad (3.14)$$

$$90 - (\phi_1 - \theta_{r_1}) = \theta_{r_2} + (90 - \phi_2)$$

$$\theta_{r_2} = \phi_2 - \phi_1 + \theta_{r_1}$$

From (3.10),(3.11) and (3.13),

$$\theta_{r_2} = \sin^{-1}\left(\frac{h}{R_2}\right) - \sin^{-1}\left(\frac{h}{R_1}\right) + \sin^{-1}\left(\frac{n_m}{n_1} \sin \theta_i\right)$$

From (3.14),

$$\theta_0 = \sin^{-1}\left(\frac{h}{R_2}\right) - \sin^{-1}\left[\frac{n_1}{n_0} \sin\left(\sin^{-1}\left(\frac{h}{R_2}\right) - \sin^{-1}\left(\frac{h}{R_1}\right) + \sin^{-1}\left(\frac{n_m \sin \theta_i}{n_1}\right)\right)\right] \quad (3.15)$$

Suitable values for R_1 and R_2 , in order to produce a collimated output beam are 0.8 mm and 0.63 mm respectively.

3.9 Modelling of flow pipe

Three possible arrangements for the collimated light entering the flow pipe are considered:-

(1) The light enters a transparent cylindrical flow pipe.

(2) The light enters a transparent cylindrical flow pipe enclosed by a square-shaped transparent perspex box.

(3) The light enters a square-shaped transparent perspex section which forms part of the flow pipe.

In order to assess which arrangement can minimise refraction of the collimated light entering the pipe and the measurement cross-section, the effect of using each arrangement is studied. It is assumed that the thickness of the cylindrical pipe wall and the square-shaped perspex is negligible. The maximum divergent angle of the light projector is assumed to be 2.15° (measured using the light source).

Transparent perspex in the form of sheets and rods are widely used for aircraft windows. It has outstanding optical properties and weatherability and is easily machined. Colourless perspex is as transparent as the finest plate glass and is capable of giving almost complete transmittance of visible light. It has white light transmittance of up to 92%, with the remaining 8% being the reflection loss [Abel & Thomas, 1988]. As such perspex is a suitable material to be used as an enclosure for the measurement section.

3.9.1 Light entering a transparent cylindrical flow pipe

Figure 3.13 shows light paths in air, inside a flow pipe containing water and going out of the flow pipe into air. For simplicity, the thickness of the flow pipe is ignored. The maximum divergent angle of the light projector is 2.15° . The diagram shows that two out of three light paths going out of the flow pipe into air have an angle of refraction (i.e. 51.4° and 33.5°) greater than 28° which is the acceptance angle of the EH4001 fibre

optic. This arrangement is not suitable as a tomographic system as some views will be not be 'captured' by the optical fibre receivers facing the light projectors.

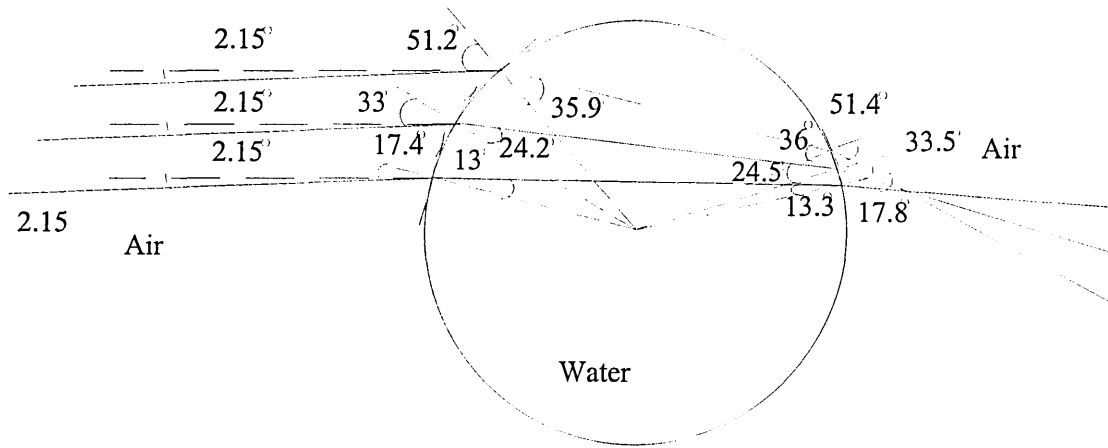


Figure 3.13 Light entering a transparent cylindrical flow pipe

3.9.2 Light entering a cylindrical flow pipe enclosed by a transparent perspex square

Figure 3.14 shows the light paths in air, inside the transparent perspex square and the flow pipe containing water and finally out into the air again. Again for simplicity, the thickness of the flow pipe is ignored. It clearly shows that not all of the outgoing light comes out from the exit side of the perspex as shown by one of the light paths going out of the top of the perspex. As such, this arrangement is not suitable because some light will be missed by the optical fibre receivers which are placed facing towards the light projectors and some vital information pertaining to the flow will be lost.

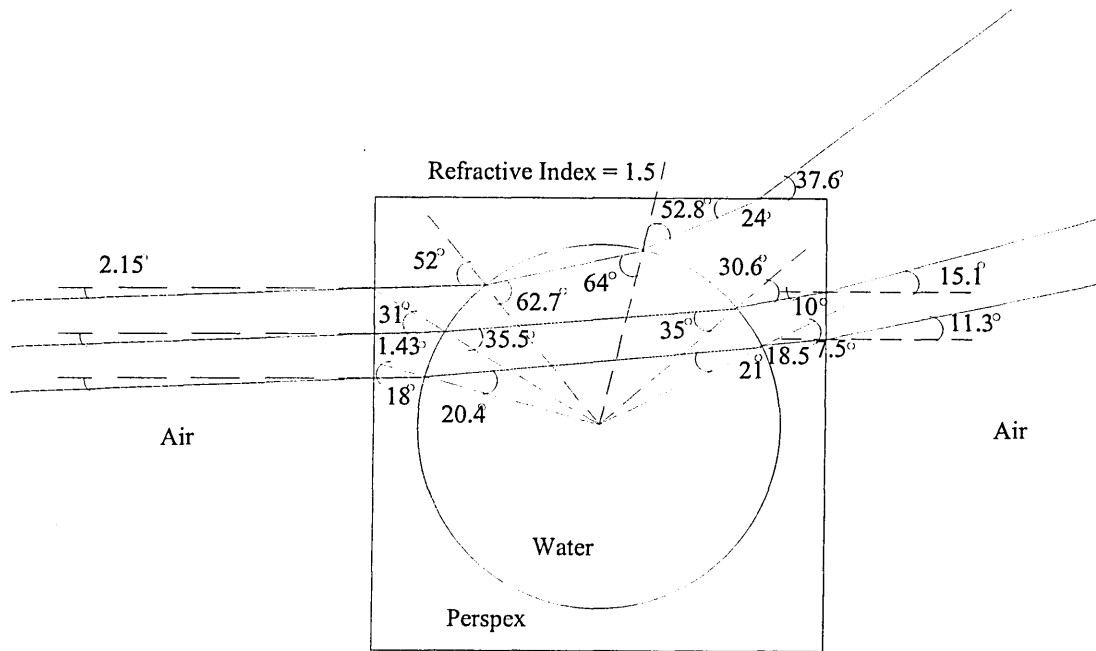


Figure 3.14 Light entering a cylindrical flow pipe enclosed by a transparent perspex square

3.9.3 Light entering a hollow perspex square moulded onto the flow pipe

It can be seen in figure 3.15 that light coming out of the perspex square has the same angle as when it enters the box when the perspex box is filled with fluid. The EH 4001 optical fibre receivers have an acceptance angle of 28° and are able to receive all the light coming out of the perspex box. This is the best arrangement compared to the two previous arrangements discussed in sections 3.8.1 and 3.8.2. This is the arrangement selected for the experimental aspects of this project.

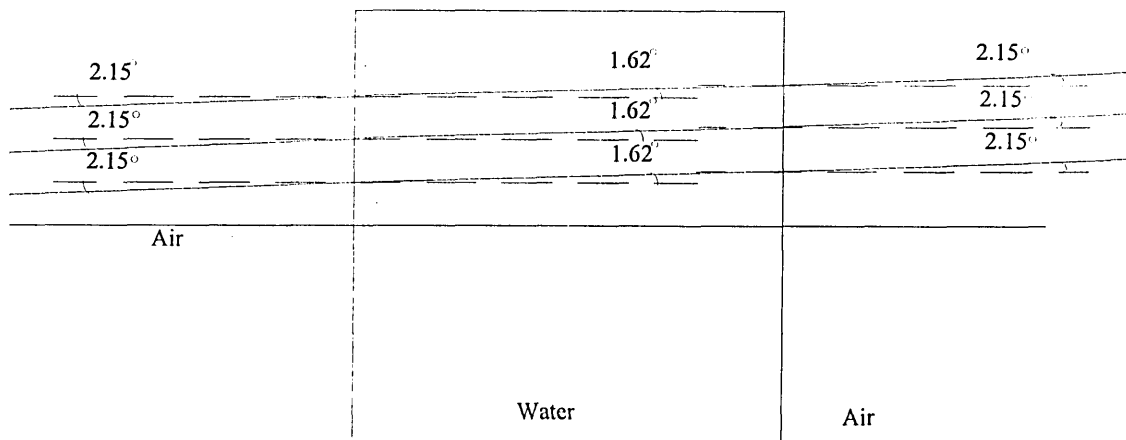


Figure 3.15 Light entering a hollow perspex square moulded onto the flow pipe

3.10 Cross correlation

To determine volume flow rates of gases experimentally using tomographic measurements it is necessary to combine concentration and velocity profiles. To measure velocity, cross-correlation is used.

The flowmeter employs two arrays of optical fibre sensors which are utilised to monitor the flow, one being positioned downstream of the other. The output signal of each sensor is modulated by the conveyed particles or droplets, in an apparently random manner. However, assuming that the arrangement of particles or droplets remains constant between sensors, the signal generated by the downstream sensor is a time-delayed replica of the upstream sensor's output (in practice the arrangement of particles or droplets changes but there is a recognisable part of the pattern conveyed between the sensors).

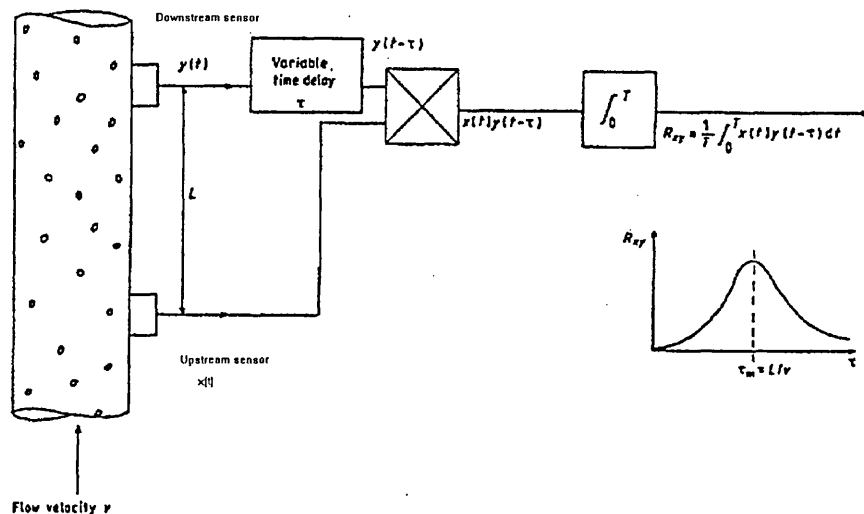


Figure 3.16 Cross-correlation of upstream and downstream sensors

If $x(t)$ and $y(t)$ represent the signals from the upstream and downstream sensors respectively, then the cross correlation function of $x(t)$ and $y(t)$ is given as:

$$R(\tau) = \lim_{T \rightarrow \infty} \frac{1}{T} \int_0^T x(t)y(t - \tau)dt$$

The peak in the $R(\tau)$ versus time plot corresponds to the most probable time required for the flow to travel between the upstream and downstream sensors, τ_m . Hence, the mean flow velocity can be obtained from the following expression:

$$V = \frac{L}{\tau_m} \quad (m / s)$$

where L is the spacing between upstream and downstream sensors.

The following operations are carried out by the optical tomography system :

(a) Analogue flow noise signals generated by the flowmeter's two arrays of sensors are converted into digital form and concentration profiles determined, which are then used to enable their cross-correlation function to be computed.

(b) The cross-correlation function of these two signals is computed and the peak position of the resulting correlogram is detected to give an estimate of the fluid transit time between the two sensors. The time delay of the maximum value of the cross correlation function gives an indication of the flow transit time between upstream and downstream pixels. This process is repeated for all the pixels enabling the actual flow velocity profile to be obtained.

A programme coded in MATLAB cross-correlates two different sets of data (ie pixel concentration profiles). Experiments were carried out to capture data from the sensors

using the data acquisition system and the data is processed using off line to obtain the cross correlation function. The computation requires two sets of data as inputs in order to perform the cross correlation. The programme listing is as follows:-

```
function x=kxcorr(u,y);
if nargin~=2,
    error('kxcorr must have two arguments')
end
L=length(u);
if length(y)~=L,
    error('kxcorr - arguments are not of the same length')
end
for i=1:L
    if i==1,
        ushft=u;
    else
        ushft=[ushft(L,1);ushft(1:L-1,1)];
    end
    x(i)=sum(y.*ushft)/L;
end

plot(x)
x=x';
[z,it]=max(x)
v=0.15/(it*0.01)
```

In the above programme, data from the upstream sensor are represented by u whereas the downstream sensor is represented by y. The programme will only proceed if the data length of both u and y are the same. x represents the cross correlation function. The method used to calculate the cross-correlation function is a point-to-point method. The

maximum value of matrix x is computed using the command $[z,it]=\max(x)$ in which z is the value of the maximum cross correlation coefficient and 'it' is the index time corresponding to the z value. The distance between the upstream and downstream sensors is 0.15m. Hence, the velocity of the bubbles is

$$v=0.15/(it*0.01)$$

in which 0.01 is the sampling time (sampling frequency of 100 Hz).

3.11 Results of LYGBP using the path length model

This section presents results obtained using modelling for several types of projection systems using the path length model. The results are presented as follows :-

- (a) Results for two orthogonal projections are shown in sections 3.10.1 and 3.10.2.
- (b) Results for a combination of two orthogonal and two rectilinear projections are shown in section 3.10.3.
- (c) Results for three fan-beam projections are shown in section 3.10.4.

Results for two rectilinear, a combination of one orthogonal and two rectilinear, and four-fan beam projections systems are presented in Appendix A.

3.11.1 Results for two orthogonal projections system

In this section the results of implementing LYGBP (section 3.6) are presented for the two orthogonal projections system for four flow models :-

- (a) Single pixel flow model.
- (b) Two pixels flow model.
- (c) Half-flow model.
- (d) Full-flow model.

All results presented in this section are discussed in section 3.14.

3.11.1.1 Single pixel flow model

If the object is in the pixel P_{13} the matrix shown in matrix 3.10.1.1, is obtained after the products of the sensitivity matrices and voltages for each sensor are summed (section 3.6). The numerical values of matrix 3.10.1.1 are converted to a grey scale range where white represents the maximum value in the matrix and black zero. This plot is shown in figure 3.17a.

$$\begin{bmatrix} 0 & 0 & 0.05 & 0 & 0 & 0 & 0 & 0 \\ 0 & 0 & 0.05 & 0 & 0 & 0 & 0 & 0 \\ 0.05 & 0.05 & 0.1 & 0.05 & 0.05 & 0.05 & 0.05 & 0.05 \\ 0 & 0 & 0.05 & 0 & 0 & 0 & 0 & 0 \\ 0 & 0 & 0.05 & 0 & 0 & 0 & 0 & 0 \\ 0 & 0 & 0.05 & 0 & 0 & 0 & 0 & 0 \\ 0 & 0 & 0.05 & 0 & 0 & 0 & 0 & 0 \\ 0 & 0 & 0.05 & 0 & 0 & 0 & 0 & 0 \end{bmatrix}$$

Matrix 3.10.1.1

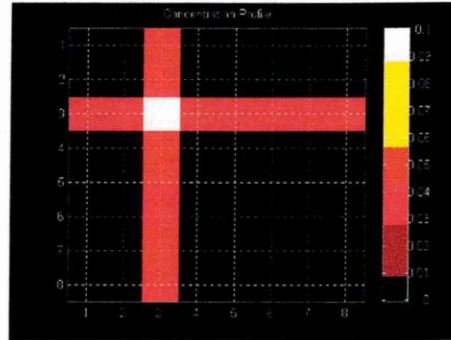


Figure 3.17a LYGBP for two orthogonal projections: single pixel flow model

3.11.1.2 Two pixels flow model

Matrix 3.10.1.2 represents the calculated concentration profiles for the two pixels flow model. The plot of matrix 3.10.1.2 is shown in figure 3.17b.

$$\begin{bmatrix} 0 & 0 & 0.05 & 0 & 0 & 0.05 & 0 & 0 \\ 0 & 0 & 0.05 & 0 & 0 & 0.05 & 0 & 0 \\ 0.05 & 0.05 & 0.1 & 0.05 & 0.05 & 0.1 & 0.05 & 0.05 \\ 0 & 0 & 0.05 & 0 & 0 & 0.05 & 0 & 0 \\ 0 & 0 & 0.05 & 0 & 0 & 0.05 & 0 & 0 \\ 0.05 & 0.05 & 0.1 & 0.05 & 0.05 & 0.1 & 0.05 & 0.05 \\ 0 & 0 & 0.05 & 0 & 0 & 0.05 & 0 & 0 \\ 0 & 0 & 0.05 & 0 & 0 & 0.05 & 0 & 0 \end{bmatrix}$$

Matrix 3.10.1.2

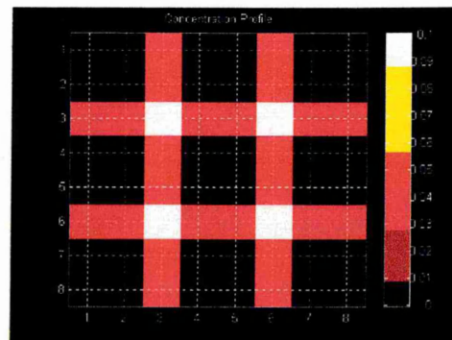


Figure 3.17b LYGBP for two orthogonal projections: two pixels flow model

3.11.1.3 Half flow model

For the half-flow model, matrix 3.10.1.3 is obtained after the products of the sensitivity matrices and voltages for each sensor are summed. The plot of matrix 3.10.1.3 is shown in figure 3.17c.

$$\begin{bmatrix} 0 & 0.17 & 0.44 & 0.56 & 0.11 & 0.11 & 0 & 0 \\ 0.09 & 0.54 & 0.51 & 0.55 & 0.16 & 0.16 & 0.18 & 0.09 \\ 0.39 & 0.49 & 0.53 & 0.57 & 0.18 & 0.18 & 0.18 & 0.16 \\ 0.45 & 0.51 & 0.55 & 0.60 & 0.20 & 0.20 & 0.20 & 0.22 \\ 0.45 & 0.51 & 0.55 & 0.60 & 0.20 & 0.20 & 0.20 & 0.22 \\ 0.39 & 0.49 & 0.53 & 0.57 & 0.18 & 0.18 & 0.18 & 0.16 \\ 0.09 & 0.54 & 0.51 & 0.55 & 0.16 & 0.16 & 0.18 & 0.09 \\ 0 & 0.17 & 0.44 & 0.56 & 0.11 & 0.11 & 0 & 0 \end{bmatrix}$$

Matrix 3.10.1.3

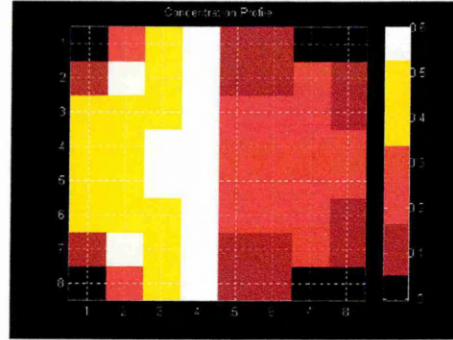


Figure 3.17c LYGBP for two orthogonal projections: half flow model

3.11.1.4 Full flow model

For the full flow model, the matrix 3.10.1.4 is obtained after the implementation of the LYGBP algorithm. The plot of matrix 3.10.1.4 is shown in figure 3.17d.

$$\begin{bmatrix} 0 & 0.17 & 0.56 & 0.68 & 0.68 & 0.56 & 0.17 & 0 \\ 0.17 & 0.72 & 0.66 & 0.71 & 0.71 & 0.66 & 0.72 & 0.17 \\ 0.56 & 0.66 & 0.70 & 0.75 & 0.75 & 0.70 & 0.66 & 0.56 \\ 0.68 & 0.71 & 0.75 & 0.80 & 0.80 & 0.75 & 0.71 & 0.68 \\ 0.68 & 0.71 & 0.75 & 0.80 & 0.80 & 0.75 & 0.71 & 0.68 \\ 0.56 & 0.66 & 0.70 & 0.75 & 0.75 & 0.70 & 0.66 & 0.56 \\ 0.17 & 0.72 & 0.66 & 0.71 & 0.71 & 0.66 & 0.72 & 0.17 \\ 0 & 0.17 & 0.56 & 0.68 & 0.68 & 0.56 & 0.17 & 0 \end{bmatrix}$$

Matrix 3.10.1.4

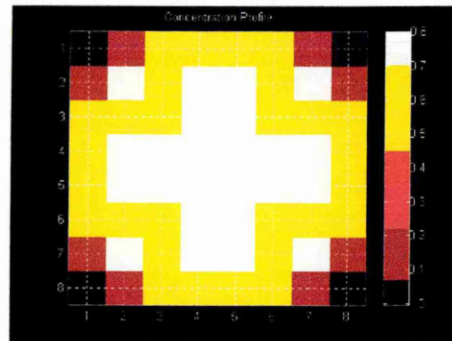


Figure 3.17d LYGBP for two orthogonal projections: full flow model

3.11.3 Results of the combination of two orthogonal and two rectilinear projections system

In this section the results of implementing LYGBP are presented for the combination of two orthogonal and two rectilinear projection systems in the case of the path length model for the same four flow models as in section 3.10.1. All results in this section are discussed in section 3.14. The plots of the single pixel flow, two pixels flow, half flow and full flow models using the LYGBP algorithm are shown in figures 3.18a, 3.18b, 3.18c and 3.18d respectively.

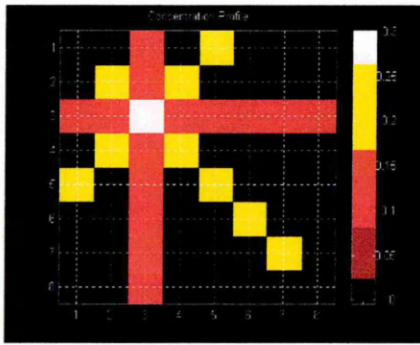


Figure 3.18a LYGBP for a combination of two orthogonal and two rectilinear projections: single pixel flow model

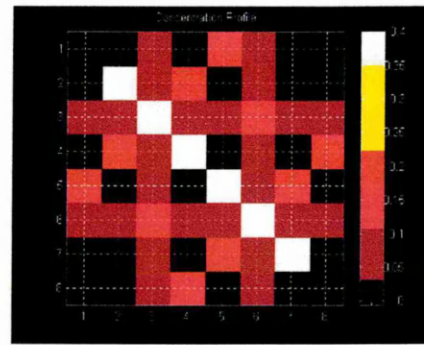


Figure 3.18b LYGBP for a combination of two orthogonal and two rectilinear projections: two pixels flow model

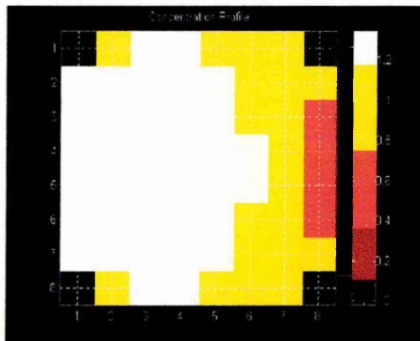


Figure 3.18c LYGBP for a combination of two orthogonal and two rectilinear projections: half flow model

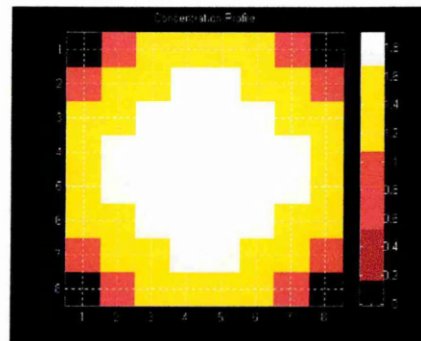


Figure 3.18d LYGBP for a combination of two orthogonal and two rectilinear projections: full flow model

3.11.4 Results for three fan-beam projections system

In this section the results of implementing LYGBP are presented for the three fan-beam projections system for the same four flow models as in section 3.10.1. All results in this section are discussed in section 3.14. The plots of the single pixel flow, two pixels flow, half flow and full flow models using the LYGBP algorithm are shown in figures 3.19a, 3.19b, 3.19c and 3.19d respectively.

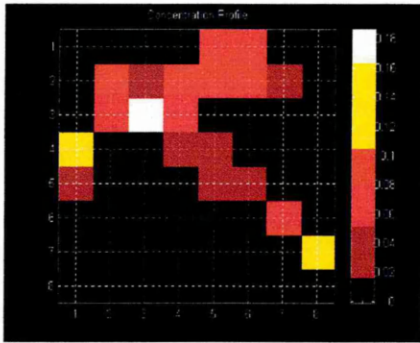


Figure 3.19a LYGBP for three fan-beam projections: single pixel flow model

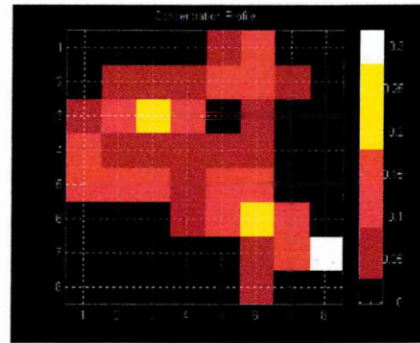


Figure 3.19b LYGBP for three fan-beam projections: two pixels flow model

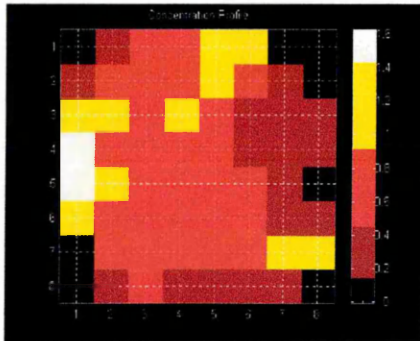


Figure 3.19c LYGBP for three fan-beam projections: half flow model

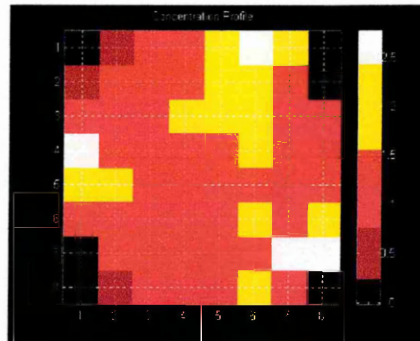


Figure 3.19d LYGBP for three fan-beam projections: full flow model

3.12 Results of LYGBP using the optical attenuation model

This section presents results for several types of projection systems using the optical attenuation model. The results are divided into several parts :-

- (a) Results for two orthogonal projections are in section 3.11.1.

- (b) Results for combination of two orthogonal and two rectilinear projections are presented in section 3.11.2.
- (c) Results for three fan-beam projections are presented in section 3.11.3.

Results for two rectilinear, a combination of one orthogonal and two rectilinear, and four-fan beam projections systems are given in Appendix B.

3.12.1 Results for two orthogonal projections system

In this section the results of implementing LYGBP are presented for the two orthogonal projections system for the same four flow models as in section 3.10.1. All results in this section are discussed in section 3.14. The plots of the single pixel flow, two pixels flow, half flow and full flow models using the LYGBP algorithm are shown in figures 3.20a, 3.20b, 3.20c and 3.20d respectively.

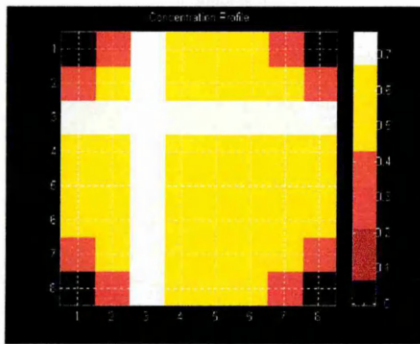


Figure 3.20a LYGBP for two orthogonal projections: single pixel flow model

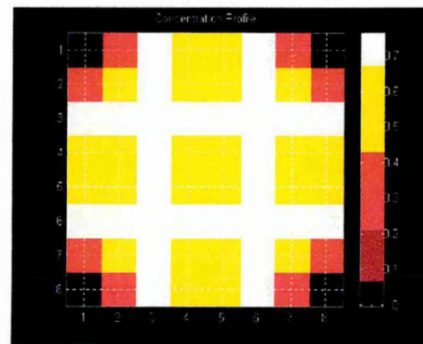


Figure 3.20b LYGBP for two orthogonal projections: two pixels flow model

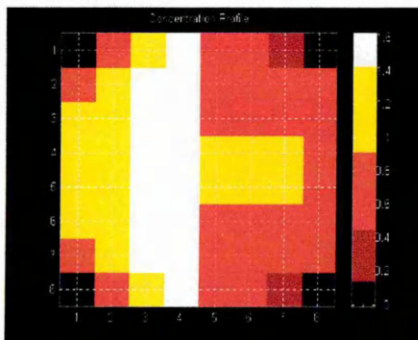


Figure 3.20c LYGBP for two orthogonal projections: half flow model.

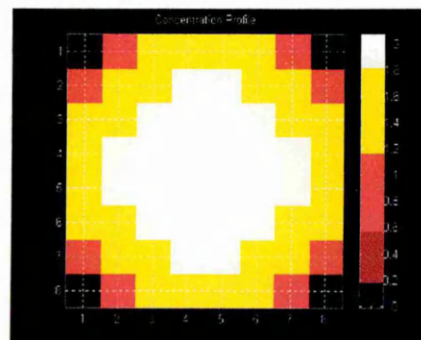


Figure 3.20d LYGBP for two orthogonal projections: full flow model

3.12.2 Results for a combination of two orthogonal and two rectilinear projections system

system

In this section the results of implementing LYGBP are presented for the combination of two orthogonal and two rectilinear projections system in the case of the optical attenuation model for the same four flow models as in section 3.10.1. All results in this section are discussed in section 3.14. The grey level plots of the single pixel flow, two pixels flow, half flow and full flow models using the LYGBP algorithm are shown in figures 3.21a, 3.21b, 3.21c and 3.21d respectively.

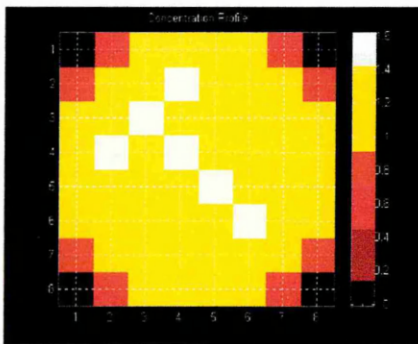


Figure 3.21a LYGBP for a combination of two orthogonal and two rectilinear projections: single pixel flow model

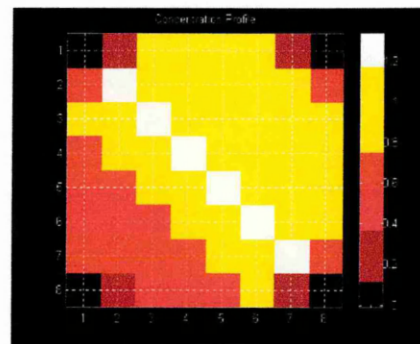


Figure 3.21b LYGBP for a combination of two orthogonal and two rectilinear projections: two pixels flow model

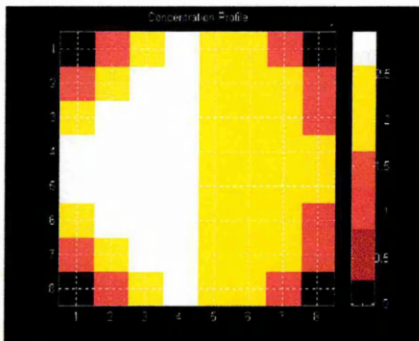


Figure 3.21c LYGBP for a combination of two orthogonal and two rectilinear projections: half flow model

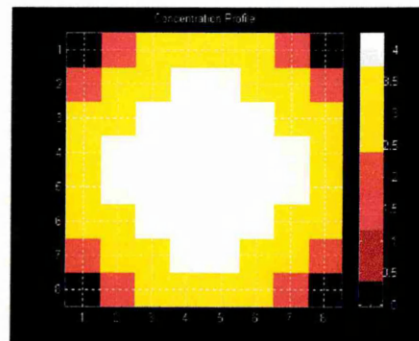


Figure 3.21d LYGBP for a combination of two orthogonal and two rectilinear projections: full flow model

3.12.3 Results for three fan-beam projections system

In this section the results of implementing LYGBP are presented for the three fan-beam projections system for the same four flow models as in section 3.10.1. All results in this section are discussed in section 3.14. The grey level plots of the single pixel flow, two pixels flow, half flow and full flow models using the LYGBP algorithm are shown in figures 3.22a, 3.22b, 3.22c and 3.22d respectively.

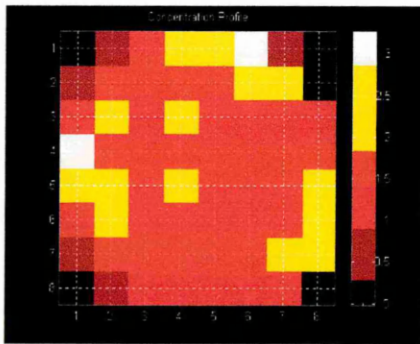


Figure 3.22a LYGBP for three fan-beam projections: single pixel flow model

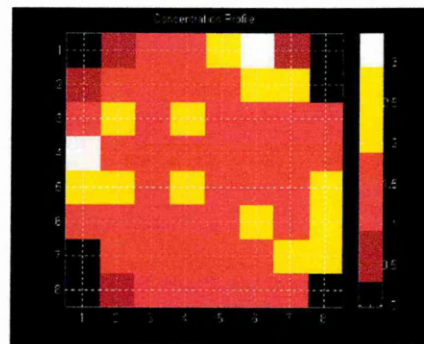


Figure 3.22b LYGBP for three fan-beam projections: two pixels flow model

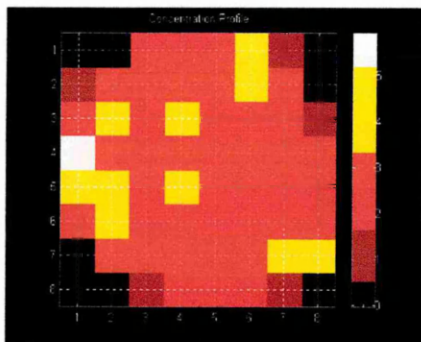


Figure 3.22c LYGBP for three fan-beam projections: half flow model

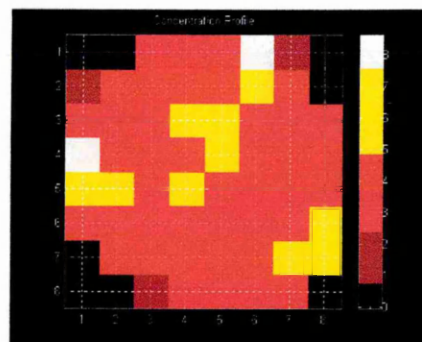


Figure 3.22d LYGBP for three fan-beam projections: full flow model

3.13 Results of LYGBP using a combination of optical attenuation model and signal conditioning

The optical attenuation modelling gives a very low contrast images due to its low sensitivity compared with the path length model. By combining both optical attenuation model and signal conditioning, the following operations will occur :-

When light does not intercept any bubbles/droplets, the sensor voltage will have a steady-state value of zero instead of the current minimum value of V_{\min} (0.2835 V).

Passage of a bubble or droplet through the beam produces a change in level, which can be amplified by the circuit (figure 4.14). This results in a large contrast in grey level between carrier and conveyed component.

This section presents results for several types of projection systems using the combination of optical attenuation model and signal conditioning. The results are divided into several parts :-

- (a) Results for two orthogonal projections are in section 3.12.1.
- (b) Results for combination of two orthogonal and two rectilinear projections are presented in section 3.12.2.
- (c) Results for three fan-beam projections are presented in section 3.12.3.

Results for two rectilinear, a combination of one orthogonal and two rectilinear, and four-fan beam projections systems are given in Appendix C.

3.13.1 Results for two orthogonal projections system

In this section the results of implementing LYGBP are presented for the two orthogonal projections system in the case of the combination of optical attenuation model and signal conditioning for the same four flow models as in section 3.10.1. All results in this section are discussed in section 3.14 . The grey level plots of the single pixel flow, two

pixels flow, half flow and full flow models using the LYGBP algorithm are shown in figures 3.23a, 3.23b, 3.23c and 3.23d respectively.

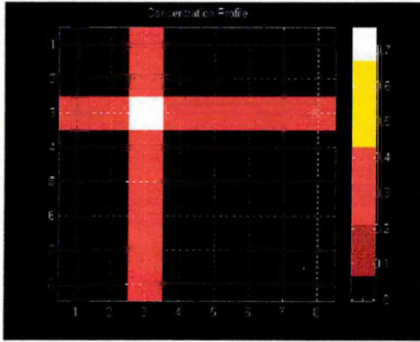


Figure 3.23a LYGBP for two orthogonal projections: single pixel flow model

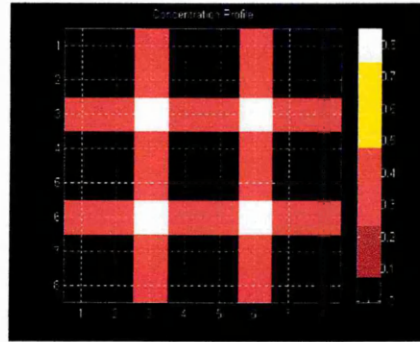


Figure 3.23b LYGBP for two orthogonal projections: two pixels flow model

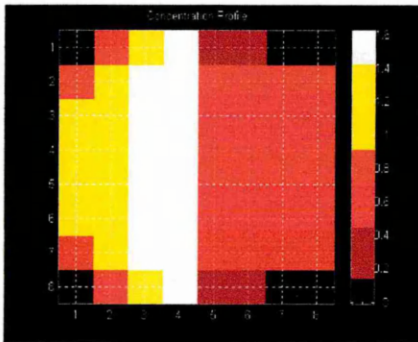


Figure 3.23c LYGBP for two orthogonal projections: half flow model

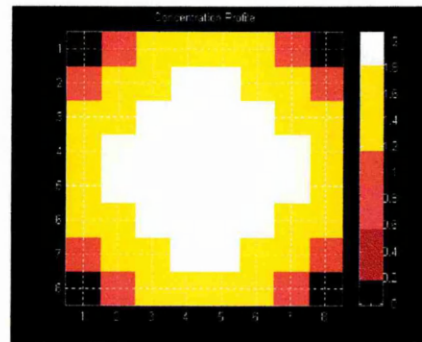


Figure 3.23d LYGBP for two orthogonal projections: full flow model

3.13.2 Results for a combination of two orthogonal and two rectilinear projections system

In this section the results of implementing LYGBP are presented for the combination of two orthogonal and two rectilinear projections system in the case of the combination of optical attenuation model and signal conditioning for the same four flow models as in section 3.10.1. All results in this section are discussed in section 3.14. The grey level plots of the single pixel flow, two pixels flow, half flow and full flow models using the LYGBP algorithm are shown in figures 3.24a, 3.24b, 3.24c and 3.24d respectively.

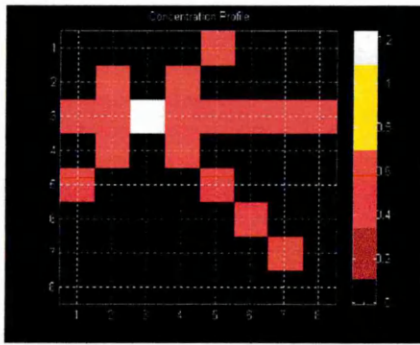


Figure 3.24a LYGBP for a combination of two orthogonal and two rectilinear projections: single pixel flow model

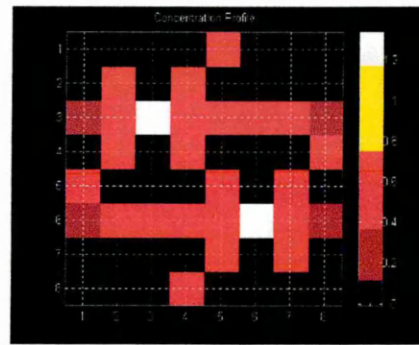


Figure 3.24b LYGBP for a combination of two orthogonal and two rectilinear projections: two pixels flow model

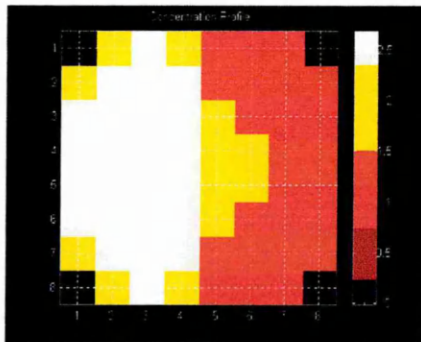


Figure 3.24c LYGBP for a combination of two orthogonal and two rectilinear projections: half flow model

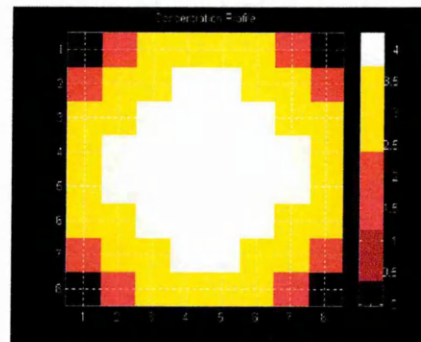


Figure 3.24d LYGBP for a combination of two orthogonal and two rectilinear projections: full flow model

3.13.3 Results for three fan-beam projections system

In this section the results of implementing LYGBP are presented for three fan-beam projections system in the case of the combination of optical attenuation model and electronic measurements for the same four flow models as in section 3.10.1. All results in this section are discussed in section 3.14. The grey level plots of the single pixel flow, two pixels flow, half flow and full flow models using the LYGBP algorithm are shown in figures 3.25a, 3.25b, 3.25c and 3.25d respectively.

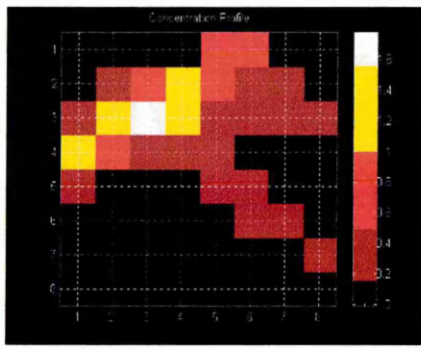


Figure 3.25a LYGBP for three fan-beam projections: single pixel flow model

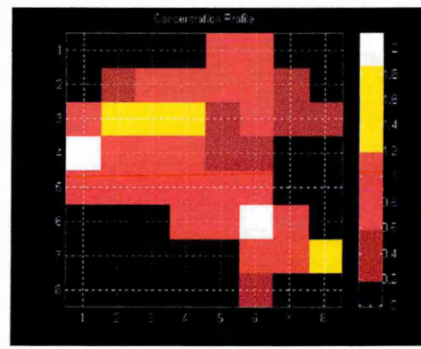


Figure 3.25b LYGBP for three fan-beam projections: two pixels flow model

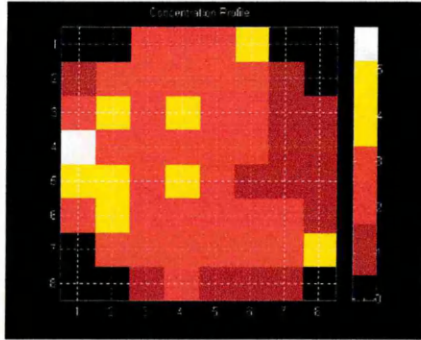


Figure 3.25c LYGBP for three fan-beam projections: half flow model

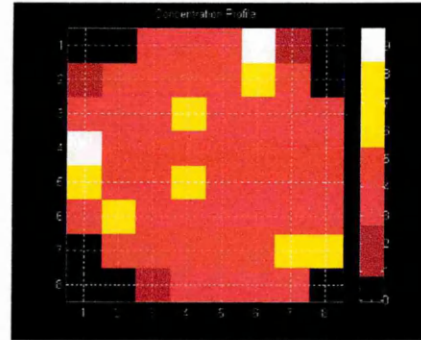


Figure 3.25d LYGBP for three fan-beam projections: full flow model

3.14 Hybrid reconstruction algorithm

Optical sensors are hard field sensors and so, in the models used for this thesis, the material in the flow is assumed only to vary the intensity of the received signal. For the optical sensor, when no objects block the path from transmitter to receiver, the sensor is designed to produce a zero output value, neglecting the effect of noise inherent in the system. This is taken into account in the development of a hybrid reconstruction algorithm which combines knowledge of sensor reading zero flow and LYGBP in order to improve the accuracy of the image reconstruction. This algorithm was developed using the C programming language. The programme is listed in Appendix F.

The algorithm is designed for two, three or four projections systems based on orthogonal and rectilinear projections. The algorithm initially assumes binary values from the sensors, either zero for no material or one for the presence of material. All pixels associated with sensors indicating zero are set and held at zero for the rest of the calculation. The LYGBP then uses numerical values as in section 3.6. Briefly, the steps involved in the algorithm are :-

- (1) Generate the sensitivity maps for the horizontal, vertical and diagonal sensors.
- (2) Initialise all sensors to zero.
- (3) Read in each sensor value.
- (4) If the sensor reading = 0, then any pixels traversed by that sensor's beam are set to zero and omitted from further calculations.
- (5) Perform LYGBP in the normal way.

The flow chart representing the steps involved in the algorithm is shown in figure 3.26.

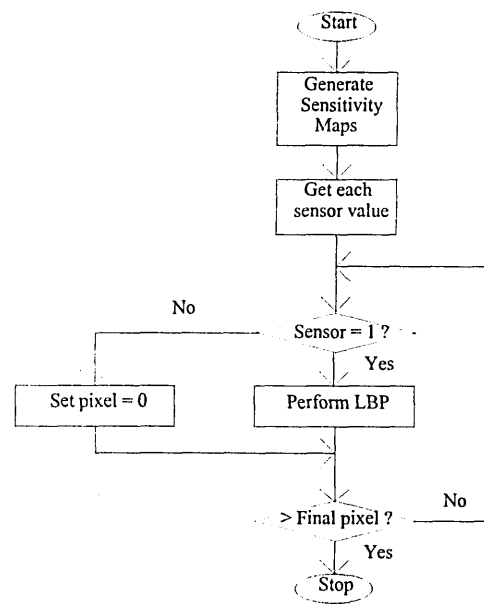


Figure 3.26 Flow chart for the hybrid reconstruction algorithm

This algorithm results in significant improvements in the measured errors. For two rectilinear projections the single pixel, half and full flow models are perfectly recovered i.e. accuracy is 100 %. However, with only two projections the two pixels model results in aliasing and four pixel images are produced (figure 3.27a). With the combination of two orthogonal and two rectilinear projections system all flow all flow models are fully reproduced (figure 3.27b).

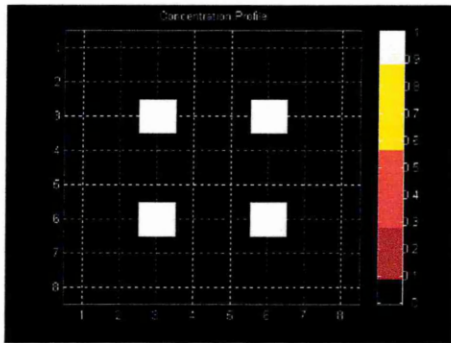


Figure 3.27a Two orthogonal projections and the hybrid reconstruction algorithm: two pixels flow model

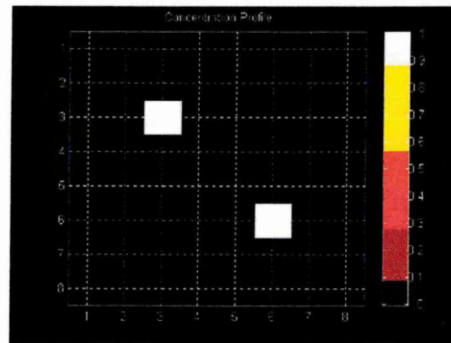


Figure 3.27b Combination of two orthogonal and two rectilinear projections and the hybrid reconstruction algorithm: two pixels flow model

For flow regimes having a void in the centre e.g. an annular flow in which the liquid flows on the wall of the pipe as a film as the gas phase flows in the centre, the hybrid algorithm is unlikely to improve image reconstruction. However, optical sensors are intended for use where the conveyed component ratio is less than 10% vol./vol. In this type of conveying, the material being monitored is well dispersed and experience shows that sensor outputs are often in the noise level (effectively zero).

3.15 General discussion of the results obtained using the LYGBP and hybrid algorithms

All the results shown in sections 3.10, 3.11 and 3.12 demonstrate the typical smearing effect generated by LYGBP. A measure of the accuracy of the image was obtained by

summing all the voltages in the relevant matrix and dividing it by the voltage appropriate to the correct pixels. Thresholding was investigated as possible methods of improving the image.

Simple thresholding models were applied to both the LYGBP results to investigate if they merited further investigation. The thresholds were applied by observing the peak voltage, V_p , in the matrix and then setting elements with $V_{ij} \leq KV_p$ to zero, where $K = 0.5$. Results are shown in tables 3.9, 3.10 and 3.11 and appendix D.

A quantitative evaluation of the LYGBP is obtained by summing the terms in the reconstructed matrix and comparing it with the numerical value provided by the ideal solution. The error percentage is calculated from the expression,

$$\text{Error} = \sum \frac{\text{value of all pixels} - \text{value of ideal pixels}}{\text{value of ideal pixels}} \times 100 \%$$

The resulting errors are tabulated in tables 3.9, 3.10, 3.11 and appendix D in order to compare the accuracy of each projection. The complete set of results for the path length modelling for the single pixel flow model is shown in table 3.9. The following abbreviations and designations are used :-

Th = threshold level

peak = the highest value in the sensitivity matrix

<i>Projections</i>	<i>Algorithm</i>	<i>No. of sensors</i>	<i>Error % (No threshold)</i>	<i>Error % (Th > 0.5 × peak)</i>
2 Orthogonal	LYGBP	16	688	0
2 Orthogonal	Hybrid	16	0	0
2 Rectilinear	LYGBP	22	451.4	106.3
2 Rectilinear	Hybrid	22	0	0
2 Rectilinear/ 2 Orthogonal	LYGBP	38	531.3	0
2 Rectilinear/ 2 Orthogonal	Hybrid	38	0	0
1 Orthogonal/ 2 Rectilinear	LYGBP	24	824.7	0
1 Orthogonal/ 2 Rectilinear	Hybrid	24		
3 fan-beam	LYGBP	36	639.5	233.3
4 fan-beam	LYGBP	48	732.6	0

Table 3.9 Estimated reconstruction errors: path length model

The complete set of results for the optical attenuation modelling for the single pixel flow model is shown in table 3.10.

<i>Projections</i>	<i>Algorithm</i>	<i>No. of sensors</i>	<i>Error % (No threshold)</i>	<i>Error % (Th > 0.5 × peak)</i>
2 Orthogonal	LYGBP	16	4786.7	4521
2 Orthogonal	Hybrid	16	0	0
2 Rectilinear	LYGBP	22	4479.8	4197.3
2 Rectilinear	Hybrid	22	0	0
2 Rectilinear/ 2 Orthogonal	LYGBP	38	4624.5	4332
2 Rectilinear/ 2 Orthogonal	Hybrid	38	0	0
1 Orthogonal/ 2 Rectilinear	LYGBP	24	4408.4	4090.1
1 Orthogonal/ 2 Rectilinear	Hybrid	24	0	0
3 fan-beam	LYGBP	36	2816.2	1463.3
4 fan-beam	LYGBP	48	3178.7	2394.5

Table 3.10 Estimated reconstruction errors: optical attenuation model

The complete set of results for a combination of optical attenuation model and signal conditioning for the single pixel flow model is shown in table 3.11.

<i>Projections</i>	<i>Algorithm</i>	<i>No. of Sensors</i>	<i>Error % (no threshold)</i>	<i>Error % (Th > 0.5 × peak)</i>
2 Orthogonal	LYGBP	16	722.7	722.7
2 Orthogonal	Hybrid	16	0	0
2 Rectilinear	LYGBP	22	464.9	214.9
2 Rectilinear	Hybrid	22	0	0
2 Rectilinear/2 Orthogonal	LYGBP	38	585.4	0
2 Rectilinear/2 Orthogonal	Hybrid	38	0	0
1 Orthogonal/2 Rectilinear	LYGBP	24	1052.7	204.5
1 Orthogonal/2 Rectilinear	Hybrid	24	0	0
3 fan-beam	LYGBP	36	993.7	487.8
4 fan-beam	LYGBP	48	935.2	269.9

Table 3.11 Estimated reconstruction errors: a combination of optical attenuation model and signal conditioning

In general, LYGBP result in significant errors as shown in tables 3.9, 3.10, 3.11 and appendix D. It was expected that increasing the number of projections and, hence, the number of measurements would provide more accurate estimates of the models, but this is not supported by the results. The single pixel and two pixels flow models show larger errors than the half flow and full flow models due to the significant smearing effect of the LYGBP. In some cases thresholding the results for the single pixel and the two pixels flow models reduced the errors significantly. However, the problem with applying thresholding is that it tends to be arbitrary and setting suitable levels is difficult with a dynamic system. Some of the large errors obtained using the LYGBP algorithm arise from the significant smearing effect in the image caused by the back-projection type of reconstruction.

Significant error is introduced if all the sensors do not carry the same weighting in the calculations. The weighting refers to the total path length of light beams intercepting each pixel e.g. two orthogonal projections gives a weighting of $2 \times 10 = 20$ mm per pixel; two orthogonal and two rectilinear projections give a pixel weighting of $(2 \times 10) + (2 \times 14.1) = 48.2$ mm. This non-uniform weighting in sensitivity was very noticeable

with the fan beam systems, where pixels close to the light sources are more heavily weighted than those further away. Optimum reconstructions occur when each pixel has the same path length. For this reason the experimental arrangement is based on a combination of orthogonal and rectilinear projections with the projections carefully arranged so that the weighting is uniform (section 4.4).

Aliasing in the image is observed when using the two orthogonal projections system (figures 3.17b and 3.17f). The previous work carried out by Dugdale [Dugdale, 1994] and Ramli [Ramli, 1998] clearly shows that it is not sufficient to have only two projections as this will result in aliasing of the image, which occurs when two particles intercept the same view, resulting in the ambiguity of the location of some particles. This is due to the fact that the two projections system produces insufficient information, leading to the lack of image resolution and aliasing. As such, it is important to have more than two projections to minimise such problems.

Based on the design study presented in this chapter, an optical tomography system with four projections, which consist of a combination of two orthogonal and two rectilinear projections, was constructed. The conditioned sensor outputs are sampled as digital integers so that the calculations are simplified and high speed is more easily achieved.

Chapter 4

The measurement system

4.1 Introduction

In this chapter, the design of the individual components, which combine to form the optical tomography system, are described.

4.2 The light source

Ideally, it would be preferable to use a laser as the light source because of its degree of coherence, but because of the high cost, it is not used [Durrani & Greated, 1977]. Related previous work [Abdul Rahim, 1996] used a halogen bulb as the light source aligned with arrays of optical fibre transmitter sensors arranged as a two orthogonal projection system. The optical fibre transmitters were arranged on a one-to-one basis with the receivers. Such an arrangement is suitable in an industrial application. In this project an alternative approach is investigated. Four 35mm projectors, which can provide collimated light beams, are used as the light source and light guide. This arrangement is suitable in a laboratory environment. The projectors use 24V d.c., 150W halogen lamps, which removes the 100 Hz ripple from the light source. The angle of divergence of the beams from the projectors was measured and found to be approximately 2.15° , which is much better than that obtained with optical fibre sources. In the case where there is no particle or bubble flowing in the pipe, light from the projector is received by the optical fibre which has an acceptance angle of 56° .

4.3 The receiving system

The receiver optical fibres were designed using equation (3.15). The front lens of the fibre has a radius of 0.8 mm and the exit lens has a radius of 0.63 mm. The exit radius helps ensure all light from the fibre is passed to the PIN diode receiver.

4.3.1 Preparation of the optical fibre

Modifications have to be made to the cut optical fibres before they are assembled into the measurement system in order to ensure that all fibres have smooth surfaces and similar lens radii resulting in near identical characteristics with minimum differences in transmitted intensity and emission angle. To achieve these characteristics, the optical fibres undergo two processes :-

- (a) Polishing.
- (b) Construction of lens.

4.3.1.1 Polishing

Three types of loss are associated with the surface state of the fibre end:-

- (a) the orthogonality of the face with respect to the axis of the fibre;
- (b) convexity;
- (c) roughness.

A good surface is one which is as flat as possible, orthogonal to the axis of the fibre and optically polished. The polishing operation generally uses three different grits; the final finish is provided by the use of a diamond lap. The advantage of this method is that good orthogonality of the face can be obtained and impairments due to convexity and roughness are minimised; the major disadvantage is the number of stages and the duration of each stage in the process [Ungar, 1997].

An aluminium block was constructed to hold the fibres tightly in a vertical manner during the polishing process [Ramli, 1998]. The block is 5.6 cm high, 3.8 cm wide and 10.2 cm long. It has twenty vertical holes each of diameter of 2.3mm allowing ten fibres (or twenty terminations) to be polished simultaneously (figure 4.1). The fibres are inserted into the holes located in the block so that approximately 5 mm of the fibre end protrudes from the bottom of the block. “Blu Tack” is used to trap the fibres between the removable and the fixed aluminium blocks. “Blu Tack” is chosen instead of silicon glue because the latter glued the fibre to the aluminium block and as a result it is difficult to remove the fibre after the completion of the polishing process resulting in damage to the fibre.

The top aluminium block is then tightened to ensure that the fibres are clamped in position tightly. The block containing the fibre is then placed on top of silicon carbide paper mounted on a moving rotor. Initially the fibres are polished with a 300 grit paper, followed by 400, 600 and finally 1200 grit paper. The fibre terminations are assessed after completing each polishing grit to assess their smoothness using a projection microscope. The polishing process is completed when the fibre ends are flat and the rough surfaces are removed. The ends of the fibres are then cleaned with industrial methylated spirit and dried. The fibres can be polished with a diamond paste to obtain the best finish.

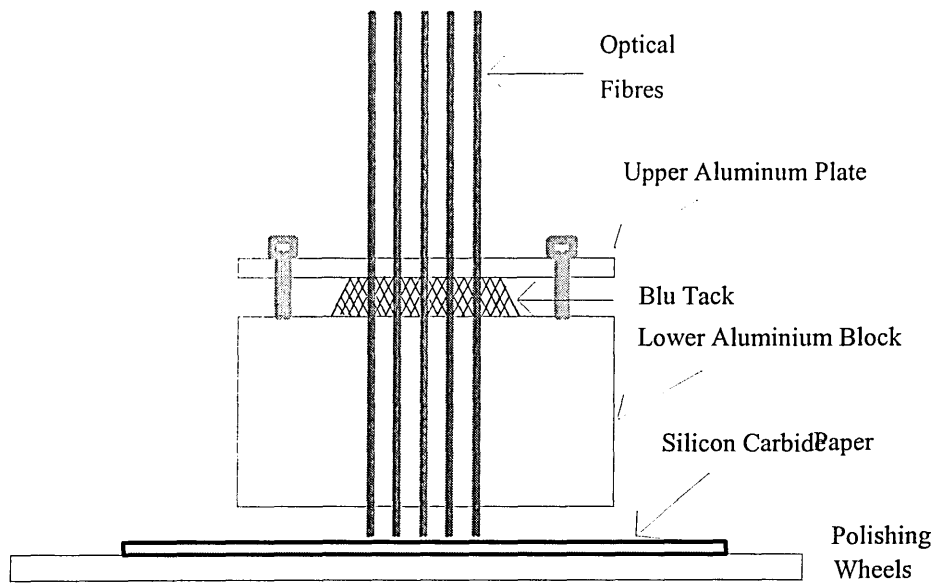


Figure 4.1 Apparatus for polishing optical fibre

4.3.1.2 Construction of lens

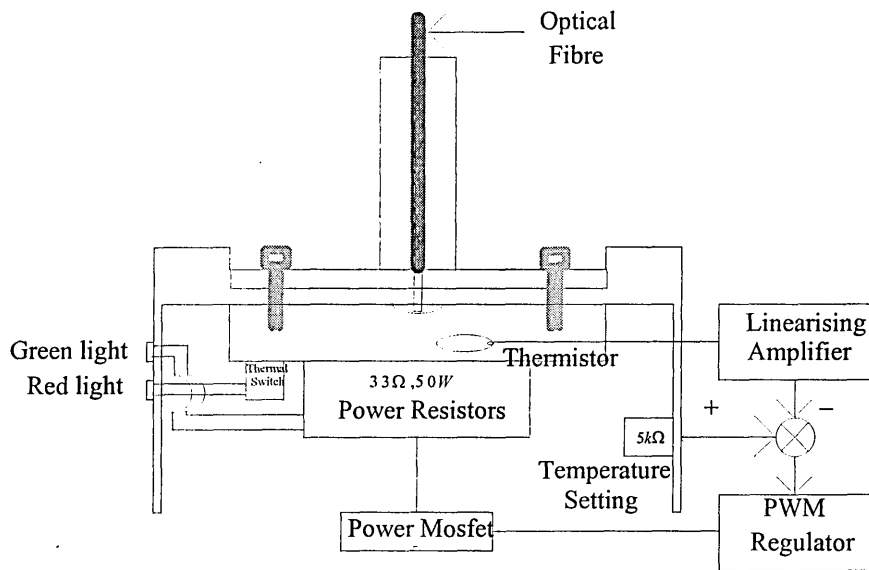


Figure 4.2a Lens making fixture

To maximise the beam intensity into the receiver diode, the beam of light must converge. This is achieved by using an optical lens. Optical lenses available in the market are either large in diameter compared with an optical fibre, or expensive.

Therefore, a temperature platform (figure 4.2a) is used to construct the lens on the optical fibre ends.

The temperature platform provides a means of heating small (20mm diameter) aluminium or other thin plates to allow suitably prepared plastic fibre samples to be formed into an appropriate shape by partial melting. The temperature of the aluminium platform can be controlled over the range 90 - 150 °C; and to operate it requires a 24 V/2A d.c. power supply. The platform is heated by two 33Ω, 50W power resistors which are fed through a power MOSFET. A red LED is illuminated if the temperature of the platform becomes excessive, i.e. greater than 150 °C. Illumination of the green LED indicates that the supply voltage is at a steady value of 24 V.

Before a fibre is placed in the lens making fixture, the polished, flat end of the fibre has 3 mm of the outer sheath stripped from it. The stripped end is positioned in the pre-heated, lens making tool and a controlled pressure applied to the fibre (figure 4.2a). The fixture ensures that the optical axis of the lens is aligned with the optical axis of the fibre. The movement of the fibre is controlled as the plastic melts to ensure close similarity in the shape and size of the resulting lenses. A spherical lens shaped mould in the heating fixture enables the plastic to be melted.

The lens mould was constructed using a steel ball bearing held in a sliding guide which positions the ball coaxially with the position of the optical fibre. The mould is made from a polished aluminium disc having a diameter of 20mm. The disc is clamped to the top surface of the heating block. To form an indentation on the disc, the ball bearing is

pressed into the disc by a controlled amount. This method provides a low cost approach to the production of optical lenses on plastic optical fibres.

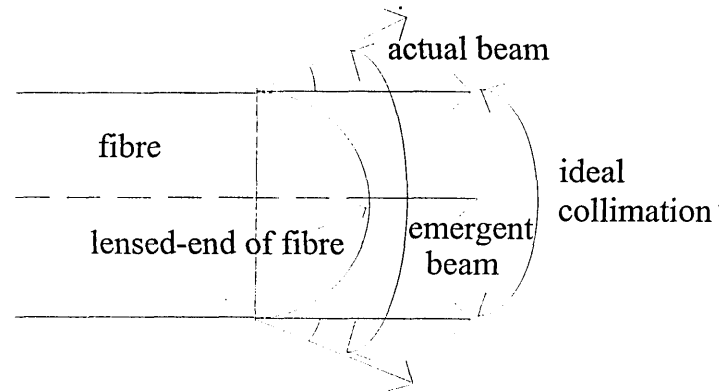


Figure 4.2b Light beam paths coming out of the lens

4.3.1.3 Emission pattern measurement

To ensure that the optical fibres have identical optical characteristics, measurements on the fibres' emission patterns were performed.

Each lensed optical fibre was tested by illuminating them with light coming from a halogen bulb placed 20 cm away. The fibre was connected to a photovoltaic detector and an amplifying stage. The results show that there is only slight variations between the output voltage given by each fibre. The mean of the results is 7.19 V and the standard deviation is 0.1 V. This shows that the fibres have closely matched characteristics.

It is also important to measure the alignment of the axis of the optical fibre and the lens as well as the angular divergence of the beam from the fibre. The latter measurement is important to ensure that the optical power in the centre of the beam is maximised. The

test rig in figure 4.3 was used for this purpose. It is equipped with two protractors placed horizontally and vertically respectively in order to measure the angle through which the fibre is rotated. The fibre is inserted into a hole in the fixture so it can be rotated about its optical axis relative to a fixed photodiode measurement head, and simultaneously can be rotated horizontally relative to the sensor. It is linked to an optoelectronic circuit which converts the optical signal to an electrical signal and then amplifies it.

A vertical emission test was carried out on each lensed optical fibre. The fibre was placed 20 cm from a halogen light source powered by a power supply delivering 5 V. The fibre was aligned with the photodetector incorporated into a current-to-voltage converter and subsequently amplified. The optical intensity was measured as the fibre was rotated axially through 360°. The results for three fibres are depicted in figure 4.4. The results show that the intensities of the optical fibres are reasonably independent of the fibre orientation. This indicates that the fibre termination is normal to the optical fibre axis.

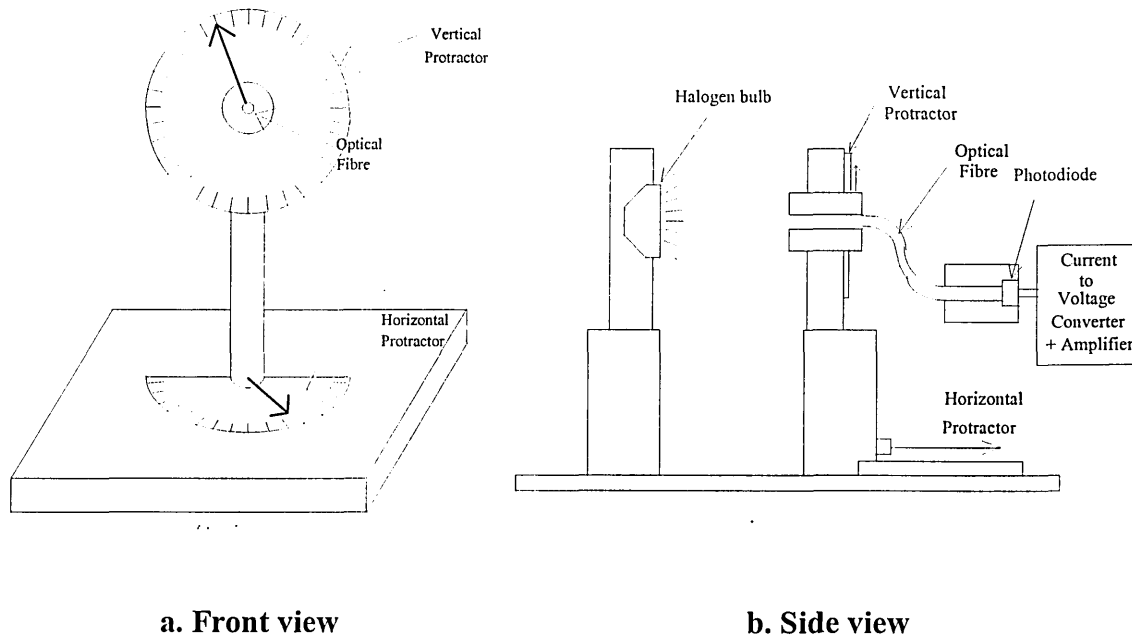


Figure 4.3 Test rig for optical fibre

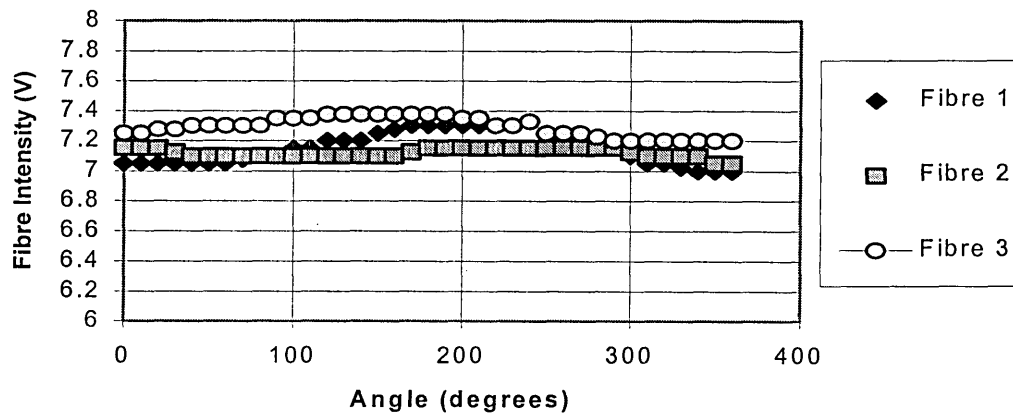


Figure 4.4 Vertical emission pattern of optical fibres

A similar test was conducted on the lensed fibre for the horizontal emission pattern. The fibre was positioned 20 cm from a halogen bulb. The bulb was connected to a d.c. power supply delivering 5V. The fibre was rotated through 180° horizontally, 90° either side of the axis between the fibre and the receiver, and for each angle, the intensity was recorded. The same set up used for the vertical emission test was used for this purpose. The results for three of the fibres are shown in figure 4.5. The intensities of all the fibres are nearly identical to each other.

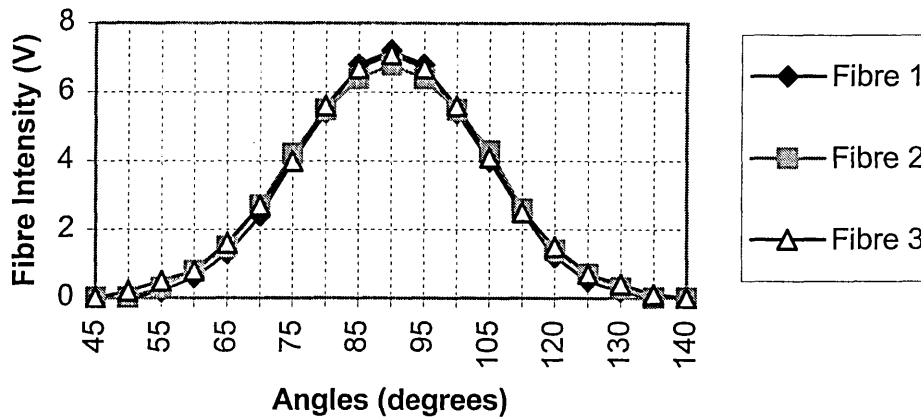


Fig. 4.5 Horizontal emission pattern of optical fibres

The method described in this section is a low cost approach to the production of optical lenses on plastic optical fibres. This method enables the lens power to be controlled and ensures that the optical fibres and the lens share a common axis. The lens is acceptably concentric and it helps to collimate the light beam. A fully collimated beam cannot be achieved due to chromatic and lens aberrations.

4.3.2 The receiver circuit

The receiver circuit is designed for signal conditioning using amplifiers and filters. The input of the sensor is a physical signal represented by light, while the outputs of the sensor are electrical signals consisting of a rectified voltage and an averaged voltage (figure 4.6). The rectified output enables unipolar data acquisition and consequent signal processing. The long time constant provides some averaging. The output of the amplifier should be proportional to the gas flow rate passing the associated sensor. If all the amplifier outputs are summed, they should be proportional to the gas flow rate indicated by the gas rotameter. The circuit is placed in an earthed metal box to minimise electrical noise pick-up. The analogue signals from an array of optical transducers, covering a cross-section of the pipe, are converted into digital form and passed into an image reconstruction system. Data acquired in this way enable an image of the cross-section of the flow regime to be created [Nordin, 1995].

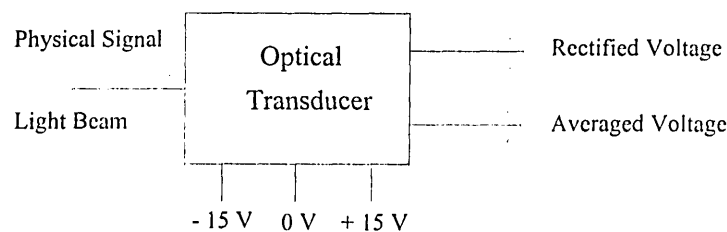


Figure 4.6 Optical Transducer

Light traversing the flow pipe passes through an optical fibre and reaches the current-to-voltage converter (figure 4.7), which then converts it to current by the PIN photodiode. The BPX65 photodiode used in this experiment is a planar 1mm^2 silicon PIN photodiode, which is hermetically sealed with an integral plain glass window. It has a low junction capacitance, short switching time and, because of its high frequency response, is capable of detecting wide bandwidth signals. It has a peak spectral response of 850 nm and, at that wavelength its responsivity is 0.55 A/W . The rise time of the photo current is 3.5 ns.

If the flow containing droplets traverses the light beam, the portion of the light reaching the photodiode may be reduced due to scattering and reflection. For small droplets, the projected area is proportional to the amount of signal lost. Hence, the signal lost is detected as a voltage, which is proportional to the particle area detected [Chin et al, 1988].

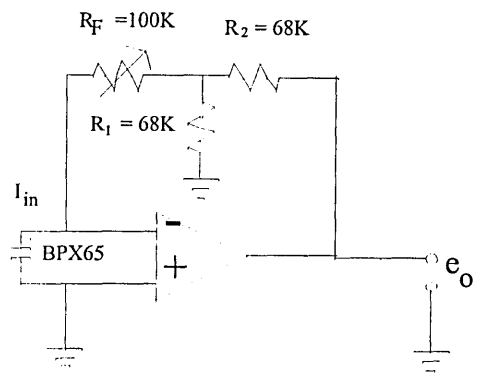


Figure 4.7 Current-to-voltage converter

Dual Bi-FET TL072CN operational amplifiers costing £0.28 each are used for the receiver circuit. Among the electrical characteristics of the TL072CN are :-

Noise voltage = $18\text{nV}\sqrt{\text{Hz}}$ Typ

Input bias current = 30 pA Typ (at 25 °C)

Input offset current = 5 pA Type (at 25 °C)

Input offset voltage = 3 mV Typ (at 25 °C)

The circuit (figure 4.7) produces an output voltage which is proportional to the input current as expressed mathematically by,

$$e_0 = -I_{in}R_f \left(1 + \frac{R_2}{R_1}\right)$$

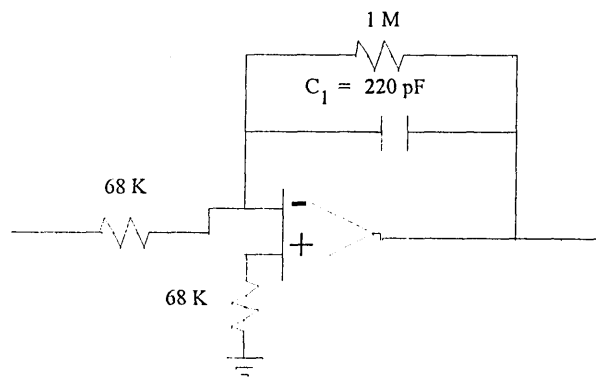


Figure 4.8 Buffer

The second operational amplifier stage (figure 4.8) acts as buffer and provides a dc gain of -14.7. The system is to be used for water/gas or water-conveyed slurries so a signal bandwidth of 800 Hz is chosen for the system, as a compromise between the required signal bandwidth related to the flow, approximately 200 Hz for 2 mm diameter bubbles travelling at 0.5 m/s [Green & Cunliffe, 1983] and limiting the noise inherent in any measurement system. Hence,

$$\omega = 2\pi (800) = 5.03 \times 10^3 \text{ rad/s}$$

$$\text{Time constant, } \tau = \frac{1}{\omega} \approx 2 \times 10^{-4} \text{ s}$$

$$\tau = CR \text{ and } R = 1 \text{ M}\Omega$$

Hence, $C = 200 \text{ pF}$ (220 pF was used in this project)

The output of the second stage is connected to the following stage via an a.c. coupling network (figure 4.9) effectively producing a band pass filter. The time constant of this a.c. coupling network is $\tau = CR = 1$ second. As such the corner frequency is $f_c = \frac{1}{2\pi\tau} = 0.159 \text{ Hz}$. A polycarbonate capacitor is used as the coupling capacitor because of its low loss, high stability, and close tolerances. It also exhibits better characteristics than a polyester capacitor, particularly the insulation resistance and temperature coefficient [Farnell Catalogue, 1999]. It also provides excellent accuracy, temperature stability and high accuracy [Horowitz & Hill, 1993].

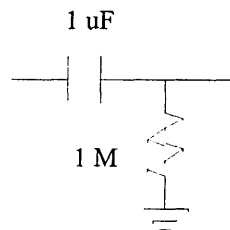


Figure 4.9 AC coupling network

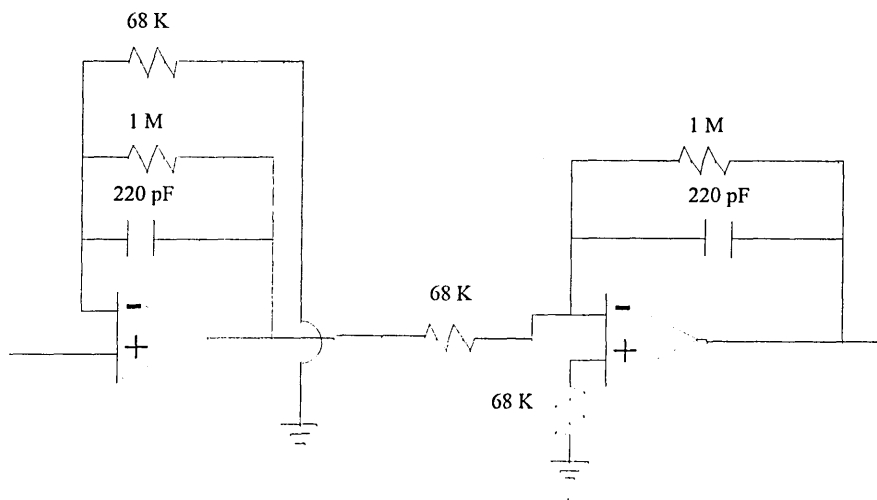


Figure 4.10 The third and fourth stage

The third stage (figure 4.10) has a gain = $1 + \frac{1M}{68K} = 15.7$ whereas the fourth stage (figure 4.10) provides a gain of 14.7. The corner frequencies of the third and fourth stages are both 723.4 Hz.

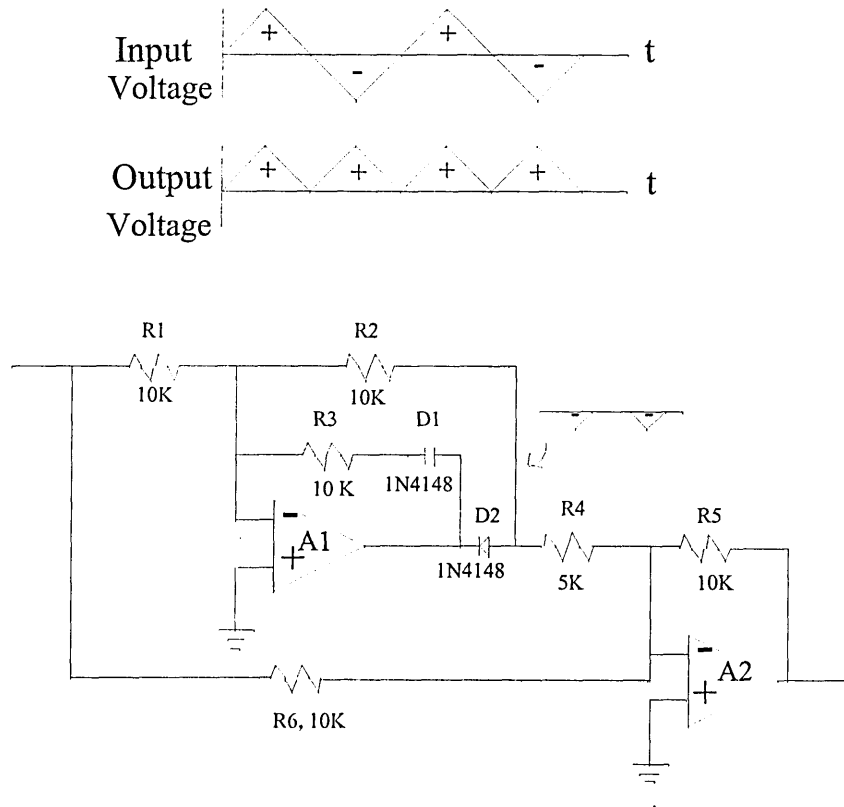


Figure 4.11 Precision Full Wave Rectifier

The next stage of the circuit consists of a precision full wave rectifier (figure 4.11). The output voltage of the rectifier is given by the following expression:

$$\text{Output, } e_0 = +|e_1| \frac{R_5}{R_6}, \text{ for } R_1 = R_2 = R_6 = 2R_4$$

$$e_0 = +|e_1|$$

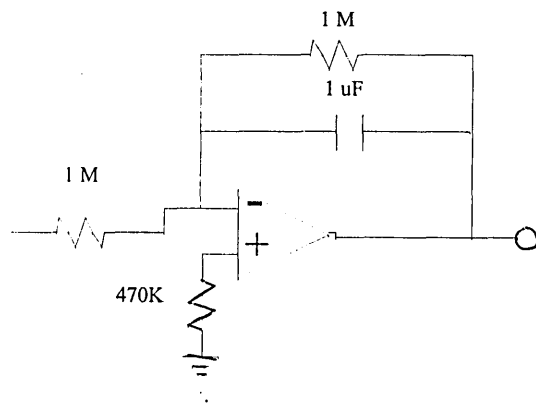


Figure 4.12 Low pass filter

The output from the rectifier circuit is directly coupled to the low pass filter circuit (figure 4.12) which has an upper cut off frequency of $f_c = \frac{1}{2\pi\tau} = 0.159 \text{ Hz}$. This circuit provides averaging or smoothing for the preceding stage. The gain of this low pass filter circuit is set to 1.

The overall receiver circuit diagram is shown in Figure 4.14.

4.3.3 Calibration and tests on the receiver circuit

Three tests were carried out on the receiver system. A gain check was made by injecting a low amplitude sine wave (5 mV peak-to-peak, frequency of 100Hz) into the summing junction of the buffer amplifier (Figure 4.14) via a 10 kΩ resistor. The outputs of each of the following stages were checked with an oscilloscope for amplitude and distortion. The stage gains were calculated and in agreement with predicted values (section 4.3.2).

The frequency of the sine wave was varied from 0.5 Hz to 3 kHz with a constant input voltage of 5 mV peak-to-peak. The results of this frequency response are plotted in

figure 4.13. Note, only the amplitude response is shown, because the final stage of the system produces rectification.

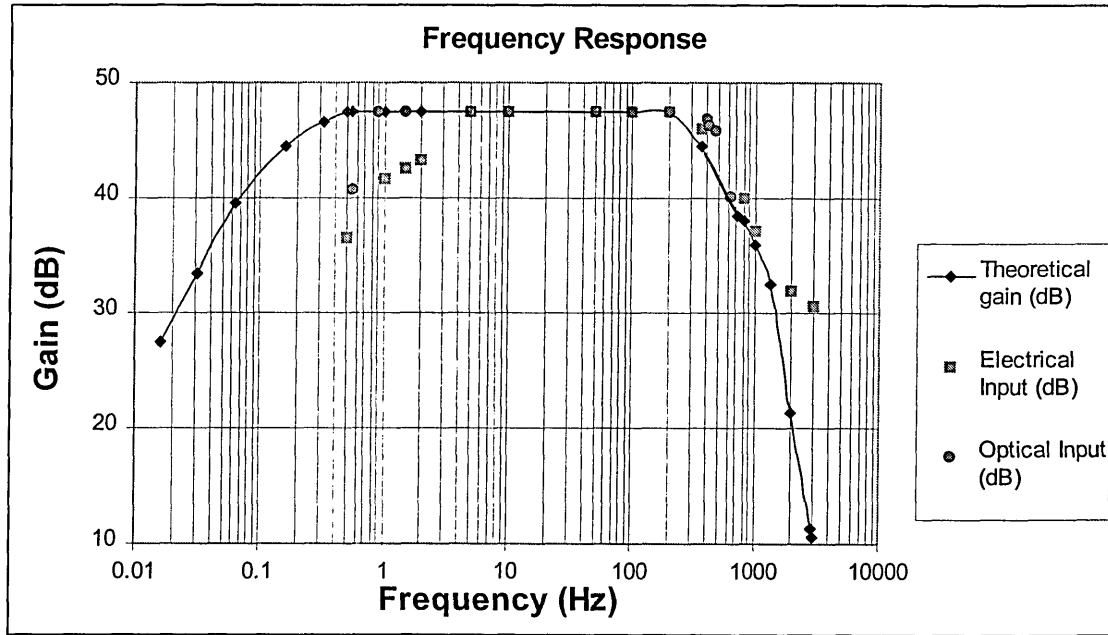


Figure 4.13 Frequency response of the circuit

In order to obtain an overall calibration of the receiver circuit (figure 4.14), a special arrangement was set up in which an optical fibre, linked to each receiver circuit in turn, was illuminated by light coming from a dichroic halogen bulb. A rotating disc containing a series of slits is placed between the bulb and the optical fibre. When the source of light, a slit and the fibre are aligned, a pulse of light energy flows from the light source into the optical fibre. The output of the circuit, as observed on an oscilloscope, displays flat-topped pulses. In order to ensure that each circuit produces similar outputs, the potentiometer, R_f (figure 4.14), of each circuit is adjusted, varying the gain.

Changes in overall gain system gain due to uneven illumination of optical fibres in the practical measurement set up and drift in working point of the electronics due to effects such as temperature change, were compensated for in software (section 5.2).

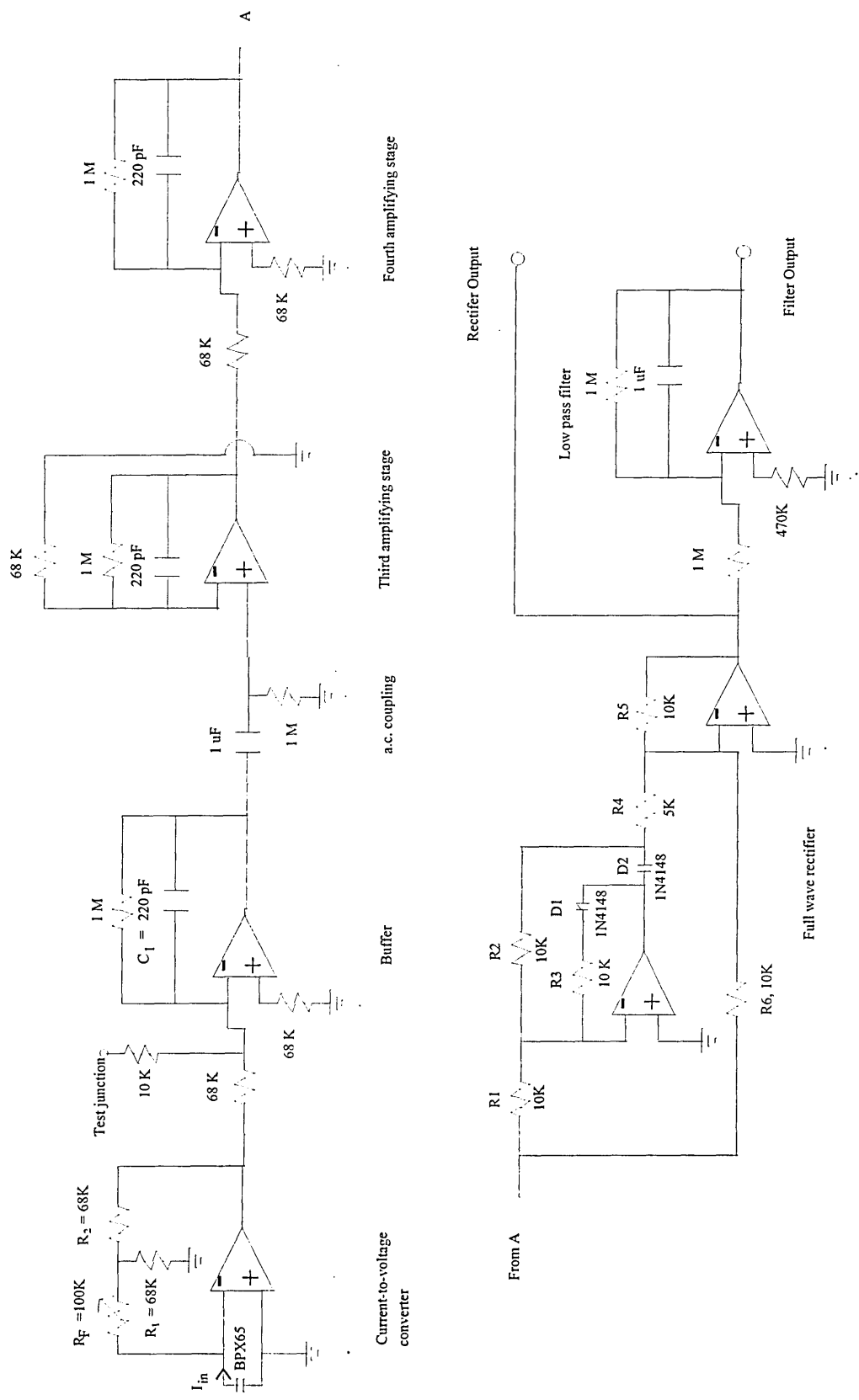


Figure 4.14 The receiver circuit

4.4 Design of the overall optical tomography system

The light receiver consists of an array of optical fibre sensors arranged in a combination of two orthogonal and two rectilinear projections (figure 4.15b). The orthogonal projections (figure 4.15a) consist of an 8×8 array of optical fibre sensors whereas the rectilinear projections consist of an 11×11 array of optical fibre sensors (the number of sensors are chosen so that they will give a balanced sensitivity). Thus the total number of optical fibre sensors used is thirty eight for each plane and for cross-correlation purposes, the total number of optical fibre sensors is doubled to seventy six as there are two planes placed axially along the flow pipe. The optical fibres are positioned adjacent to each other to provide a large number of views. Ideally the two orthogonal and two rectilinear projections system should be in the same plane. However, if they were they would overlap each other and so two of the projections have to be placed in a separate plane. These planes are separated by only a few mm with the two orthogonal projections system placed on top of the rectilinear projections. Each optical fibre receiver has a length of 200 cm from the flow pipe to the electronic circuit.

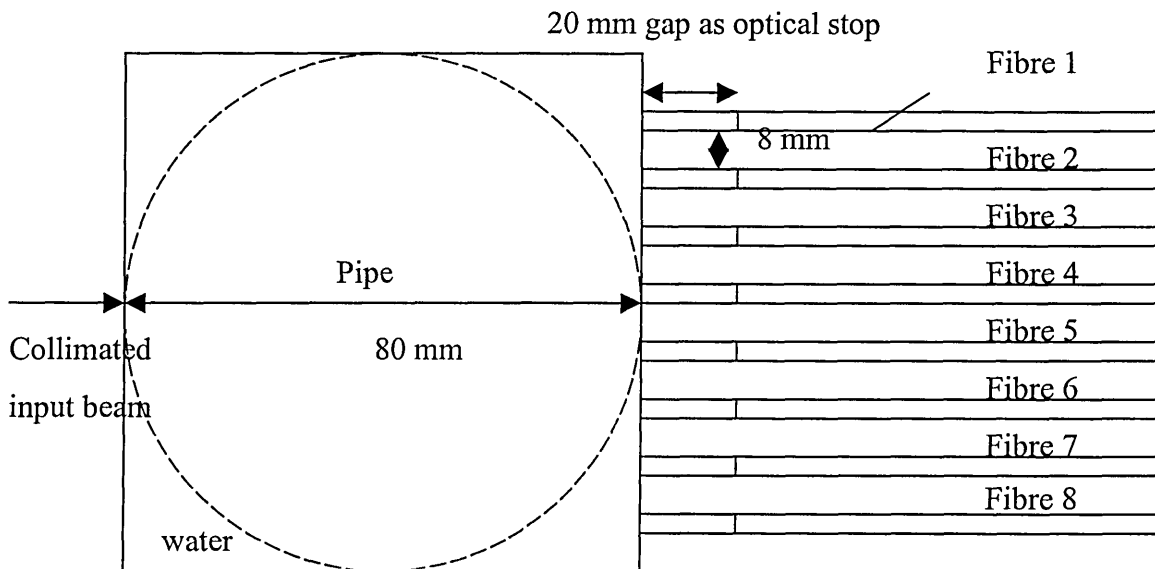


Figure 4.15a Arrangement of the optical fibres around the flow pipe - top view

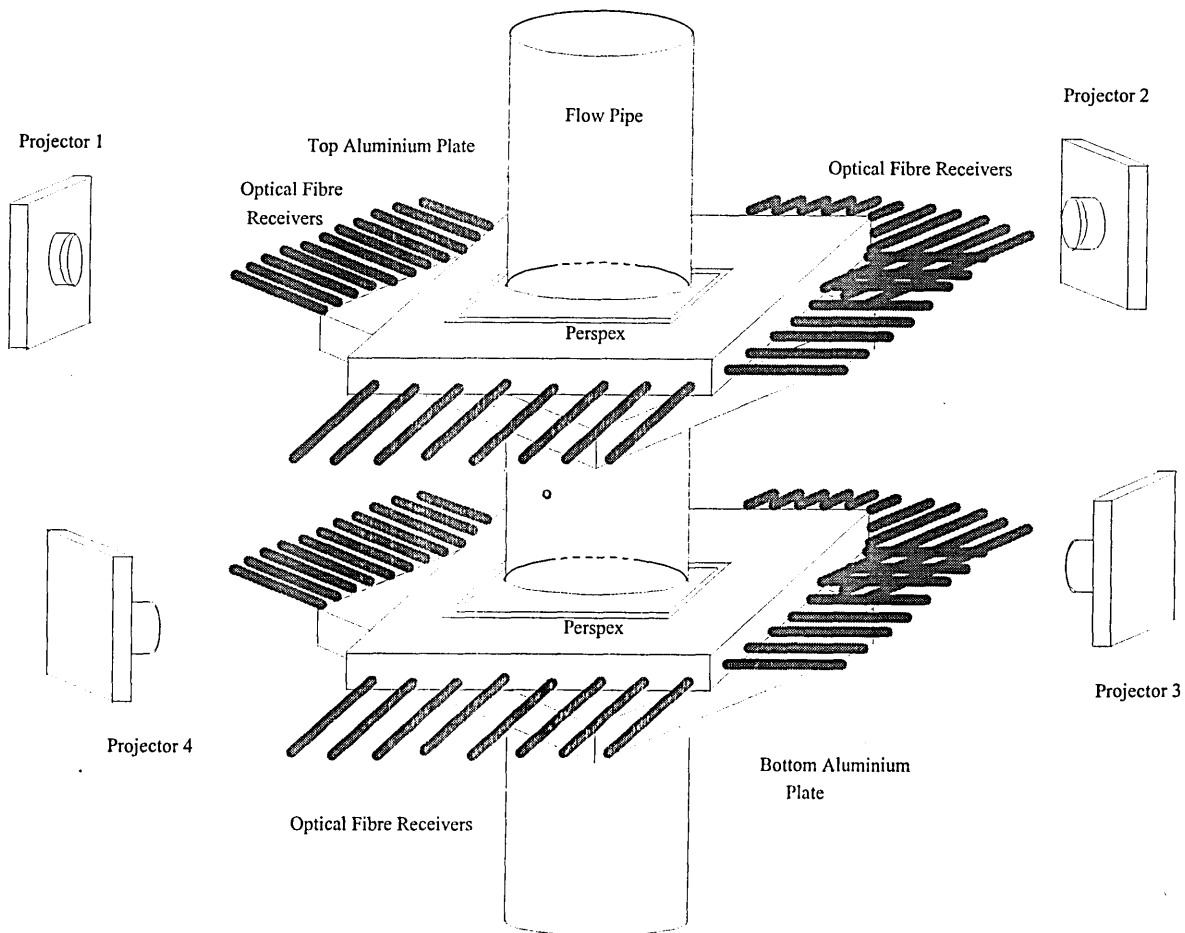


Figure 4.15b Arrangement of the optical fibres around the flow pipe - isometric view

4.5 The data acquisition system

The Keithley Instruments DAS-1800HC data acquisition system was used in this project. It is a high-performance data acquisition board, which is suitable for an IBM-compatible PC. It can be configured for 64 single-ended or 32 differential inputs and can measure up to 333ksample/s maximum input rate.

For concentration measurements (chapter 5) the band pass amplifier of the transducer has a cut off frequency of approximately 800 Hz. So a sampling frequency of 500 Hz per channel was chosen as the velocities and flow rates associated with this project are relatively low (i.e. 0.2 - 0.3 m/s). This enables two hundred and twenty two points to be collected for each of the thirty eight channels, which allows 0.44 seconds of flow data to be obtained. For velocity measurements (chapter 6), the sampling frequency must be fast enough (100 Hz in the case of large bubbles) to record the transit time of the bubbles between upstream and downstream sensors).

4.6 The hydraulic flow rig

The system was tested on a hydraulic flow rig shown in figure 4.15. The measurement system is built around a vertical pipe, 1.27m long, with a circular cross-section, 80mm in diameter. Control of the water flow is effected by the use of a pump and by various valves installed in the rig. Bubbles are injected into the measurement section through two bubble injectors placed at the base of the vertical section. The two small air injectors are utilised to blow different sized gas bubbles from the bottom of the pipe. Control of bubble flow is achieved through the use of two valves linked to the two bubble injectors. The valves can control the size of the bubbles as well as generating various flow regimes. The air pressure supply to the bubble injectors can be varied from 0 to 420 kPa. Throughout the experiment, a constant pressure of 50 kPa was applied.

The flow pipe is made of perspex to enable visual observation of the flow. The lower measurement section, consisting of thirty eight sensors, is placed 62 cm above the gas injection points and the second sensing array, which also consists of thirty eight sensors, is placed 15 cm (approximately two pipe diameter) downstream of the former. The measurement section is of modular construction and comprises a series of perspex blocks 90 mm square with an 80 mm diameter central bore so that when bolted together they provide a continuous 80 mm diameter internal flow passage. The square shape of the section allows optical observation and measurement to be made without optical distortion - as would be the case if a circular pipe was used [King et al, 1983]. The flow rig is equipped with two rotameters: a water rotameter (0 - 7 l/min) and a gas rotameter (0 - 7 l/min). Each rotameter provides direct readings of the total flow rate of water and bubbles respectively. For the experiments described in this thesis water always formed the continuous phase and the gas flow was always in the bubbly regime. The volumetric flowrate of bubbles ranged from 0 to 7 l/min.

In the measurement section (sections 5.2 and 5.3) and associated discussions (section 5.4) small bubble and large bubble flows are mentioned. For the purposes of this thesis small bubbles are generated by a porous plug in the base of the flow rig, producing bubbles which visually appear to be in the range 1 - 10 mm. Large bubbles are produced by direct gas injection into the flowing water. These bubbles are about 15 - 20 mm in diameter.

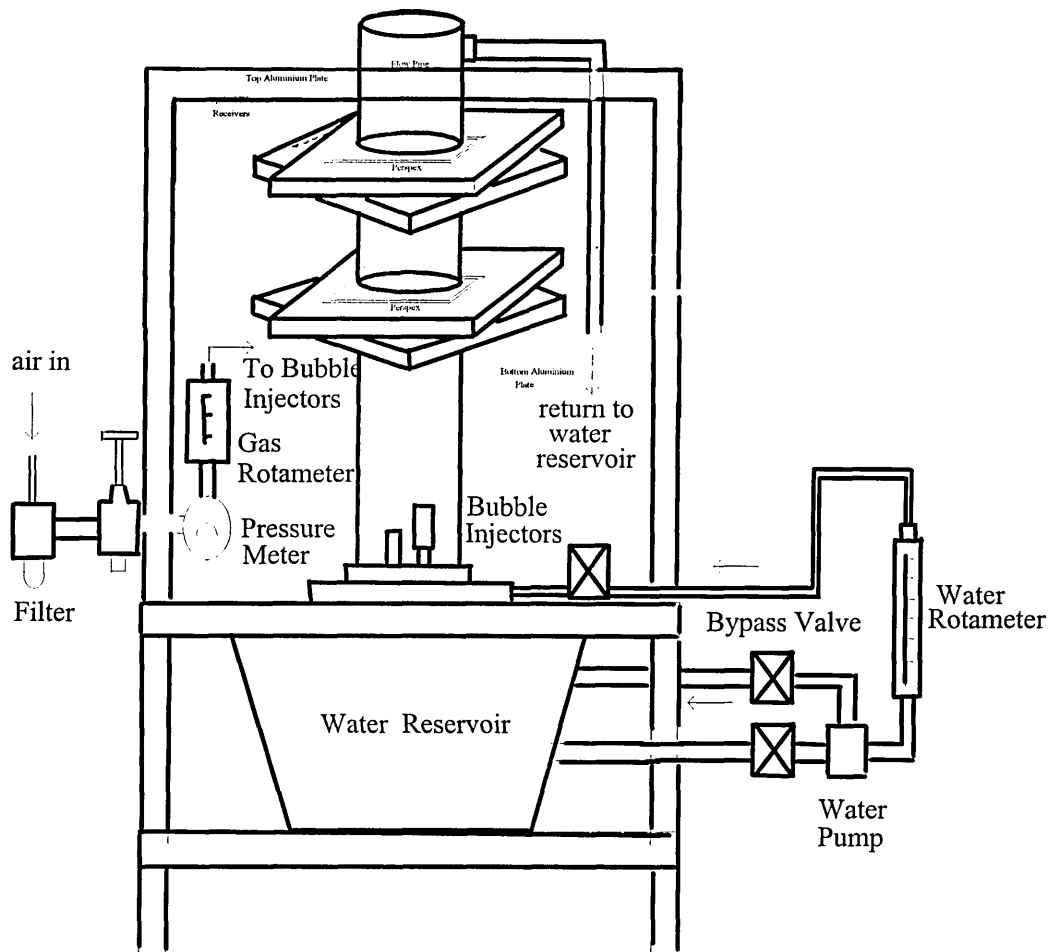


Figure 4.15 The hydraulic flow rig

Chapter 5

Concentration measurement

5.1 Introduction

The aim of this section is to investigate the use of the optical tomographic system for obtaining concentration information of the bubbles in the flow pipe. Two approaches are investigated. The first aims to obtain an average gas concentration at the measurement section, the second aims to obtain a gas distribution profile by using tomographic imaging. The hybrid reconstruction (section 3.13) algorithm is used to generate the tomographic images of the measurement cross-section using the measured data.

5.2 Average concentration measurement

The measurements presented in this section consider the results from each sensor as a continuous sample of the gas concentration within its sensing field. The method was to obtain two hundred and twenty two samples for all thirty eight sensors; each sensor was sampled at 500 Hz. The mean value for each sensor was calculated at the specified flow rate. The standard layergram back-projection algorithm was applied and the resulting pixel voltages summed. The values obtained for each flow rate for small bubbles are compared with the values obtained for large bubbles to observe the effect of flow rates and bubble size. Table 5.1 shows the sum of pixels for small bubbles and large bubbles corresponding to various volumetric flow rates.

Flow Rates (l/min)	Sum of pixels for small bubbles (V)	Sum of pixels for large bubbles (V)
0	4.9	4.9
0.5	262.2	291.1
1	345.6	334.2
1.5	285.4	365.5
2	240.5	397.9
2.5	249.3	389.3
3	243.8	412
3.5	201.6	408.4
4	188	406.4
4.5	185.5	390.8
5	180.1	371.4
5.5	186.4	340.3
6	185.4	316.1
6.5	179.3	303.9
7	188.2	282.4

Table 5.1

The results in table 5.1 are shown graphically in figure 5.1 and discussed in section 5.4.

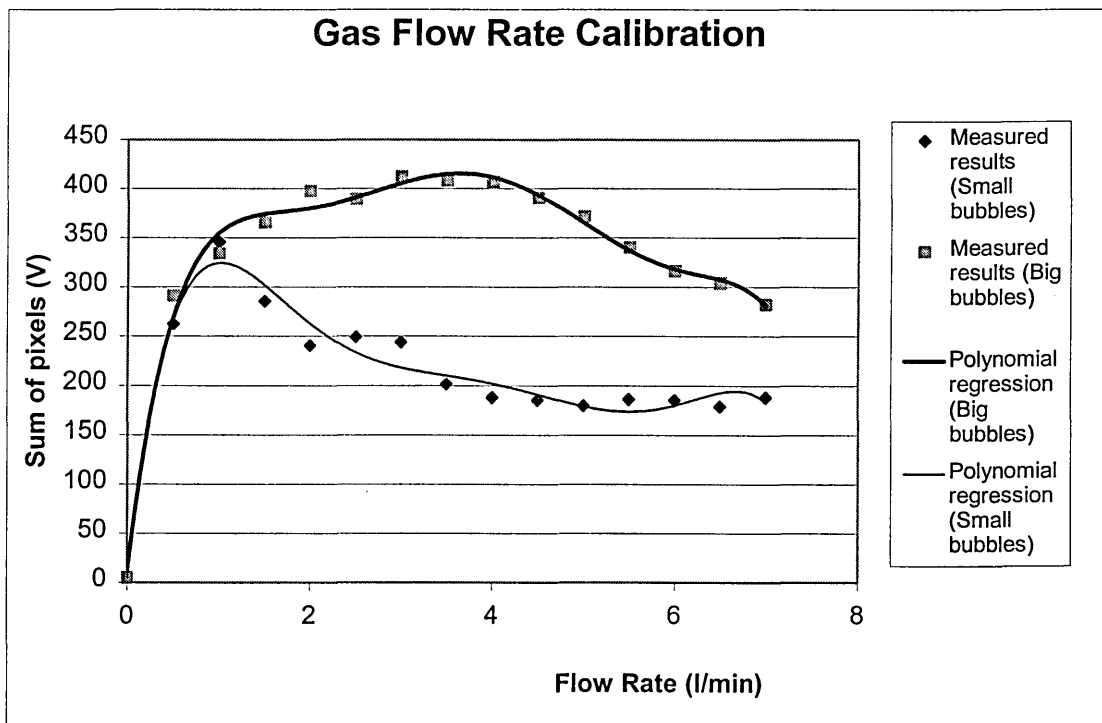


Figure 5.1 Gas flow rate calibration graph - water flow rate 3 l/min

5.3 Concentration profiles

The measurement system for concentration consists of thirty eight sensors. Ideally, with zero flow, all sensors should have zero output. In practice many of the sensors have an output voltage due to factors such as drift, intrinsic noise and offset in operational amplifiers. To reduce these errors all the sensors were sampled at 500 Hz for 0.44 seconds with no gas flow at the start of each series of experiments. The root mean square voltage was then calculated for each sensor to provide a zero flow voltage. The zero flow voltages were used to correct the gas flow measurements for offset errors in each sensor.

The experiments were conducted with the laboratory lights switched off to ensure that the mains lighting did not affect the light receivers. Measurements were made by energising all thirty eight optical sensors and monitoring their outputs at several gas flow rates ranging from 0 l/min to 7 l/min. Throughout the experiment, water flowed upwards at a volumetric flow rate of 3 l/min. The data acquisition system was used to obtain two hundred and twenty two samples, with a sampling frequency of 500 Hz per channel, at each flow rate. These data were used to calculate two hundred and twenty two concentration tomograms.

After implementing the hybrid reconstruction algorithm (section 3.13), optical density measurements are expressed as voltages with respect to a two-dimensional co-ordinate frame defining a plane through the sensor array. Each point in this co-ordinate system corresponds to a real-world location lying on a plane through the pipe. Hence, bubble concentration estimates are registered with the pipe locations from which they arose.

The time series for one of the sensors, which interrogated the central cross-section of the pipe, is shown in figure 5.2. The sampling frequency used is 500 Hz. The bubbles

injected from the base of the pipe consist of small bubbles generated at a volumetric flow rate of 0.5 litres/min.

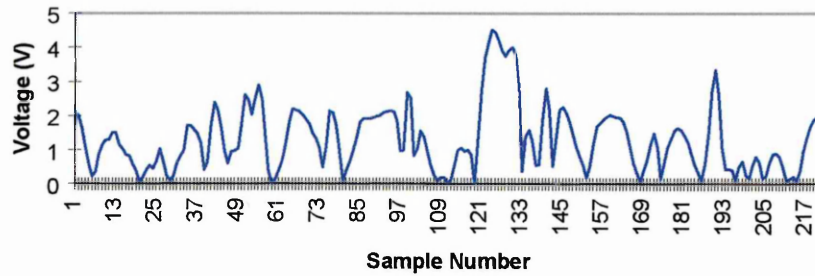


Figure 5.2 Typical sensor output over time

The peaks in Figure 5.2 represent the dispersed phase (bubbles) which cut the light path coming from the light projectors.

5.3.1 Concentration profiles of small bubbles

The following subsections show a sequence of selected images representing the reconstructed fields of small bubbles flowing in water, which were generated at various volumetric flow rates. These results are discussed in section 5.4.

5.3.1.1 Flow rate of 0.5 l/min

A sequence of images representing small bubbles flowing at a volumetric flow rate of 0.5 l/min, are shown on figures 5.3a to 5.3d.

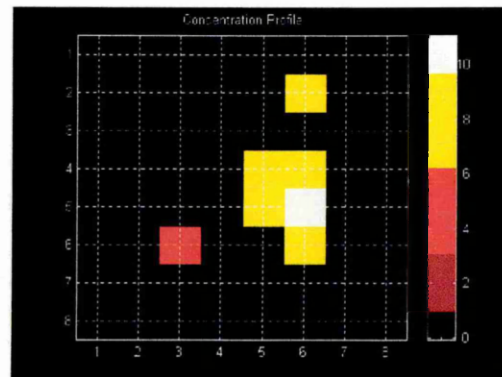
$$\begin{bmatrix} 0 & 0 & 0 & 0 & 0 & 0 & 0 & 0 \\ 0 & 0 & 0 & 0 & 0 & 9.06 & 0 & 0 \\ 0 & 0 & 0 & 0 & 0 & 0 & 0 & 0 \\ 0 & 0 & 0 & 0 & 8.59 & 9.54 & 0 & 0 \\ 0 & 0 & 0 & 0 & 8.82 & 11.00 & 0 & 0 \\ 0 & 0 & 4.93 & 0 & 0 & 8.40 & 0 & 0 \\ 0 & 0 & 0 & 0 & 0 & 0 & 0 & 0 \\ 0 & 0 & 0 & 0 & 0 & 0 & 0 & 0 \end{bmatrix}$$


Figure 5.3a Matrix and concentration profile of the first sample representing small bubbles at 0.5 l/min

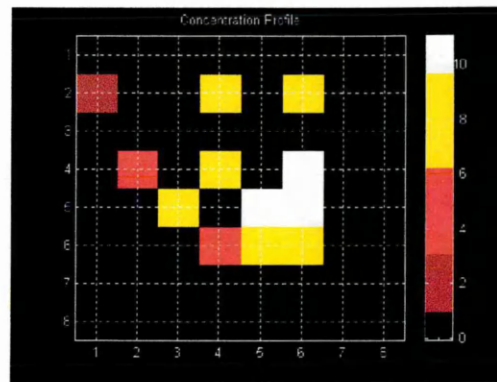
$$\begin{bmatrix} 0 & 0 & 0 & 0 & 0 & 0 & 0 & 0 \\ 1.97 & 0 & 0 & 7.44 & 0 & 9.32 & 0 & 0 \\ 0 & 0 & 0 & 0 & 0 & 0 & 0 & 0 \\ 0 & 3.47 & 0 & 9.64 & 0 & 10.75 & 0 & 0 \\ 0 & 0 & 9.48 & 0 & 9.75 & 11.00 & 0 & 0 \\ 0 & 0 & 0 & 5.95 & 9.00 & 8.59 & 0 & 0 \\ 0 & 0 & 0 & 0 & 0 & 0 & 0 & 0 \\ 0 & 0 & 0 & 0 & 0 & 0 & 0 & 0 \end{bmatrix}$$


Figure 5.3b Matrix and concentration profile of the second sample representing small bubbles at 0.5 l/min

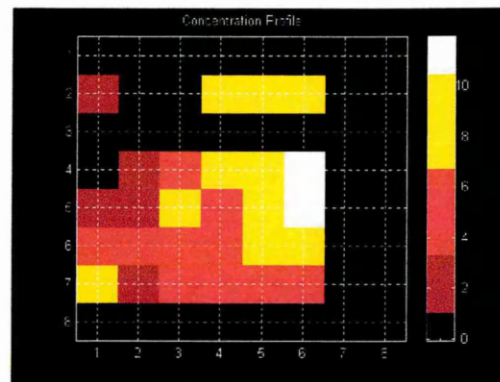
$$\begin{bmatrix} 0 & 0 & 0 & 0 & 0 & 0 & 0 & 0 \\ 1.87 & 0 & 0 & 7.72 & 8.89 & 9.05 & 0 & 0 \\ 0 & 0 & 0 & 0 & 0 & 0 & 0 & 0 \\ 0 & 3.18 & 5.96 & 10.22 & 10.41 & 11.87 & 0 & 0 \\ 2.65 & 3.03 & 8.34 & 4.65 & 9.54 & 10.78 & 0 & 0 \\ 4.68 & 6.65 & 6.19 & 6.48 & 9.38 & 8.63 & 0 & 0 \\ 7.05 & 2.45 & 5.39 & 5.88 & 6.06 & 4.73 & 0 & 0 \\ 0 & 0 & 0 & 0 & 0 & 0 & 0 & 0 \end{bmatrix}$$


Figure 5.3c Matrix and concentration profile of the third sample representing small bubbles at 0.5 l/min

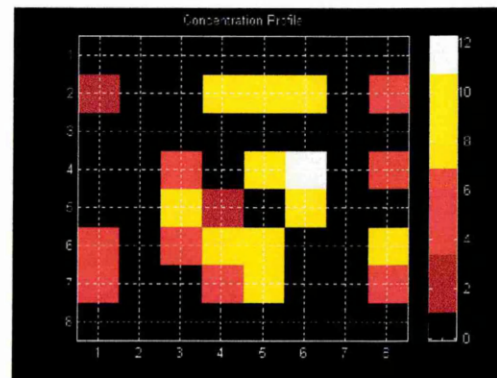
$$\begin{bmatrix} 0 & 0 & 0 & 0 & 0 & 0 & 0 & 0 \\ 1.75 & 0 & 0 & 6.95 & 8.72 & 8.64 & 0 & 4.96 \\ 0 & 0 & 0 & 0 & 0 & 0 & 0 & 0 \\ 0 & 0 & 6.26 & 0 & 10.23 & 12.18 & 0 & 5.16 \\ 0 & 0 & 8.19 & 3.37 & 0 & 10.19 & 0 & 0 \\ 5.10 & 0 & 6.17 & 7.15 & 9.26 & 0 & 0 & 8.97 \\ 6.81 & 0 & 0 & 5.50 & 6.86 & 0 & 0 & 5.92 \\ 0 & 0 & 0 & 0 & 0 & 0 & 0 & 0 \end{bmatrix}$$


Figure 5.3d Matrix and concentration profile of the fourth sample representing small bubbles at 0.5 l/min

For the remainder of the concentration profile results for small bubbles only the pictorial image are presented.

5.3.1.2 Flow rate of 3 l/min

A sequence of images representing small bubbles flowing at a volumetric flow rate of 3 l/min, are shown on figures 5.4a to 5.4d.

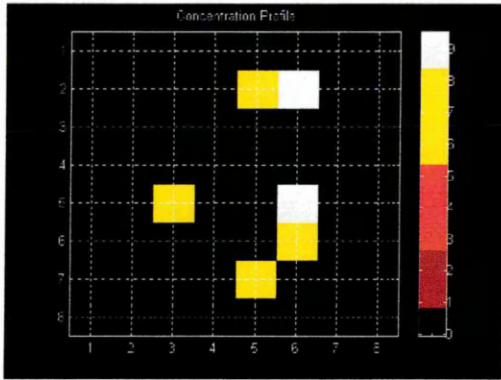


Figure 5.4a Concentration profile of the first sample representing small bubbles at 3 l/min

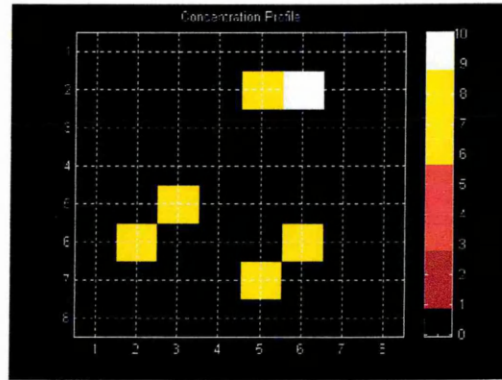


Figure 5.4b Concentration profile of the second sample representing small bubbles at 3 l/min

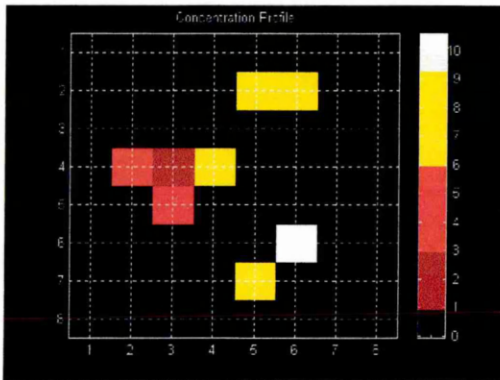


Figure 5.4c Concentration profile of the third sample representing small bubbles at 3 l/min

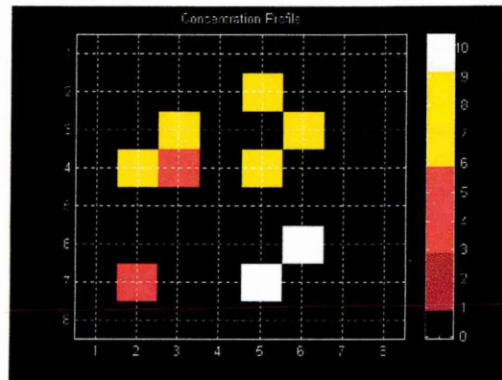


Figure 5.4d Concentration profile of the fourth sample representing small bubbles at 3 l/min

5.3.1.3 Flow rate of 5 l/min

A sequence of images representing small bubbles flowing at a volumetric flow rate of 5 l/min, are shown on figures 5.5a to 5.5d.

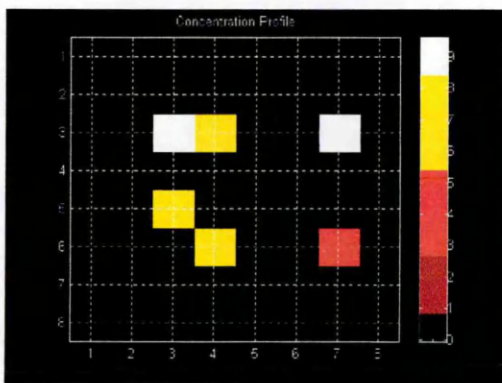


Figure 5.5a Concentration profile of the first sample representing small bubbles at 5 l/min

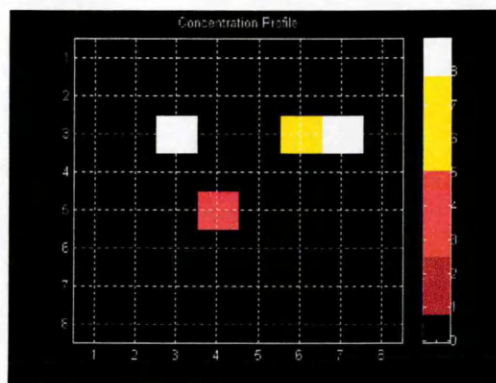


Figure 5.5b Concentration profile of the second sample representing small bubbles at 5 l/min

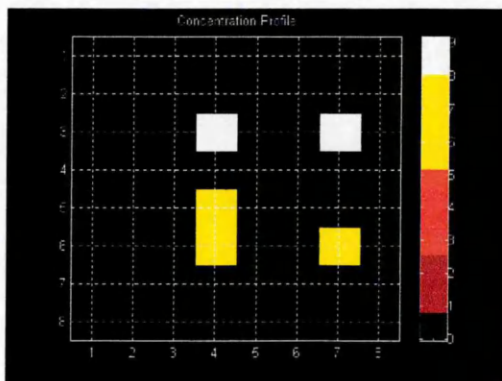


Figure 5.5c Concentration profile of the third sample representing small bubbles at 5 l/min

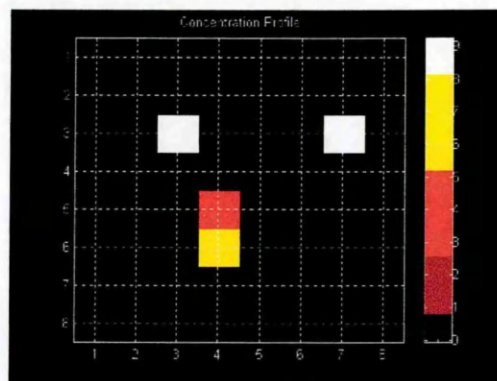


Figure 5.5d Concentration profile of the fourth sample representing small bubbles at 5 l/min

5.3.1.4 Flow rate of 7 l/min

A sequence of images representing small bubbles flowing at a volumetric flow rate of 7 l/min, are shown on figures 5.6a to 5.6d.

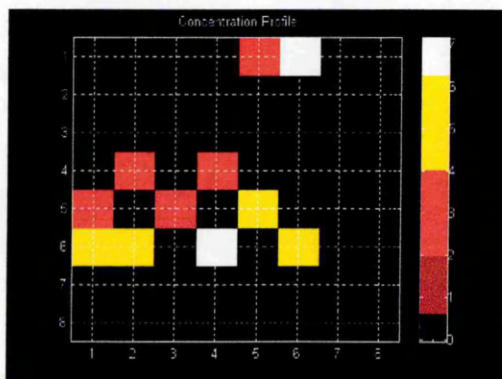


Figure 5.6a Matrix and concentration profile of the first sample representing small bubbles at 7 l/min

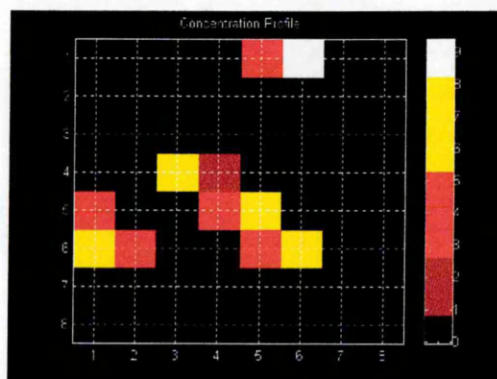


Figure 5.6b Matrix and concentration profile of the second sample representing small bubbles at 7 l/min

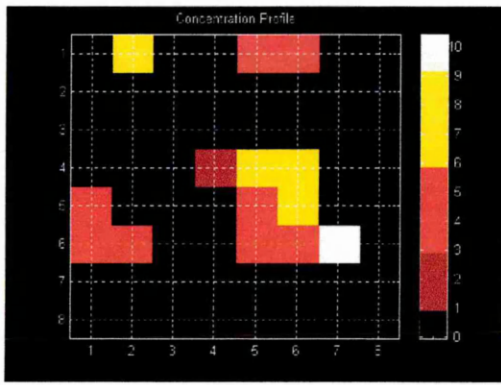


Figure 5.6c Matrix and concentration profile of the third sample representing small bubbles at 7 l/min

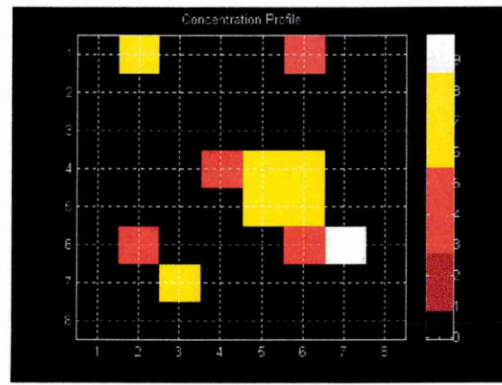


Figure 5.6d Matrix and concentration profile of the fourth sample representing small bubbles at 7 l/min

5.3.2 Concentration profiles of large bubbles

The following subsections show a sequence of selected images of large bubbles flowing in water, which were generated at various volumetric gas flow rates. These results are discussed in section 5.4.

5.3.2.1 Flow rate of 0.5 l/min

A sequence of images representing large bubbles generated at a volumetric gas flow rate of 0.5 l/min, are shown on figures 5.7a to 5.7d.

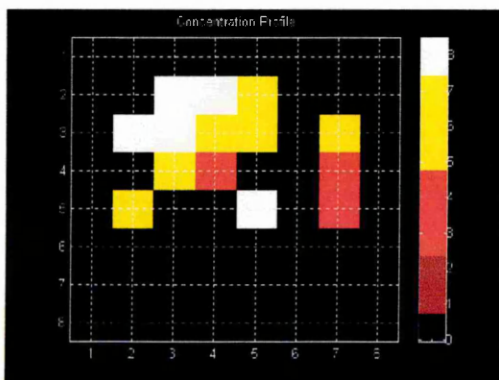


Figure 5.7a Matrix and concentration profile of the first sample representing large bubbles at 0.5 l/min

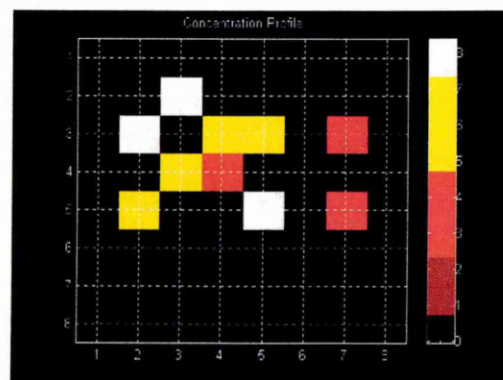


Figure 5.7b Matrix and concentration profile of the second sample representing large bubbles at 0.5 l/min

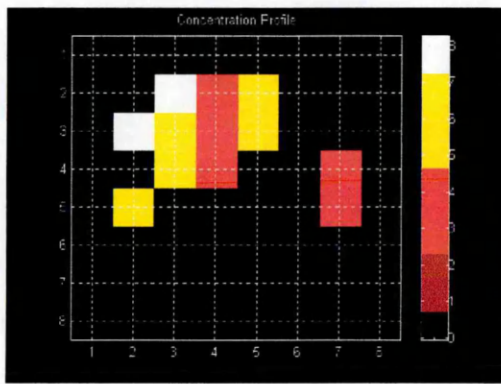


Figure 5.7c Matrix and concentration profile of the third sample representing large bubbles at 0.5 l/min

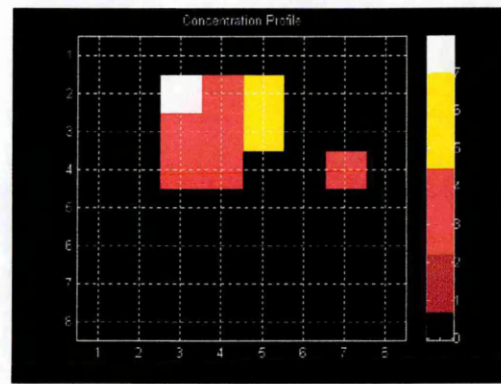


Figure 5.7d Matrix and concentration profile of the fourth sample representing large bubbles at 0.5 l/min

5.3.2.2 Flow rate of 3 l/min

A sequence of images representing large bubbles flowing at a volumetric flow rate of 3 l/min, are shown on figures 5.8a to 5.8d.

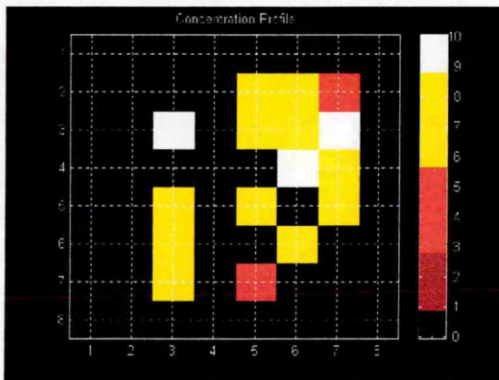


Figure 5.8a Matrix and concentration profile of the first sample representing large bubbles at 3 l/min

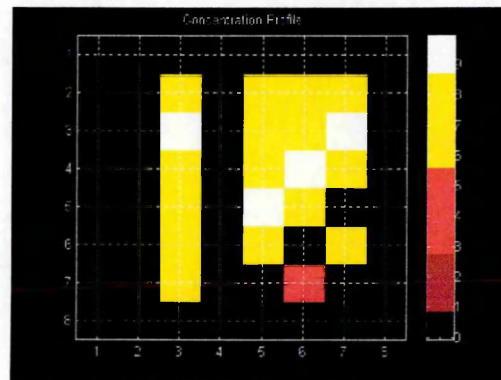


Figure 5.8b Matrix and concentration profile of the second sample representing large bubbles at 3 l/min

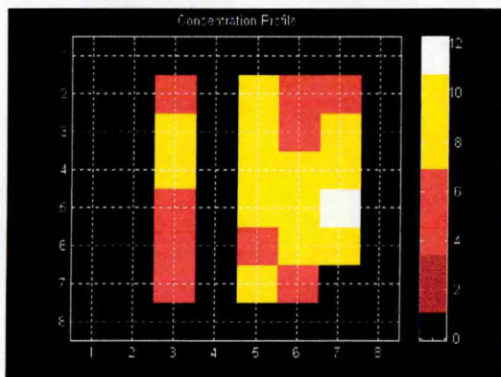


Figure 5.8c Matrix and concentration profile of the third sample representing large bubbles at 3 l/min

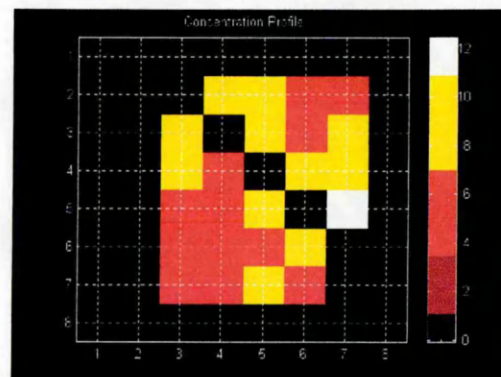


Figure 5.8d Matrix and concentration profile of the fourth sample representing large bubbles at 3 l/min

5.3.2.3 Flow rate of 5 l/min

A sequence of images representing large bubbles generated at a volumetric flow rate of 5 l/min, are shown on figures 5.9a to 5.9d.

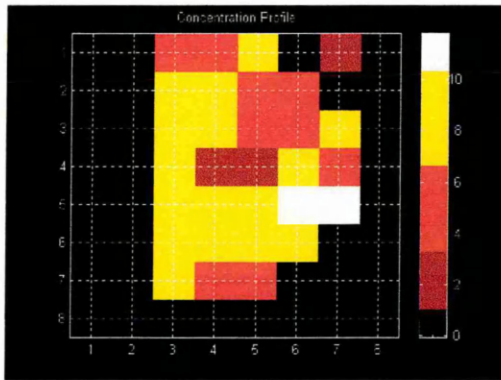


Figure 5.9a Matrix and concentration profile of the first sample representing large bubbles at 5 l/min

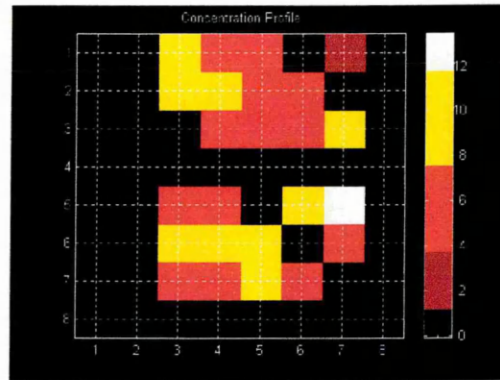


Figure 5.9b Matrix and concentration profile of the second sample representing large bubbles at 5 l/min

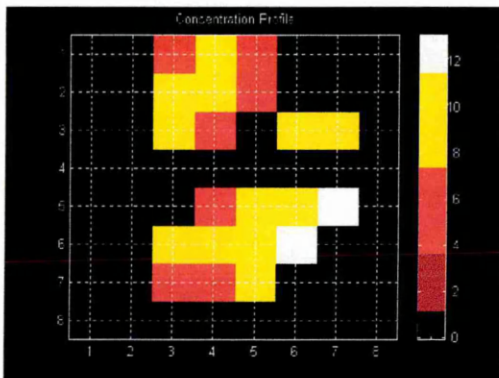


Figure 5.9c Matrix and concentration profile of the third sample representing large bubbles at 5 l/min

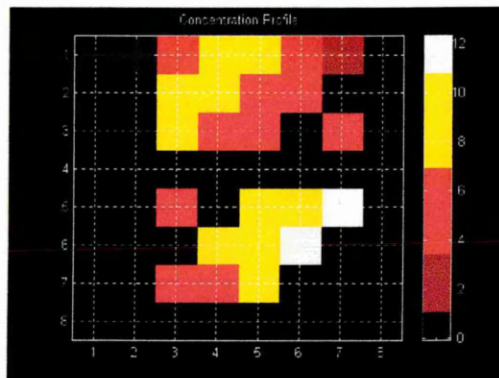


Figure 5.9d Matrix and concentration profile of the fourth sample representing large bubbles at 5 l/min

5.3.2.4 Flow rate of 7 l/min

A sequence of images representing large bubbles flowing at a volumetric flow rate of 7 l/min, are shown on figures 5.10a to 5.10d.

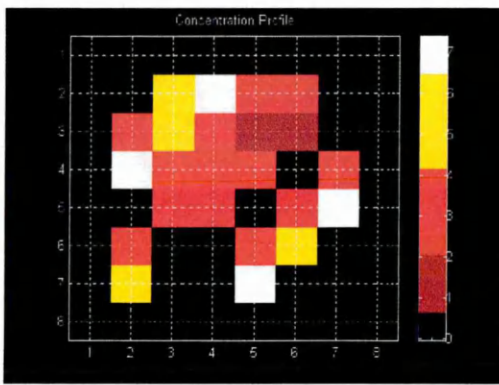


Figure 5.10a Matrix and concentration profile of the first sample representing large bubbles at 7 l/min

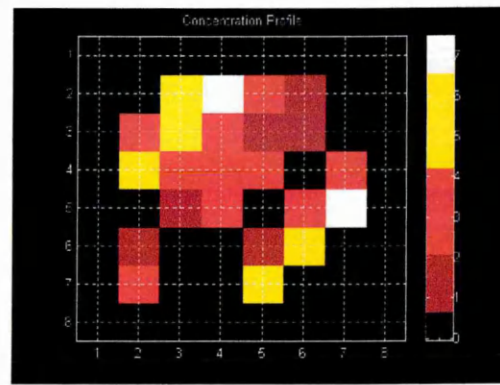


Figure 5.10b Matrix and concentration profile of the second sample representing large bubbles at 7 l/min

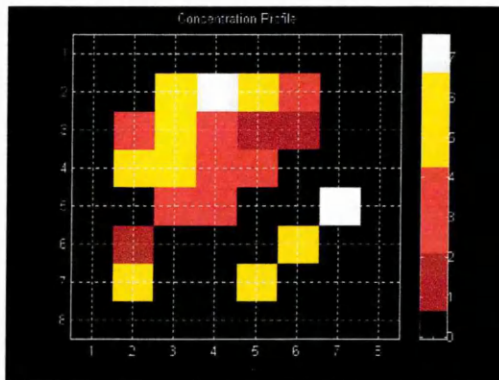


Figure 5.10c Matrix and concentration profile of the third sample representing large bubbles at 7 l/min

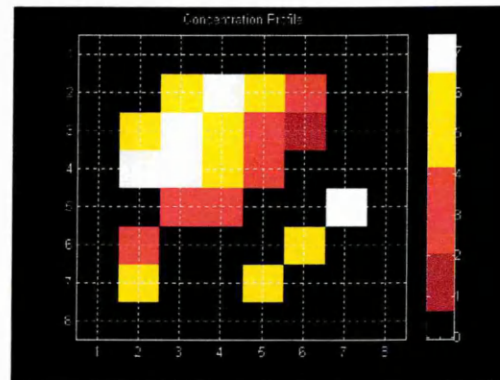


Figure 5.10d Matrix and concentration profile of the fourth sample representing large bubbles at 7 l/min

5.3.3 Concentration profiles of small bubbles at higher frequency

The experiments conducted as in section 5.3.1 were repeated but the data acquisition system was used to obtain 600 samples, with a sampling frequency of 20 kHz per channel, for each flow measurement. This high sampling rate was used to try to identify the movement of individual bubbles through the measurement cross section. These experiments made use of the two orthogonal projections system consisting of 8×8 optical fibre sensing arrays. The experiment was restricted to the 8×8 array for two reasons; firstly to enable a larger number of samples per channel to be collected and secondly to eliminate image registration problems due to the physical displacement of the 8×8 and 11×11 arrays. The sequence of images for small bubbles flowing at a

volumetric flow rate of 0.5 l/min, are shown on figures 5.11a to 5.11d. The results are discussed in section 5.4.

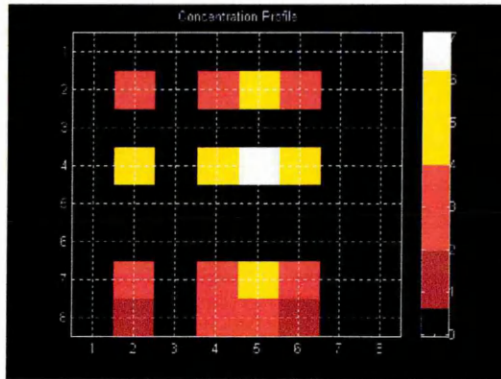


Figure 5.11a Matrix and concentration profile of the first sample representing small bubbles at 0.5 l/min

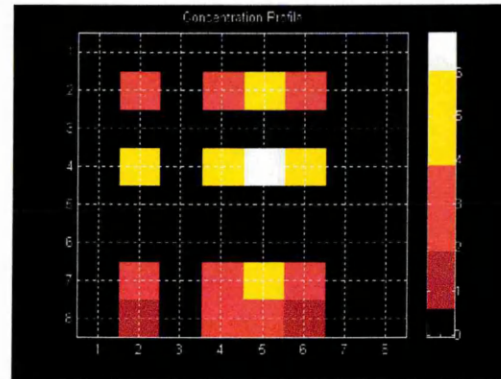


Figure 5.11b Matrix and concentration profile of the second sample representing small bubbles at 0.5 l/min

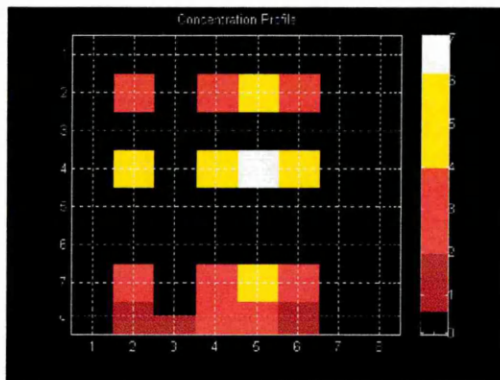


Figure 5.11c Matrix and concentration profile of the third sample representing small bubbles at 0.5 l/min

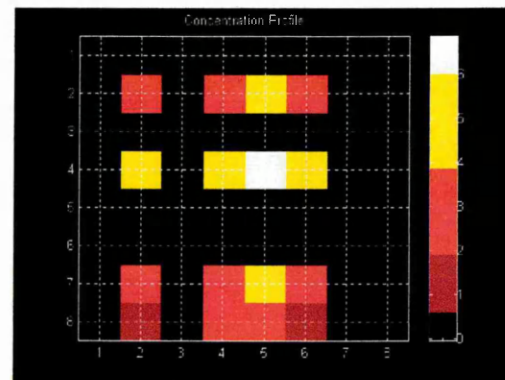


Figure 5.11d Matrix and concentration profile of the fourth sample representing small bubbles at 0.5 l/min

5.4 Discussion on concentration measurement

5.4.1 Gas flow rate calibration

The gas flow rate calibration graph (figure 5.1) shows the sum of voltages in all pixels within the flow pipe plotted against the volumetric flow rate of the bubbles for both small bubbles and large bubbles. The results shown in table 5.1 give a noise level of 4.9V, at zero flow, which corresponds to levels of 1.4 % of maximum flow reading for small bubbles and 1.2 % for large bubbles. The results obtained in section 5.2 indicate that the system reacts to large and small bubbles in a similar manner. However, saturation occurs

at higher flow rates with large bubbles than small bubbles. Figure 5.1 shows saturation occurring at a gas flow rate of 1 l/min for large bubbles and 3 l/min for small bubbles. This result is discussed further in sections 5.4.2 and 5.4.3. Empirical equations have been fitted to the results. For small bubbles the equation used is

$$\text{Sum of pixels} = -0.32x^6 + 7.76x^5 + 72.93x^4 + 340.26x^3 + 810.16x^2 + 860.21x + 4.9$$

where x is the gas flow rate in l/min.

The equation used for the large bubbles is

$$\text{Sum of pixels} = -0.31x^6 + 7.39x^5 - 67.63x^4 + 302.38x^3 - 694.29x^2 + 796.74x + 4.9$$

where x again is the gas flow rate in l/min.

5.4.2 Small bubbles

The majority of measurements was made with circulating water to ensure that the bubbles flowed upwards in the pipe. Consideration of the Reynolds number shows the water is flowing laminarly. The Reynolds, R_e number for water flowing through the rig at 3 l/min is given by:-

Velocity of water at 3 l/min in 80mm bore pipe is

$$v = \frac{3/60 \times 10^{-3}}{(0.08/2)^2} \approx 0.01 \text{ m/s}$$

If water density, $\rho = 10^3 \text{ kg/m}^3$, water velocity, $v = 0.01 \text{ m/s}$, pipe diameter, $d = 0.08 \text{ m}$, and water viscosity, ζ at $20^\circ\text{C} = 54 \times 10^{-5} \text{ kg/ms}$,

$$\text{then } R_e = \frac{\rho v d}{\zeta} = \frac{10^3 \times 0.01 \times 0.08}{54 \times 10^{-5}} = 1480$$

For $R_e < 2300$, the flow is laminar. So the water is flowing laminarly.

The flowing water appeared to keep the small bubbles in the centre of the pipe. This means that the majority of bubbles are confined to the central part of the measurement cross-section and only affect a few sensors. As the flow rate increases the bubbles get closer together until the few sensors being affected became saturated. The diagrams (figures 5.12a and 5.12b) indicate the flow of small bubbles at two different volumetric flow rates.

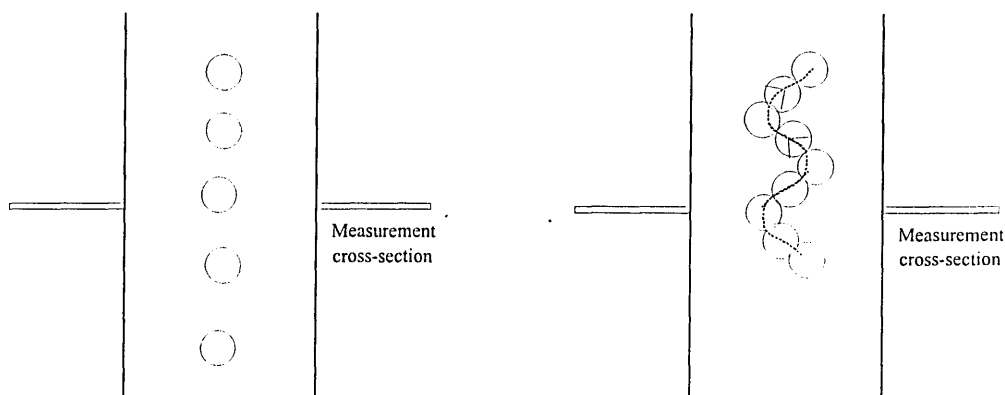


Figure 5.12a Small bubbles at a gas flow rate below 1 l/min

Figure 5.12b Small bubbles approximately at gas flow rates above 1 l/min

The gas flow rate calibration graph shows that initially from 0 to 1 l/min, the sum of the pixels increases, but from 1.5 l/min to 7 l/min, the sum of the pixels begins to decrease as the flow rate increases. Section 5.3.1 shows that the small gas bubbles are generally confined to the centre of the pipe. As the volumetric flow rate increases, more bubbles are released, resulting in only a few sensors being affected and as such, the sensors as well as the electronics have little time to recover from bubbles that flowed previously. Beyond 1 l/min, the graph shows saturation due to the large number of bubbles in the path of the optical fibre sensors.

In tomographic imaging the data sampling rate for the individual sensors can effect the images produced. The majority of the tomographic images were generated using a

sampling rate of 500 Hz/sample (500 concentration tomograms/s). Section 5.3.3 shows that with a very high rate, 20 kHz/sample (20,000 concentration tomograms/s), the bubble is virtually stationary. Further work is required to optimise the sampling rate, which should be related to bubble velocity (chapter 6).

5.4.3 Large bubbles

Large bubbles occupy a much larger cross section of the conveyor than small bubbles and so the majority of the sensors detect the presence of the bubbles. For this reason higher gas flow rates are measurable before saturation effects become dominant. The sum of the pixels increases over the flow rate of 0 to 3 l/min as shown in figure 5.1. However, beyond the volumetric flow rate of 3 l/min, the sum of the pixels begins to decrease as shown in figure 5.1. The diagrams (figures 5.13a and 5.13b) indicate the flow of large bubbles at two different volumetric flow rates.

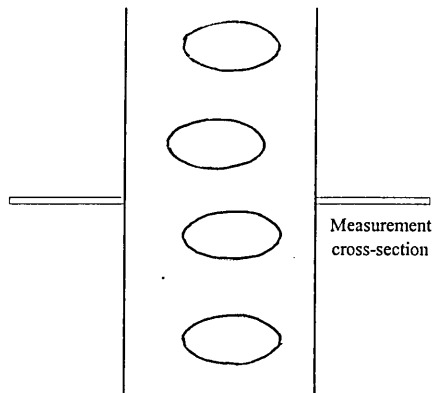


Figure 5.13a Large bubbles at a gas flow rate below 3 l/min

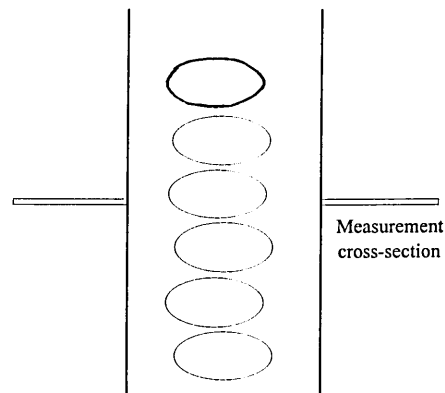


Figure 5.13b Large bubbles at gas flow rates above 3 l/min

Chapter 6

Velocity Measurements

6.1 Introduction

Cross correlating the upstream sensor time series with the downstream sensor time series generates a correlogram. The peak position of the correlogram provides the time taken for markers within the flow to travel between the upstream and downstream measurement cross-sections [Beck & Plaskowski, 1987]. Since the distance between the upstream and downstream sensors is known, the velocity of the marker can be calculated. Two methods of cross-correlation were attempted. The first approach cross correlates the data from upstream and downstream sensors. This method provides an average bubble velocity at the specific section in the flow pipe being monitored. The second method uses the upstream and downstream sensor arrays to generate two sequences of concentration profiles using the hybrid layergram back-projection algorithm (section 3.13). Individual upstream and downstream pixels have their concentration time series cross-correlated. This approach enables the velocity profile at the measurement cross-section to be investigated. By cross correlating non-aligned pixels radial velocity or swirl can be detected.

6.2 Sensor-to-sensor correlation

For the velocity measurement based on sensor-to-sensor correlation, voltages representing the grey level concentration, V_{glc} , with time from one of the downstream sensor were recorded and are shown in figure 6.1a and that from the corresponding upstream sensor are shown in figure 6.1b . In this experiment so as to enable a good

visual marker to be produced, the valve controlling the air supply was opened once for a few seconds and quickly closed. As a result, a large bubble of approximately 60 - 70 mm in diameter and 20 to 30 mm tall was released. By cross-correlating the signals coming out of the two sensors placed 15 cm above each other, the correlogram shown in figure 6.1c is obtained. The sampling frequency of the data acquisition system was fixed at 100 Hz. The peak value of the correlogram is 0.558 and occurs at a parametric time shift of 54 units (each unit represents 10 ms) corresponding to a transit time of 540 ms. The velocity was calculated as 0.278 m/s.

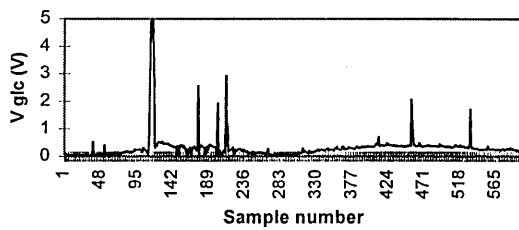


Figure 6.1a Downstream sensor output

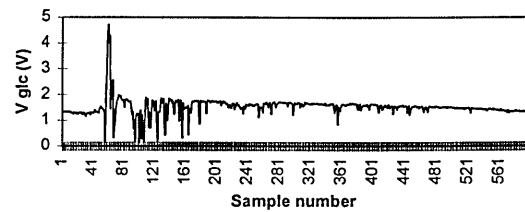


Figure 6.1b Upstream sensor output

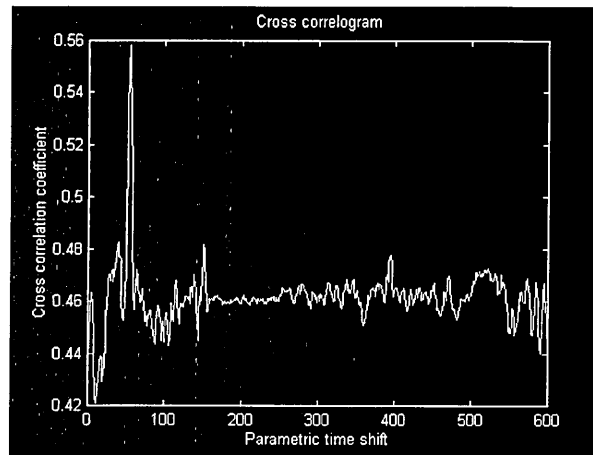


Figure 6.1c Cross-correlation of upstream and downstream sensors

The experiment was repeated using other sensors and the resulting correlogram is shown in figure 6.2. The peak value of the correlogram is 0.594 and occurs at a parametric time shift of 53 units (each unit represents 10 ms) corresponding to a transit time of 530 ms. From the correlogram, the velocity of the large bubble is calculated as 0.283 m/s. The

correlogram peak is well defined in both figures 6.1c and 6.2. The results obtained are within 1 parametric time unit i.e. 54 and 53 time units, which is the resolution of the measurement.

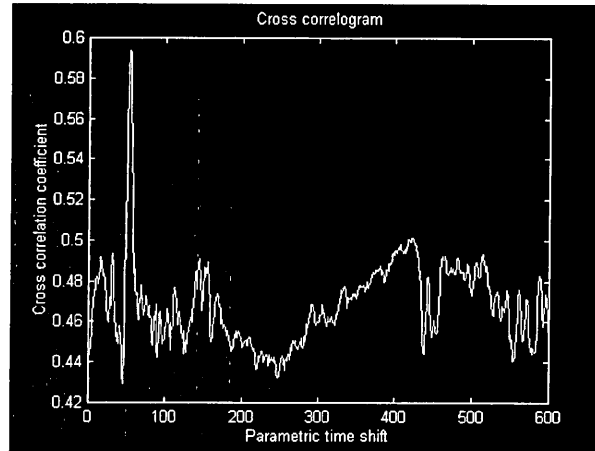


Figure 6.2 Cross correlation of upstream and downstream sensors

6.3 Pixel-to-pixel correlation

Pixel-to-pixel correlation has been carried out on flows containing large bubbles. Six hundred samples were obtained at a sampling rate of 100 Hz/sample for each sensor. Each block of measurements was used to calculate an upstream and downstream concentration profile (section 5.3). This was repeated for all six hundred samples. A time varying grey level was produced for each upstream and downstream pixel consisting of a sequence of six hundred values. Upstream pixel (4,4) and downstream pixels (3,3), (3,4), (3,5), (4,3), (4,4), (4,5), (5,3), (5,4) and (5,5) are considered for grey level cross correlation. The numbering of pixels in the flow pipe is shown in figure 6.3.

1,1	1,2	1,3	1,4	1,5	1,6	1,7	1,8
2,1	2,2	2,3	2,4	2,5	2,6	2,7	2,8
3,1	3,2	3,3	3,4	3,5	3,6	3,7	3,8
4,1	4,2	4,3	4,4	4,5	4,6	4,7	4,8
5,1	5,2	5,3	5,4	5,5	5,6	5,7	5,8
6,1	6,2	6,3	6,4	6,5	6,6	6,7	6,8
7,1	7,2	7,3	7,4	7,5	7,6	7,7	7,8
8,1	8,2	8,3	8,4	8,5	8,6	8,7	8,8

Figure 6.3 Arrangement of pixels within the flow pipe

6.3.1 Pixel-to-pixel correlation on large bubbles

Figure 6.4a shows the voltage representing the grey level concentration, V_{glc} , with time for upstream pixel 4,4; figure 6.4b shows the corresponding voltage variation for downstream pixel 3,3. Cross-correlation of the upstream pixel 4,4 and downstream pixel 3,3 produced the correlogram shown in figure 6.4. The peak value of the correlogram is 9.12 and occurs at a parametric time shift of 57 units (again each unit represents 10 ms) corresponding to a transit time of 570 ms. From the correlogram, the velocity of the large bubble is calculated as 0.263 m/s compared with 0.278 m/s for sensor-to-sensor correlation.

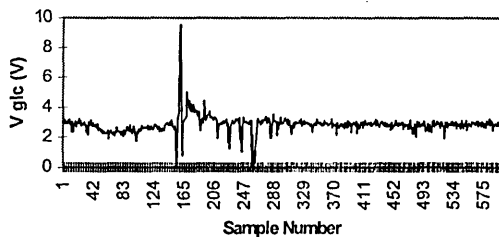


Figure 6.4a Upstream concentration signal at pixel 4,4

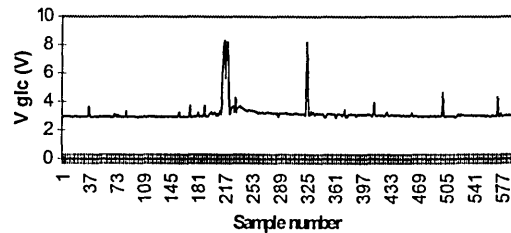


Figure 6.4b Downstream concentration signal at pixel 3,3

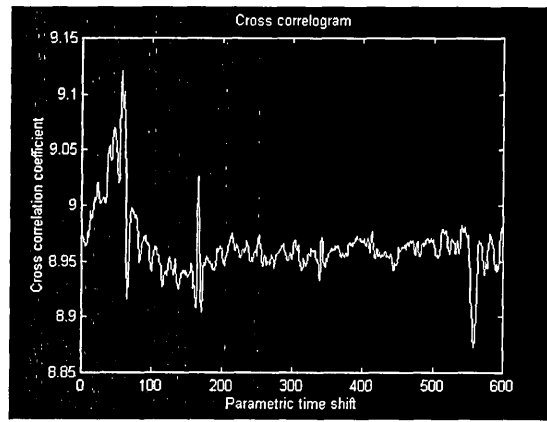
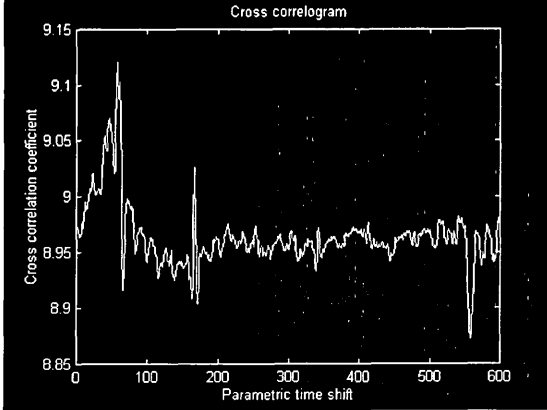
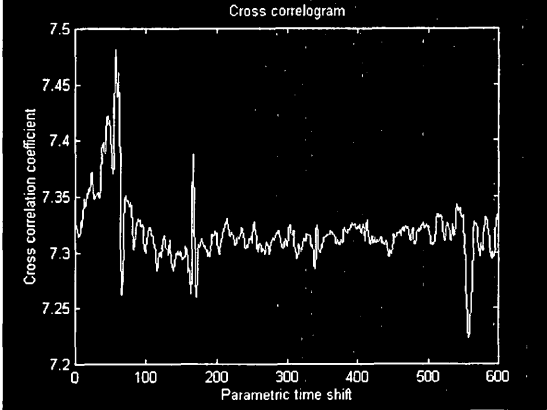
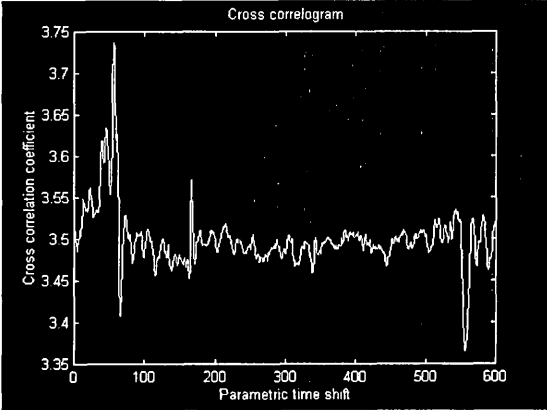
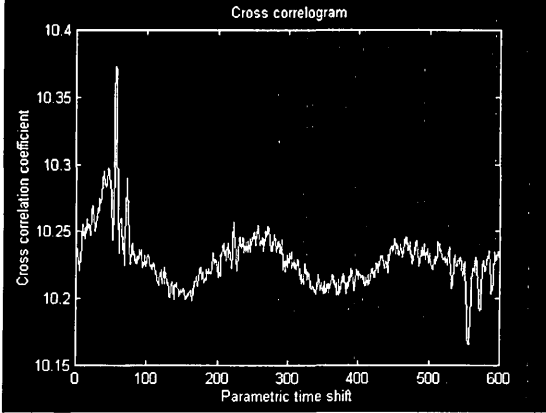
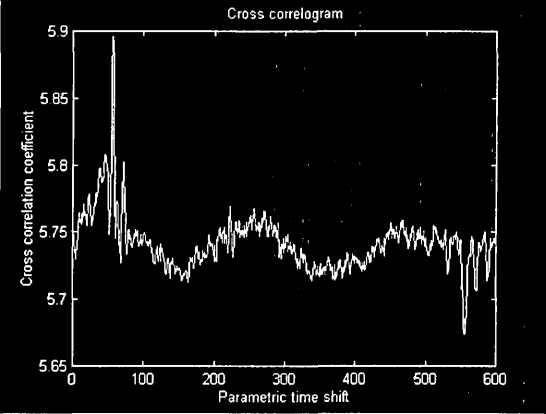
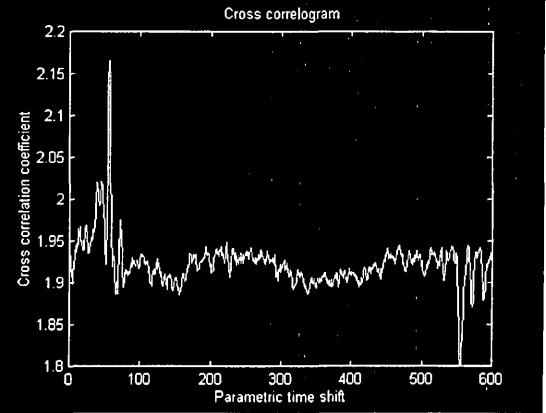


Figure 6.4c Cross correlation of upstream concentration at pixel 4,4 and downstream concentration at pixel 3,3

This process of cross correlating upstream and downstream pixels was repeated and the results are tabulated in table 6.1.

Correlogram	Peak value	Parametric delay	Time delay (ms)	Velocity (ms^{-1})
 <p data-bbox="257 646 538 719">Upstream pixel 4,4; downstream pixel 3,3</p>	9.12	57	570	0.263
 <p data-bbox="257 1217 538 1289">Upstream pixel 4,4; downstream pixel 3,4</p>	7.48	57	570	0.263
 <p data-bbox="257 1810 538 1921">Upstream pixel 4,4; downstream pixel 3,5</p>	3.73	56	560	0.268

Correlogram	Peak value	Parametric delay	Time delay (ms)	Velocity (ms^{-1})
 <p data-bbox="253 612 529 725">Upstream pixel 4,4; downstream pixel 4,3</p>	10.37	56	560	0.268
 <p data-bbox="253 1223 529 1336">Upstream pixel 4,4; downstream pixel 4,4</p>	5.90	56	560	0.268
 <p data-bbox="253 1834 529 1947">Upstream pixel 4,4; downstream pixel 4,5</p>	2.17	56	560	0.268

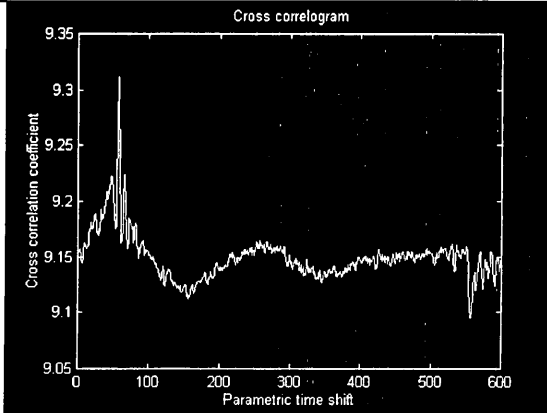
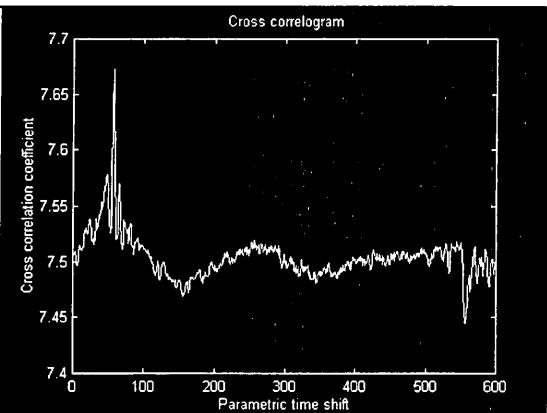
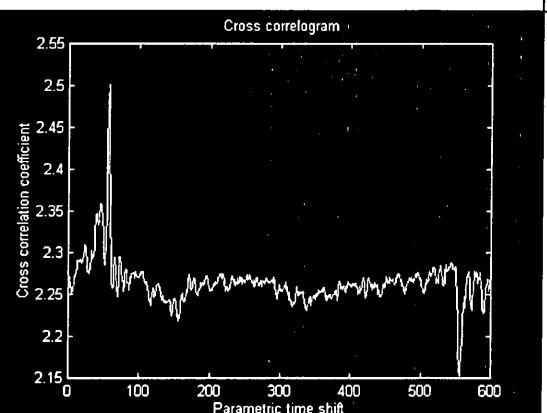
Correlogram	Peak value	Parametric delay	Time delay (ms)	Velocity (ms ⁻¹)
 <p>Upstream pixel 4,4; downstream pixel 5,3</p>	9.31	57	570	0.263
 <p>Upstream pixel 4,4; downstream pixel 5,4</p>	7.67	57	570	0.263
 <p>Upstream pixel 4,4; downstream pixel 5,5</p>	2.50	57	570	0.263

Table 6.1

The results presented in table 6.1 show that the velocities of the bubbles are similar even though the cross-correlations are carried out on different pixels. In all cases considered, the correlogram peak is well defined and the cross correlation of upstream and downstream pixel time histories appears to work satisfactorily. Table 6.2 summarises the velocities obtained using pixel-to-pixel correlation. Two interpretations of these results are possible. Firstly, the resolution in parametric time is 1 unit in 56 or 57 corresponding to a resolution of 2 %. This means the velocity is 0.266 ms^{-1} with a tolerance of $\pm 0.005 \text{ ms}^{-1}$ (i.e. $0.261 - 0.271 \text{ ms}^{-1}$). Secondly, if the velocities are regarded as accurate measurements then pixels 3,5; 4,3; 4,4 and 4,5 show that a part of the bubble is moving with slightly larger velocity than in the other pixels.

The velocities obtained from pixel-to-pixel cross correlation are also similar to that obtained from sensor-to-sensor cross correlation.

Pixel (3,3) Velocity = 0.263 m/s	Pixel (3,4) Velocity = 0.263 m/s	Pixel (3,5) Velocity = 0.268 m/s
Pixel (4,3) Velocity = 0.268 m/s	Pixel (4,4) Velocity = 0.268 m/s	Pixel (4,5) Velocity = 0.268 m/s
Pixel (5,3) Velocity = 0.263 m/s	Pixel (5,4) Velocity = 0.263 m/s	Pixel (5,5) Velocity = 0.263 m/s

Table 6.2 Map of velocities obtained using pixel-to-pixel cross correlation for nine central downstream pixels

6.3.2 Pixel-to-pixel correlation on small bubbles

Several experiments have been carried out to measure the velocity of small bubbles. In the experiments, the distance between the upstream and downstream sensor planes is reduced to 3 cm. However, the results did not produce transit time measurements similar in value to that of large sized bubbles. This could be attributed to the fact that the sensor

spacing is much larger than the size of the bubbles. A typical correlogram is shown in figure 6.5. There is no single peak, which can be identified for the purpose of calculating the velocity. This correlogram may arise because the small bubbles are very similar in size and have a reasonably regular frequency. Thus different bubbles may correlate with one another. To enable the system to perform cross-correlation on small-sized bubbles, the sensor spacing should be of the order of the bubble size or smaller than the expected bubble size (see section 7.3). At the relatively low water and bubble velocities used in this thesis, spatial filtering effects [Hammer & Green, 1982] are not relevant due to the high signal bandwidth of the system [Green et al, 1995].

The images are produced at a frame rate of 100 per second. Considering this as the sampling frequency, the corresponding Nyquist frequency is 50 frames per second. Small bubbles travelling at 0.263 m/s will have moved 5.3 mm. The small bubbles appear to be in the range 1 - 10mm, with a mean of 5mm. For the velocity measurements, the individual bubbles were well spaced i.e. approximately 15 - 20mm, so the possibility of image aliasing does not arise.

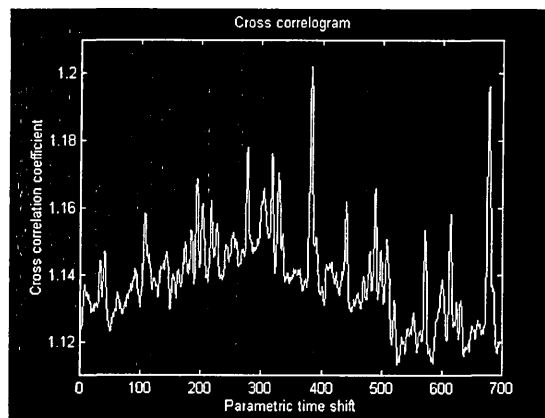


Figure 6.5 A correlogram obtained from pixel-to-pixel cross-correlation of small bubbles

Conclusions and suggestions for future work

7.1 Conclusions

An optical tomographic measurement system has been successfully designed and an initial evaluation of its performance made. The specific objectives of the thesis have been fulfilled as follows :-

- Chapter three presents an investigation on the interaction between a collimated beam of light and a spherical bubble. Models of an optical tomographic system using various projection geometries and the results of the modelling using layergram back-projection and hybrid reconstruction algorithms aimed at optimising the design of the tomography system (objectives one, two and three) are also presented.
- The optical fibre lens is modelled in chapter three and a description of its construction is described in chapter four (objective four).
- The transducer design is presented in chapter four (objective five).
- The work presented in chapter five shows that the measurement system is suitable for producing concentration profiles of the tomographic images (objective six).
- The work presented in chapter six shows that the system can also measure the velocity of the flow and determine the velocity profiles (objective seven).
- Suggestions for further research are presented in chapter seven (objective eight).

7.2 Contribution to the field of process tomography

The combination of two orthogonal and two rectilinear projections system based on optical fibres is capable of making concentration measurements of small bubbles in water of diameter 1-10 mm and volumetric flow rates up to 1 l/min, and large bubbles in water of diameter 15-20 mm and volumetric flow rates up to 3 l/min on a hydraulic conveyor. Two arrays, each of thirty eight sensors, are capable of performing velocity measurements using the same gas bubbles by cross correlation. Tomograms of the concentration profile have been determined and the optical sensors are sensitive to bubbles of various sizes.

7.3 Suggestions for future work

- Ideally in an industrial environment, it would be preferable to use laser as the light source due to its monochromatic and coherent characteristics. It may be more cost effective to have two laser sources with associated high grade collimation, combined with a system of beam splitters allowing radiation to cover all the projections in the tomographic cross-section. Alternatively, optical fibres could be used as light channels to carry the light into the measurement section.
- Increase the number of views per light sources for each pixel, i.e. initially use 16×16 orthogonal projections and 22×22 rectilinear projections to increase resolution. The projections should be arranged in the same plane or determine an algorithm which compensates for non-aligned projections. This algorithm could use velocity to determine transit time between projections.
- In this thesis the data acquisition system that was used sampled the sensors sequentially. This causes problems for both concentration and velocity profile

reconstructions. Sampling all the sensors at the same instant would ensure that the data for a specific time were accurately related. It would ease the time registration of axially displaced projection data, because velocity measurement would provide the necessary time delay between projections. High speed sampling and analogue to digital conversion would provide time for the digital data to be read into the PC sequentially.

- The calibration of the sensors should be investigated. Ideally all the sensors should have the same zero and sensitivity to light variation. This could be checked by feeding light from a fixed source, via a mechanical chopper into an optical fibre and then to the electronics. All the optical fibres and associated amplifiers should be checked. Further thought should be given to checking/calibrating the measurement on line so that defects in the pipe may be compensated.
- Further investigations should be carried out on reconstruction algorithms. Different forms of filtering techniques should be investigated. The hybrid reconstruction algorithm should be developed for use with two component flows, where the conveyed component concentration is low i.e. measurement of crude oil concentration in water discharged by tankers flushing their oil storage tanks.
- An investigation should be carried out on capturing the flow using CCD (charge-coupled devices). Photographs of the motion of particles/droplets in a flow could be taken. CCDs can detect a broad spectrum of light of different intensities. The CCD video cameras could provide velocity information if the frame rate is known.
- Further work is required to optimise the lens curvature. The lens production fixture should be modified so that the lens surface is smoother, providing a more collimated beam and so that the fibre cladding is not affected by the surface heating process.

- The current combination of on-line measurement and off-line computation should be replaced with an on-line measurement system. The concentration and cross correlation algorithms should be optimised for speed. If necessary some of the calculations should be carried out in parallel. Potential industrial users should be asked if they require on line images of concentration profile, which is heavy on computation and display time, compared with the concentration matrices of a single volume flow rate reading.
- Multi modality tomography should be investigated with in which the optical tomographic system can be combined with other types of sensing with the aim of comparing the accuracy of the measurements and increasing the understanding on the flow process.
- The cross correlation can be improved by hardware correlators or special digital signal processing chips embedded in the data acquisition system. To enable the system to perform cross-correlation on small-sized bubbles, the projection axial spacing should be of the order of the bubble size or smaller than the expected bubble size. Also, the number of optical fibres should be increased, possibly doubled, to maximise the probability of detecting the small bubbles. A dedicated data capture system should be employed to increase the data bandwidth.
- The electronic design of the system could be optimised to include fast data acquisition and signal processing chips. The sampling time of the data capturing system should be improved to allow information on higher velocity flows to be collected. Direct memory access could be incorporated so that more data can be stored to allow improved averaging of the correlations and voltage profiles. Correlations and averaging could be done by dedicated signal processing circuits, which would speed up the overall system.

- The number of sensors in an array should be increased until there is no discernible difference in output value between adjacent pairs. This will allow the maximum amount of data to be collected for use in image reconstruction. Each sensor is providing a view, an increase in the number of views generally helps to improve the image resolution.
- Experiments on other arrangements of optical fibre sensing arrays such as two orthogonal, a combination of one orthogonal and two rectilinear, three and four fan-beam projections should be carried out in order to compare their accuracy and see whether measured results agree with the predictions in section 3.13.
- The electronics circuit should be redesigned to optimise the gain, bandwidth and signal to noise ratio using the latest, improved operational amplifiers which have higher bandwidth, lower noise and drift e.g. OPA 2137. Programmable gain amplifiers with low offset are needed to improve the receiver circuit.
- The measurement system should be tested on an industrial hydraulic flow rig to determine the concentration and velocity measurement limitations and accuracies. Different sizes and types of droplets should be used with the measurement system on the conveyor to investigate the range of materials which it is suitable. These measurements could also be used for an evaluation of the effects of droplet size.
- This project is confined to investigating bubbles flowing upwards in water. Other media such as oil, which has a different attenuation coefficient should be investigated. Investigations should also be carried out on the effect of actual operating processes in which the surfaces of the pipe may become fouled e.g. with viscous crude oil, which will reduce the sensitivity and the resolution of the sensor. For crude oil infra red light of an appropriate wavelength could be used.

- The modelling (chapter 3) indicates that more accurate images were reconstructed when the modelled measurement system provided equal weighting for each pixel. Further modelling should be carried out to investigate different weighting, perhaps non-linear weighting, in the sensitivity matrix to allow for non-equal path lengths.
- The bubbles could be injected at different heights up the flow pipe to investigate the effect of pipe length on reproduction of flow regimes which are useful for developing process tomography systems.
- The bubbles will generally will reflecting and attenuating the light beam. Further work can be done on modelling and carrying out experiments on the effect of bubbles scattering the light. This may require some of the detectors to be mounted radially around the flow pipe.
- This investigation has been restricted to vertical flow. The system could be tested for flow moving in various directions i.e. horizontal, downwards vertical and the flow pipe inclined at different angles to the vertical.
- Application of image segmentation algorithms to the reconstructed images should be investigated, which may provide opportunities to determine specific features of the flow.
- The measurement system could be used with a wider range of concentrations and velocities than has been described in this work. It is expected that the error in measurement will increase when several droplets intercept the same beam simultaneously.
- The longer term aim of this project is to determine the volumetric flow rate of the conveyed phase. This can be achieved by combining the concentration profiles.

$$\text{Volumetric flow rate} = \sum_{t=0}^{t=T} KC_t V_t$$

where C_t is the instantaneous concentration at time t , V_t is the velocity applicable to this concentration and K is a constant of proportionality.

- In this project, measurements were made on concentration and velocity profiles. Further thought should be given to characterising the droplet by modifying the transducer circuit and using more/smaller diameter optical fibres.

- A dedicated sensor calibration system should be designed. This could be based on a voltage controlled light source or laser light source, followed by a mechanical or electrical light chopper. The chopped light could be fed through the optical fibre system into the electronic sensor. In this manner both optical fibre and electronics could be calibrated (section 4.3.3). The dedicated system should be under the control of a PC, with automatic data logging of the required measurements.

- This thesis has considered both path length and optical attenuation models. However, many systems may have both effects present e.g. small bubbles or the edges of larger bubbles may prevent light from reaching the sensor (path length model) and some bubbles may simply cause an optical attenuation. A combination of path length and optical attenuation models should be investigated with the aim of predicting the effect of bubble size and concentration.

REFERENCES

- Abdul Rahim R., *A tomographic imaging system for pneumatic conveyors using optical fibres*, PhD Thesis, Sheffield Hallam University, 1996.
- Abdul Rahim R., Green R.G., Horbury N.M., Dickin F.J., Naylor B.D. & Pridmore T.P., An investigation into the use of optical fibres to produce on-line particle size information and tomographic images for hydraulic processes, *Proc. ECAPT 95*, pp. 134-138, Norway, 1995.
- Abdullah M.Z., Quick S.V. & Dickin F.J., Quantitative algorithm and computer architecture for real-time image reconstruction in process tomography, *Proc European Concerted Action on Process Tomography, Manchester*, 1992.
- Abel L.A. and Thomas P., *Engineering Materials Handbook*, Vol. 2, ASM International, 1988.
- Abro E. and Johansen G.A., Void fraction and flow regime determination by low-energy multi-beam gamma ray densitometry, *Proc. First world congress on industrial process tomography*, Buxton, pp. 339 - 343, 1999.
- Altobelli S., Givler R.C. and Fukushima E., Velocity and concentration measurements of suspensions by nuclear magnetic resonance imaging, *Journal of Rheology*, 35, pp. 721 - 734, 1991.
- Beck M.S., Feature on process tomography - Introduction, *Measurement + Control*, Vol. 30, No. 7, p. 196, 1997.
- Beck M.S., Byars M., Dyakowski T., Waterfall R., He R., Wang S.J. & Yang W.Q., Principles and industrial applications of electrical capacitance tomography, *Measurement + Control*, Vol. 30, No. 7, pp. 197-200, 1997.
- Beck M.S. & Plaskowski A., *Cross correlation flow meters: their design and application*, Adam Hilger, 1987.
- Bevir M.K., The theory of induced voltage electromagnetic flowmeters, *J. Fluid Mech.*, pp. 577 - 590, 1970.
- Bidin A.R., *Electrodynamics sensors and neural networks for electrical charge tomography*, PhD Thesis, Sheffield Hallam University, 1993.
- Burns D.H., Optical tomography for three-dimensional spectroscopy, *Applied Spectroscopy*, 48 (5), pp. 12A - 19A, 1994.
- Chin A.D.A., Butler P.B., & Luerkens D.W., Influence of particle shape on size measured by the light blockage techniques, *Powder Technology*, 54, p. 99-105, 1988.
- Clarke A.J., Jia X. & Williams R.A., Verification of distinct element modelling of particle separation in laboratory jig using positron emission tomography, pp. 91-96, *Proc. Frontiers in Industrial process tomography II*, The Netherlands, 1997.

- Daily W., Ramirez A., LeBrecque & Binley A., Detecting leaks in hydrocarbon storage tanks using electrical resistance tomography, *Proc. Frontiers in Industrial Process Tomography* ed. D.M. Scott & R.A. Williams, New York, Engineering Foundation, p. 309, 1995.
- Daniels A.R., *Dual modality tomography for the monitoring of constituent volumes in multi-component flows*, PhD Thesis, Sheffield Hallam University, 1996.
- Dickin F.J., Tomography for improving the design and control of particulate processing systems, *KONA - Powder and Particle*, 10, pp. 4-14, 1992.
- Dugdale W.P., *An optical instrumentation system for the imaging of two-component flow*, PhD Thesis, University of Manchester, 1994.
- Durrani T.S. & Greated C.A., *Laser systems in flow measurement*, Plenum Press, 1977.
- Dyakowski T., Process tomography applied to multi-phase flow measurement, *Measurement Science and Technology*, 7, pp. 343 - 353, 1996.
- Farnell Catalogue, p. 128, April 1999.
- Fiber Collimators/Focusers, OZ Optics Ltd., 1998.
- Fordham E.J., Holmes A., Ramos R.T., Simonian S., Huang S.M. and Lenn C.P., Multi-phase fluid discrimination with local fibre-optical probes, *Measurement Science and Technology*, 10, pp. 1329 - 1337, 1999.
- Gladden L.F. and Alexander P., Applications of nuclear magnetic resonance imaging in process engineering, *Measurement Science and Technology*, 7, pp. 423 - 435, 1996.
- Gonzalez R.C. & Woods R.E., *Digital image processing*, Addison-Wesley, 1992.
- Govier G. W. & Aziz K., *The flow of complex mixtures in pipes*, Robert E. Krieger, 1970.
- Grassler T. & Wirth K.E., X-ray computer tomography - potential and limitation for the measurement of local solids distribution in circulating fluidized beds, *Proc. First World Congress on Industrial Process Tomography*, Buxton, pp. 402 - 209, 1999.
- Green R.G. & Cunliffe J.M., A frequency modulated capacitance transducer for on-line measurement of two-component fluid flow, *IMEKO Journal of Measurement*, Vol. 1, No. 4, pp. 191 - 195, October - December 1983.
- Green R.G., Horbury N.M., Abdul Rahim R., Dickin F.J., Naylor B.D. & Pridmore T.P., Optical fibre sensors for process tomography, *Measurement Science & Technology*, Vol. 6, pp. 1699 - 1704, 1995.
- Hammer E.A., *Three-component flow measurement in oil/gas/water mixtures using capacitance transducers*, PhD Thesis, 1983.

- Hammer E.A. & Green R.G., The spatial filtering effect of capacitance transducer electrodes, *J. Physics E: Scientific Instruments*, Vol.16, pp. 438 - 443, 1982.
- Hammer E.A. & Johansen G.A., Process tomography in the oil industry - state of the art and future possibilities, *Measurement + Control*, Vol. 30, pp. 212 - 216, 1997.
- Hecht J., *Understanding Fiber Optics*, Prentice-Hall, 1999.
- HIAC-ROYCO, Particle counting: A valuable tool for many industries, *Application Note 212*, 1998.
- Horowitz P. & Hill W. , *The Art of Electronics*, p. 223, Cambridge University Press, 1993.
- Hou R., Hunt A. & Williams R.A., Acoustic monitoring of pipeline flows: particulate slurries, *Powder Technology*, 106, 1999, pp. 30 - 36, 1999.
- Isaksen O. and Nordtvedt J.E., Capacitance tomography: Reconstruction based on optimisation theory, *Proc. ECAPT 1992*, pp. 178 - 189, 1992.
- Jackson R.G. , The development of optical systems for process imaging in :- Williams, R.A. & Beck, M.S. (ed), *Process Tomography - Principles, Techniques and Applications*, Butterworth-Heinemann, 1995, pp 167 - 180, 1995.
- Jalie M., *The Principles of Ophthalmic Lenses*, The Association of Dispensing Opticians, London, 1977.
- Johansen G.A., Froystei, T., Hjertake, B.T., Isakse, O., Olsen O., Strando, S.K., Olsen T.S., Abro E., McKibben B., Heggsta, S. and Hammer E.A., The design of a dual model tomograph for three-component flow imaging, , *Proc. ECAPT 94 Process tomography: A strategy for industrial exploitation*, pp. 75-80, Oporto, 1994.
- Khan S.H., Xie C.G. and Abdullah F., Computer modelling of process tomography sensors and systems in :- Williams, R.A. & Beck, M.S. (ed), *Process Tomography - Principles, Techniques and Applications*, Butterworth-Heinemann, pp. 325 - 365, 1995.
- King N.W., Purfit G. L. & Pursley W. C., A laboratory facility for the study of mixing phenomena in water/oil flows, *Proc. Symposium Flow metering and proving techniques in the offshore oil industry*, Institute of Measurement and Control, Aberdeen, pp. 233 - 241, 1983.
- Longhurst R.S., *Geometrical and Physical Optics*, Second edition, Longman, 1967.
- Mann R., Modelling needs in process tomography, *Proceedings ECAPT 1995*, Bergen, pp. 440 - 452, 1995.
- McKee S.L., Applications of nuclear magnetic resonance tomography in :- Williams R.A. & Beck M.S. (ed), *Process Tomography - Principles, Techniques and Applications*, Butterworth-Heinemann, pp. 539 - 548, 1995.

- Menemenlis D., Webb T., Wunsch C., Send U., & Hill C., Basin-scale ocean circulation from combined altimetric, tomographic and model data, *Nature*, 385, pp. 618 - 621, 1997.
- Nordin M.J., *An image reconstruction algorithm for a dual modality tomographic system*, PhD Thesis, Sheffield Hallam University, 1995.
- Optical Reflectance Measurement, *Messtechnik Schwartz GMBH brochure*, p. 1, 1997.
- Plaskowski A., Beck M.S., Thorn R. & Dyakowski T., *Imaging Industrial Flows*, Institute of Physics Publishing Ltd., p. xi, 1995.
- Rahmat M.F., *Instrumentation of particle conveying using electrical charge tomography*, PhD Thesis, Sheffield Hallam University, 1996.
- Ramli N., *Tomographic imaging instrumentation of pneumatic particle conveying using optical fibre sensors*, MPhil/PhD Transfer Report, Sheffield Hallam University, 1998.
- Schlaberg H.I., Yang M. & Hoyle B.S., Ultrasound reflection tomography for process application, *Proc. Frontiers in Industrial process tomography*, The Netherlands, pp. 173-178, 1997.
- Southern P.W. & Deloughry R.J., Imaging of oil/gas/water/sand interface levels in an oil separation vessel, pp. 181 - 184, *ECAPT 93 Process tomography: A strategy for industrial exploitation*, Karlsruhe, 1993.
- Tunnecliffe A.H. & Hirst J.G., *Optics*, Association of Dispensing Opticians, 1981.
- Ungar S., *Fibre Optics: Theory and Applications*, John Wiley and Sons, 1997.
- Wang M., Three-dimensional effects in electrical impedance tomography, *Proc. First world congress on industrial process tomography*, pp. 410 - 415, Buxton, 1999
- Wang M., Mann R. & Dickin F.J., Electrical resistance tomographic sensing systems for industrial applications, *Proc. Frontiers in industrial process tomography II*, The Netherlands, pp. 179 - 184, 1997.
- Williams R.A. & Beck M.S., Introduction to Process Tomography in :- Williams, R.A. & Beck, M.S. (ed), *Process Tomography - Principles, Techniques and Applications*, Butterworth-Heinemann, pp 3-12, 1995.
- Williams R.A., Dyakowski T., Xie C.G., Luke S.P., Gregory P.J., Edwards R.B., Dickin F.J. & Gate L.F., Industrial measurement and control of particulate processes using electrical tomography, *Process Tomography 95 Implementation for Industrial Processes*, Manchester, 1995, pp. 3-15, 1995.
- Xie C.G., Huang S.M., Hoyle B.S., Thorn R., Lenn C.P. & Beck M.S., Electrical capacitance tomography for flow imaging: system model for development of image

reconstruction algorithms and design of primary sensors, *IEE Proceedings-G*, Vol. 139, No. 1, pp. 89-98, February 1992.

Xie Z., *Optical tomography of small bubble distribution measurement using filtered backprojection technique*, M.Phil. Thesis, University of Manchester, 1993.

PUBLICATIONS RELATING TO THE THESIS

Journals

1. Optical sensor configurations for process tomography, S.Ibrahim, R.G. Green, K. Dutton, K.Evans, A. Goude & R. Abdul Rahim, *Measurement, Science and Technology*, Vol. 10, pp. 1079-1086, 1999.
2. An integrated optical fibre and lens system for tomography, S.Ibrahim, R.G. Green, K. Dutton, K.Evans & B. Naylor, *Measurement + Control*, Vol. 33, pp. 109 – 112, May 2000.

Conferences

1. Optical fibres for process tomography: a design study, S.Ibrahim, R.G. Green, K. Dutton, R. Abdul Rahim, K.Evans & A. Goude, *Proc. First World Congress on Industrial Process Tomography*, Buxton, United Kingdom, pp. 511-516, 14-17 April, 1999.
2. Modelling of optical fibres for process tomography, S.Ibrahim, R.G. Green, K. Dutton, R. Abdul Rahim, K.Evans, A. Goude & R. Abdul Rahim, *Proc. International Conference on Robotics, Vision and Parallel Processing for Automation*, Ipoh, Malaysia, pp. 226- 233, 16-18 July, 1999.
3. Image reconstruction of particle/droplet concentration profiles using optical tomography, S.Ibrahim, R.G. Green, K. Dutton, R. Abdul Rahim, K.Evans & A. Goude, *Proc. World Engineering Congress 1999*, pp. 171-177, Kuala Lumpur, Malaysia, 1999.
4. Process tomography using a hybrid optical fibre-lens system, S.Ibrahim, R.G. Green, K. Dutton, R. Abdul Rahim & B. Naylor, *Proc. Instrument Asia '99*, Singapore, 1-3 December, 1999.
5. An integrated optical fibre-lens system for tomography, S.Ibrahim, R.G. Green, K. Dutton, K.Evans & B. D. Naylor, *Proc. International Conference on Sensors and Transducers*, Birmingham, 16-17 February 2000.
6. Modelling to optimise the design of optical tomography systems for process measurement, S.Ibrahim, R.G. Green, K. Dutton & R. Abdul Rahim, *Proc. International Symposium on Process Tomography*, Jurata, Poland, 18-19 May, 2000.
7. Modelling optical fibre lens for process tomography, S.Ibrahim, R.G. Green, B. Naylor, N. Ramli & R. Abdul Rahim, *Proc. International Symposium on Process Tomography*, Jurata, Poland, 18-19 May, 2000.
8. Optical tomography for multi-phase flow, S.Ibrahim, R.G. Green, K. Dutton & R. Abdul Rahim, *Proc. International Symposium on Process Tomography*, Jurata, Poland, 18-19 May, 2000.

9. Optical tomography for concentration and velocity profiles in two component flows, S. Ibrahim, R.G. Green & K Dutton, *Proc. EOS/SPIE on Applied Photonics*, Glasgow, UK, 22 - 25 May, 2000.
10. Optical fibre sensors for flow measurement, S. Ibrahim, R.G. Green & K Dutton, *Proc. EOS/SPIE on Applied Photonics*, Glasgow, UK, 22 - 25 May, 2000.
11. Optical fibre sensing arrays for visualisation of two-phase flow: a design study, S.Ibrahim, R.G. Green, K. Evans, K. Dutton & A. Goude, *Proc. 9th International Symposium on Flow Visualisation*, Edinburgh, UK, 22 - 25 August, 2000.
12. Flow visualisation using optical tomography, S.Ibrahim, R.G. Green, K. Evans & K. Dutton, *Proc. 9th International Symposium on Flow Visualisation*, Edinburgh, UK, 22 - 25 August, 2000.
13. Optical tomography for process measurement and control, S.Ibrahim, R.G. Green, K. Dutton, K.Evans & R. Abdul Rahim, *Proc. UKACC International Conference on CONTROL 2000*, Cambridge, 4-7 September, 2000.
14. Optical fibre sensors for measurement of gas bubbles in water using tomographic techniques, S.Ibrahim, R.G. Green, K. Dutton & K. Evans, *Proc. Applied Optics and Opto-Electronics Conference*, Loughborough, 17-21 September, 2000.
15. A cross-correlation flowmeter using optical fibre sensors for velocity measurement in a hydraulic conveyor, S.Ibrahim, R.G. Green, K. Dutton & K. Evans, *Proc. Applied Optics and Opto-Electronics Conference*, Loughborough, 17-21 September, 2000.
16. Application of optical tomography in industrial process control system, S.Ibrahim, R.G. Green, K. Dutton & R. Abdul Rahim, *Proc. TENCON 2000*, Kuala Lumpur, 25-27 September, 2000, Malaysia.

Appendix A Results of LYGBP using the path length model

This section presents results obtained using modelling for several types of projection systems using the path length model. The results are divided into several parts :-

- (a) Results for two rectilinear projections are shown in section A.1.
- (b) Results for the three 120° rectilinear projections are shown in section A.2.
- (c) Results for four fan-beam projections are shown in section A.3.

A.1 Results for two rectilinear projections system

In this section the results of implementing LYGBP are presented for the two rectilinear projection system for the same four flow models as in sections 3.10.1 and 3.10.2. The grey level plots of the single pixel flow, two pixels flow, half flow and full flow models using the LYGBP algorithm are shown in Figures A.1a, A.1b, A.1c and A.1d respectively.

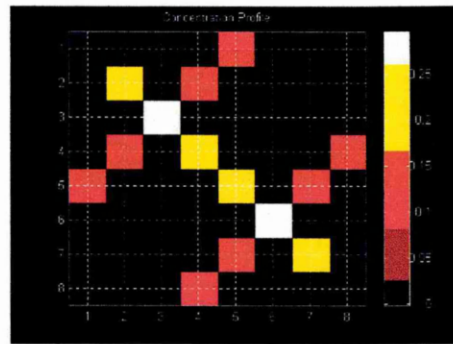
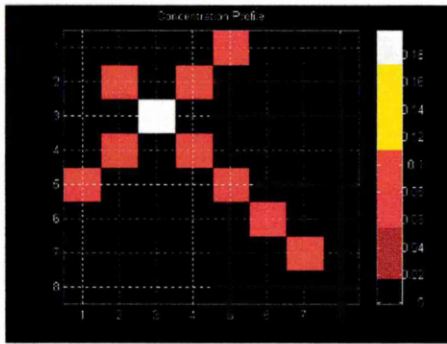


Figure A.1a LYGBP for two rectilinear projections: single pixel flow model

Figure A.1b LYGBP for two rectilinear projections: two pixels flow model

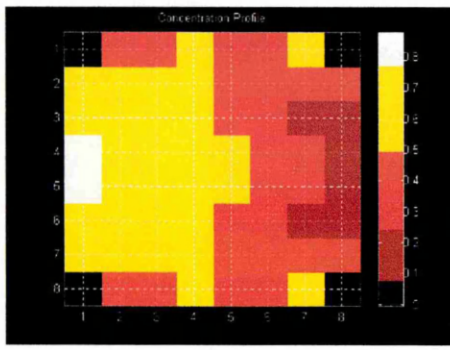


Figure A.1c LYGBP for two rectilinear projections: half flow model

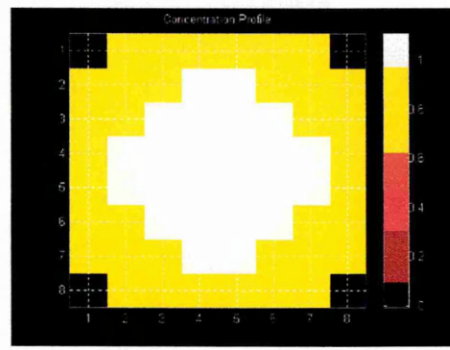


Figure A.1d LYGBP for two rectilinear projections: full flow model

A.2 Results for a combination of a combination of one orthogonal and two rectilinear projections system

In this section the results of implementing LYGBP are presented for a combination of one orthogonal and two rectilinear rectilinear projections for the same four flow models as in section 3.10.1. The grey level plots of the single pixel flow, two pixels flow, half flow and full flow models using the LYGBP algorithm are shown in Figures A.2a, A.2b, A.2c and A.2d respectively.

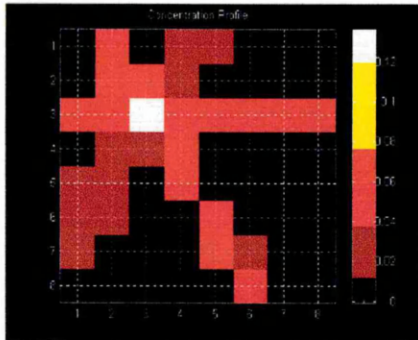


Figure A.2a LYGBP for three rectilinear projections: single pixel flow model

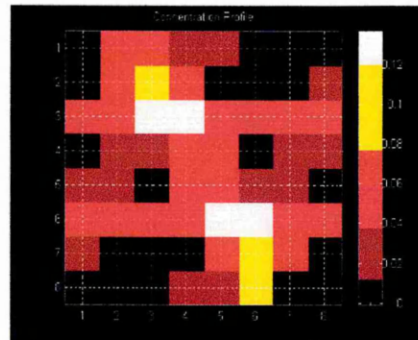


Figure A.2b LYGBP for three rectilinear projections: two pixels flow model

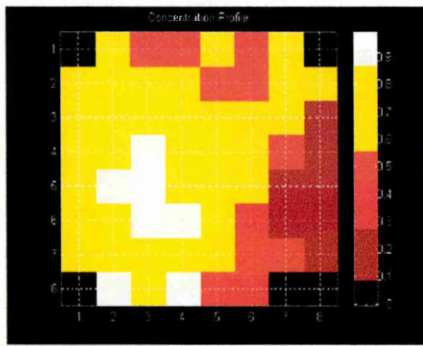


Figure A.2c LYGBP for three rectilinear projections: half flow model

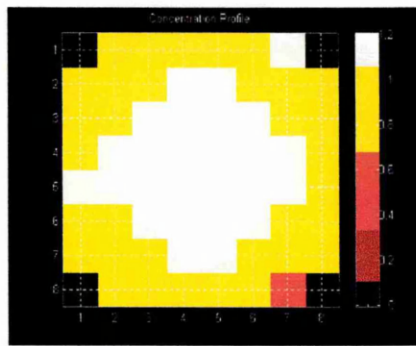


Figure A.2d LYGBP for three rectilinear projections: full flow model

A.3 Results of four fan-beam projections system

In this section the results of implementing LYGBP in the case of four fan-beam projection system are presented for the same four flow models as in sections 3.10.1 and 3.10.2. The grey level plots of the single pixel flow, two pixels flow, half flow and full flow models using the LYGBP algorithm are shown in Figures A.3a, A.3b, A.3c and A.3d respectively.

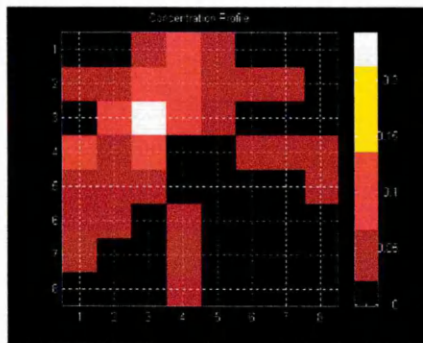


Figure A.3a LYGBP for four fan-beam projections: single pixel flow model

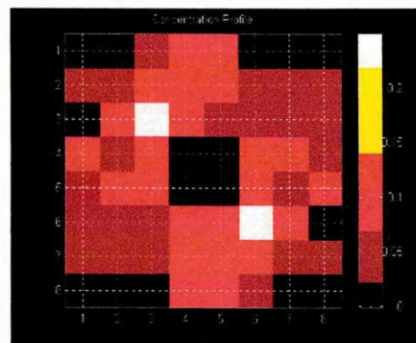


Figure A.3b LYGBP for four fan-beam projections: two pixels flow model

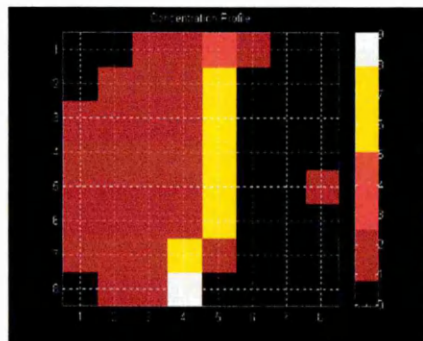


Figure A.3c LYGBP for four fan-beam projections: half flow model

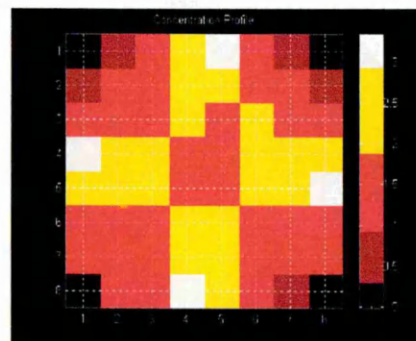


Figure A.3d LYGBP for four fan-beam projections: full flow model

Appendix B Results of LYGBP using the optical attenuation model

This section presents results for several types of projection systems using the optical attenuation model. The results are divided into several parts :-

- (a) Results for two rectilinear projections are presented in section B.1.
- (b) Results for a combination of one orthogonal and two rectilinear projections are presented in section B.2.
- (c) Results for four fan-beam projections are presented in section B.3.

B.1 Results for two rectilinear projections system

In this section the results of implementing LYGBP are presented for the two rectilinear projections system for the same four flow models as in section 3.10.1. The grey level plots of the single pixel flow, two pixels flow, half flow and full flow models using the LYGBP algorithm are shown in Figures B.1a, B.1b, B.1c and B.1d respectively.

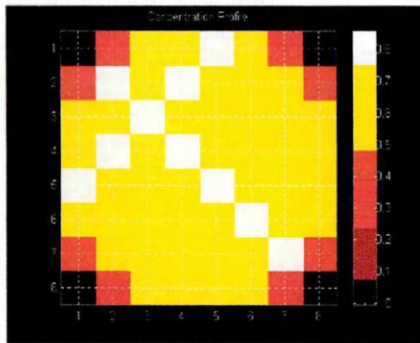


Figure B.1a LYGBP for two rectilinear projections: single pixel flow model

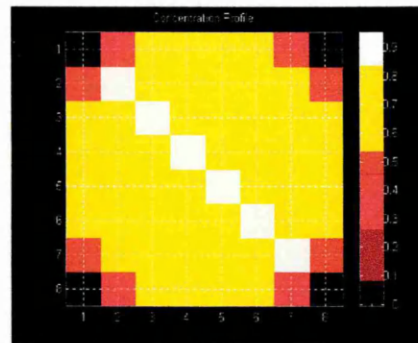


Figure B.1b LYGBP for two rectilinear projections: two pixels flow model

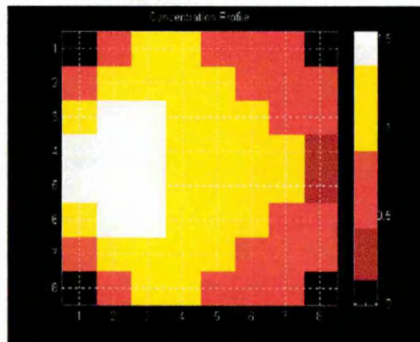


Figure B.1c LYGBP for two rectilinear projections: half flow model

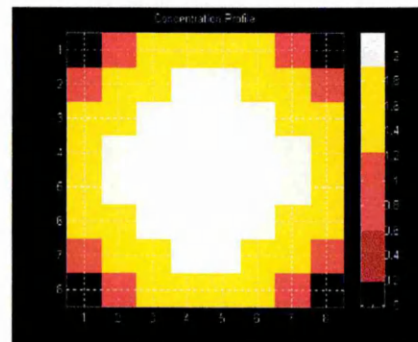


Figure B.1d LYGBP for two rectilinear projections: full flow model

B.2 Results for a combination of a combination of one orthogonal and two rectilinear projections system

In this section the results of implementing LYGBP are presented for a combination of one orthogonal and two rectilinear projections system in the case of the optical attenuation model for the same four flow models as in section 3.10.1. The grey level plots of the single pixel flow, two pixels flow, half flow and full flow models using the LYGBP algorithm are shown in Figures B.2a, B.2b, B.2c and B.2d respectively.

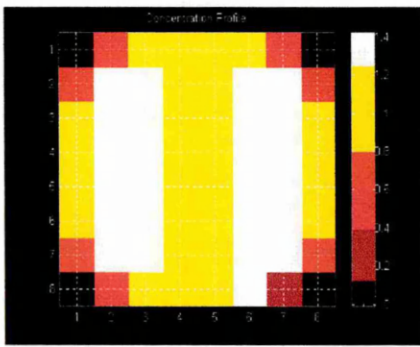


Figure B.2a LYGBP for a combination of one orthogonal and two rectilinear projections: single pixel flow model

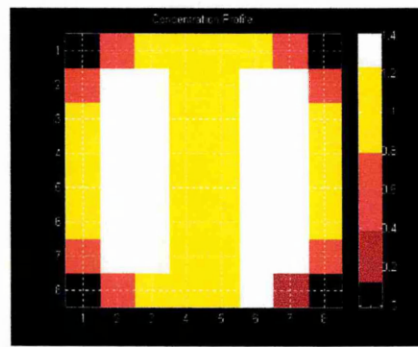


Figure B.2b LYGBP for a combination of one orthogonal and two rectilinear projections: two pixels flow model

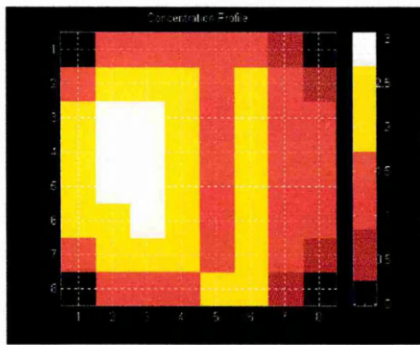


Figure B.2c LYGBP for a combination of one orthogonal and two rectilinear projections: half flow model

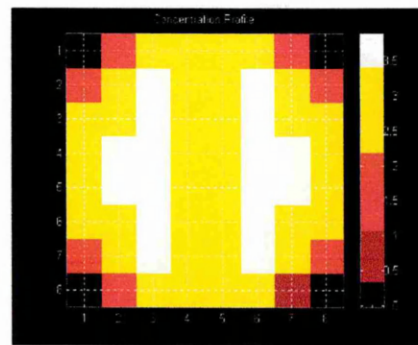


Figure B.2d LYGBP for a combination of one orthogonal and two rectilinear projections: full flow model

B.3 Results of four fan-beam projections system

In this section the results of implementing LYGBP are presented for the four fan-beam projections system for the same four flow models as in section 3.10.1. The grey level

plots of the single pixel flow, two pixels flow, half flow and full flow models using the LYGBP algorithm are shown in Figures B.3a, B.3b, B.3c and B.3d respectively.

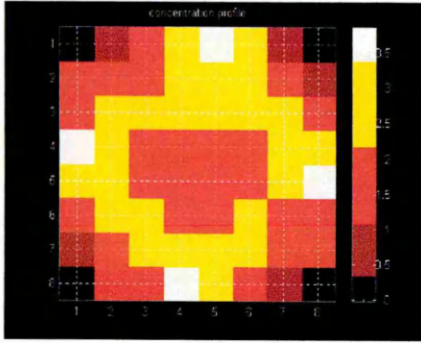


Figure B.3a LYGBP for four fan-beam projections: single pixel flow model

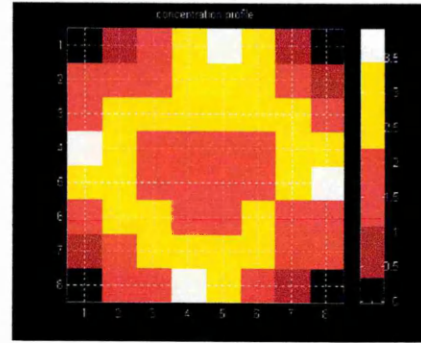


Figure B.3b LYGBP for four fan-beam projections: two pixels flow model

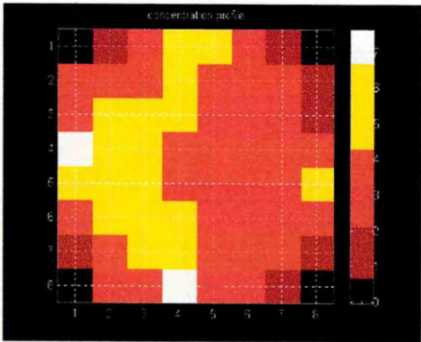


Figure B.3c LYGBP for four fan-beam projections: half flow model

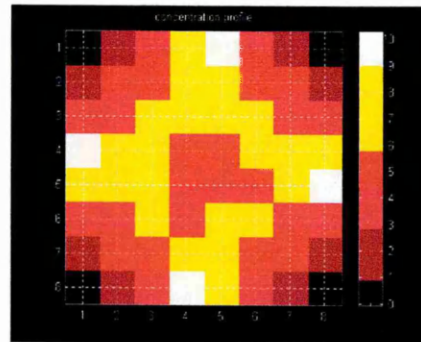


Figure B.3d LYGBP for four fan-beam projections: full flow model

Appendix C Results of LYGBP using a combination of optical attenuation model and signal processing

In this appendix, the results of LYGBP using a combination of optical attenuation model and signal processing are presented for :

- (a) two rectilinear projections (section C.1).
- (b) a combination of one orthogonal and two rectilinear projections (section C.2).
- (c) four fan-beam projections (section C.3).

C.1 Results for two rectilinear projections system

In this section the results of implementing LYGBP are presented for the two rectilinear projections system in the case of the combination of optical attenuation model and signal processing for the same four flow models as in section 3.10. The grey level plots of the single pixel flow, two pixels flow, half flow and full flow models using the LYGBP algorithm are shown in Figures C.1a, C.1b, C.1c and C.1d respectively.

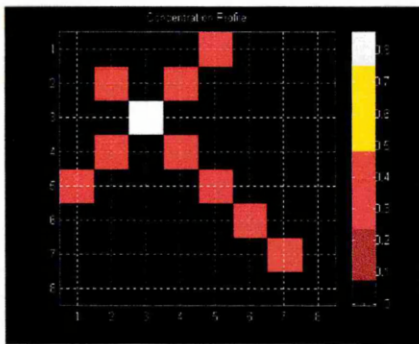


Figure C.1a LYGBP for two rectilinear projections: single pixel flow model

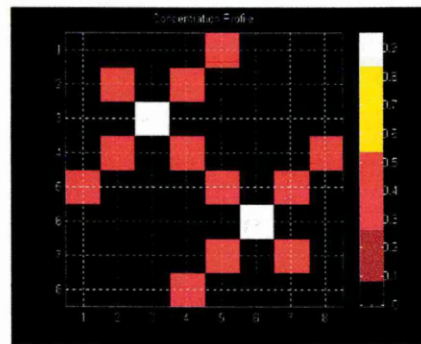


Figure C.1b LYGBP for two rectilinear projections: two pixels flow model

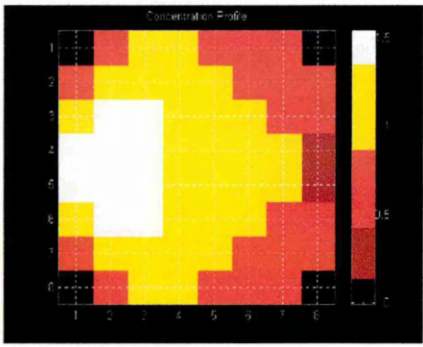


Figure C.1c LYGBP for two rectilinear projections: half flow model

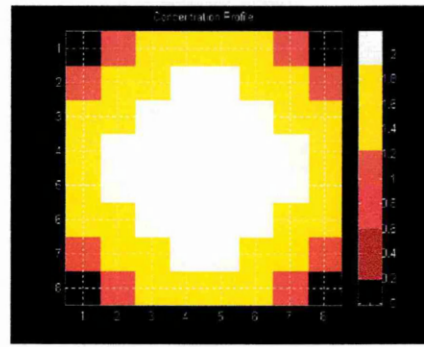


Figure C.1d LYGBP for two rectilinear projections: full flow model

C.2 Results for a combination of one orthogonal and two rectilinear projections system

In this section the results of implementing LYGBP are presented for a combination of one orthogonal and two rectilinear projections system in the case of the combination of optical attenuation model and signal processing for the same four flow models as in section 3.10.1. The grey level plots of the single pixel flow, two pixels flow, half flow and full flow models using the LYGBP algorithm are shown in Figures C.2a, C.2b, C.2c and C.2d respectively.

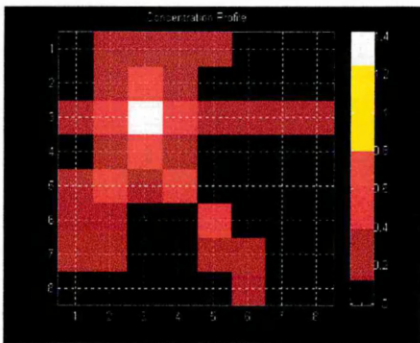


Figure C.2a LYGBP for a combination of one orthogonal and two rectilinear projections: single pixel flow model

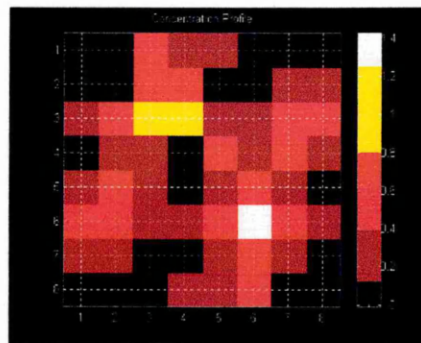


Figure C.2b LYGBP for a combination of one orthogonal and two rectilinear projections: two pixels flow model

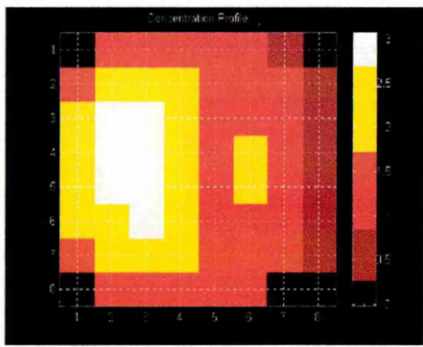


Figure C.2c LYGBP for a combination of one orthogonal and two rectilinear projections: half flow model

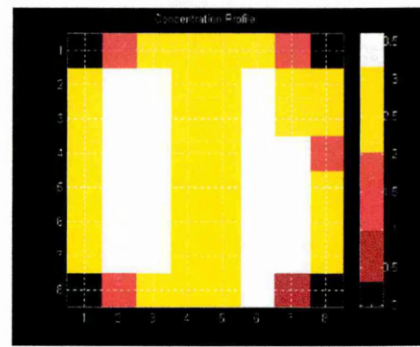


Figure C.2d LYGBP for a combination of one orthogonal and two rectilinear projections: full flow model

C.3 Results for four fan-beam projections system

In this section the results of implementing LYGBP are presented for the four fan-beam projections system in the case of the combination of optical attenuation model and electronic measurements for the same four flow models as in section 3.10.1. The grey level plots of the single pixel flow, two pixels flow, half flow and full flow models using the LYGBP algorithm are shown in Figures C.3a, C.3b, C.3c and C.3d respectively.

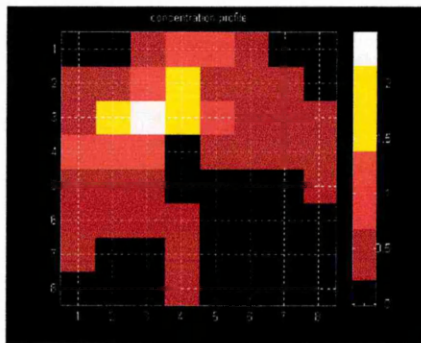


Figure C.3a LYGBP for four fan-beam projections: single pixel flow model

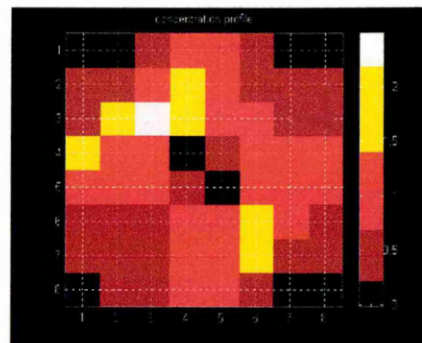


Figure C.3b LYGBP for four fan-beam projections: two pixels flow model

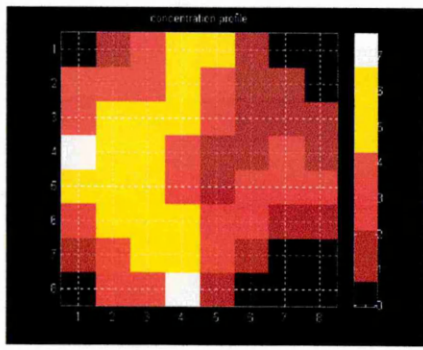


Figure C.3c LYGBP for four fan-beam projections: half flow model

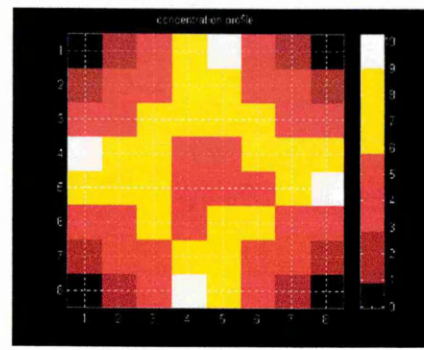


Figure C.3d LYGBP for four fan-beam projections: full flow model

Appendix D Tables of estimated reconstruction errors for two pixels flow, half flow and full flow models

The complete set of results for the path length modelling for the two pixels flow model is shown in Table D.1.

<i>Projections</i>	<i>Algorithm</i>	<i>No. of Sensors</i>	<i>Error % (no threshold)</i>	<i>Error % ($Th > 0.5 \times peak$)</i>
2 Orthogonal	LYGBP	16	688	100
2 Orthogonal	Hybrid	16	100	100
2 Rectilinear	LYGBP	22	267.6	130.1
2 Rectilinear	Hybrid	22	0	0
2 Rectilinear/2 Orthogonal	LYGBP	38	374.3	0
2 Rectilinear/2 Orthogonal	Hybrid	38	0	0
1 Orthogonal/2 Rectilinear	LYGBP	24	802.7	215.5
1 Orthogonal/2 Rectilinear	Hybrid	24	100	100
3 fan-beam	LYGBP	36	412.3	46.5
4 fan-beam	LYGBP	48	716.3	51.3

Table D.1 Estimated reconstruction errors: path length model

The complete set of results for the optical attenuation modelling for the two pixels flow model is shown in Table D.2.

<i>Projections</i>	<i>Algorithm</i>	<i>No. of Sensors</i>	<i>Error % (no threshold)</i>	<i>Error % ($Th > 0.5 \times peak$)</i>
2 Orthogonal	LYGBP	16	2396.7	2263.9
2 Orthogonal	Hybrid	16	100	100
2 Rectilinear	LYGBP	22	2008.8	1881.8
2 Rectilinear	Hybrid	22	0	0
2 Rectilinear/2 Orthogonal	LYGBP	38	1961	1802.6
2 Rectilinear/2 Orthogonal	Hybrid	38	0	0
1 Orthogonal/2 Rectilinear	LYGBP	24	2175.1	2017.8
1 Orthogonal/2 Rectilinear	Hybrid	24	91	91
3 fan-beam	LYGBP	36	1350.5	756.8
4 fan-beam	LYGBP	48	1551.8	1200

Table D.2 Estimated reconstruction errors: optical attenuation model

The complete set of results for the combination of optical attenuation model and signal conditioning for the two pixels flow model is shown in Table D.3.

<i>Projections</i>	<i>Algorithm</i>	<i>No. of Sensors</i>	<i>Error % (no threshold)</i>	<i>Error % (Th > 0.5 x peak)</i>
2 Orthogonal	LYGBP	16	722.7	722.7
2 Orthogonal	Hybrid	16	100	100
2 Rectilinear	LYGBP	22	286.8	129
2 Rectilinear	Hybrid	22	0	0
2 Rectilinear/ 2 Orthogonal	LYGBP	38	403.7	-11.5
2 Rectilinear/ 2 Orthogonal	Hybrid	38	0	0
1 Orthogonal/ 2 Rectilinear	LYGBP	24	887.6	396.8
1 Orthogonal/ 2 Rectilinear	Hybrid	24	-14.1	-14.1
3 fan-beam	LYGBP	36	695.7	398
4 fan-beam	LYGBP	48	933.7	322.4

Table D.3 Estimated reconstruction errors: combination of optical attenuation model and signal conditioning

The complete set of results for the path length modelling for the half flow model is shown in Table D.4.

<i>Projections</i>	<i>Algorithm</i>	<i>No. of Sensors</i>	<i>Error % (no threshold)</i>	<i>Error % Th > 0.5 x peak</i>
2 Orthogonal	LYGBP	16	3.5	-25.3
2 Orthogonal	Hybrid	16	- 22.4	- 25.3
2 Rectilinear	LYGBP	22	7.4	-22.3
2 Rectilinear	Hybrid	22	-31.1	-37.1
2 Rectilinear/ 2 Orthogonal	LYGBP	38	17.5	-21.8
2 Rectilinear/ 2 Orthogonal	Hybrid	38	- 19.6	- 25.3
1 Orthogonal/ 2 Rectilinear	LYGBP	24	26.2	11.8
1 Orthogonal/ 2 Rectilinear	Hybrid	24	- 22.2	- 25.1
3 fan-beam	LYGBP	36	23.1	-60.9
4 fan-beam	LYGBP	48	63.0	-81.0

Table D.4 Estimated reconstruction errors: path length model

The complete set of results for the optical attenuation modelling for the half flow model is shown in Table D.5.

<i>Projections</i>	<i>Algorithm</i>	<i>No. of Sensors</i>	<i>Error % (no threshold)</i>	<i>Error % (Th > 0.5 x peak)</i>
2 Orthogonal	LYGBP	16	30.2	16.1
2 Orthogonal	Hybrid	16	-19.1	-23.9
2 Rectilinear	LYGBP	22	40	30.7
2 Rectilinear	Hybrid	22	-21	-25.7
2 Rectilinear/ 2 Orthogonal	LYGBP	38	44.1	35
2 Rectilinear/ 2 Orthogonal	Hybrid	38	-14.7	-19.7
1 Orthogonal/ 2 Rectilinear	LYGBP	24	17.4	2.5
1 Orthogonal/ 2 Rectilinear	Hybrid	24	-30.8	-36
3 fan-beam	LYGBP	36	-15	-60.3
4 fan-beam	LYGBP	48	-7.7	-50.1

Table D.5 Estimated reconstruction errors: optical attenuation model

The complete set of results for the combination of optical attenuation model and signal conditioning for the half flow model is shown in Table D.6.

<i>Projections</i>	<i>Algorithm</i>	<i>No. of Sensors</i>	<i>Error % (no threshold)</i>	<i>Error % (Th > 0.5 × peak)</i>
2 Orthogonal	LYGBP	16	30.2	16.1
2 Orthogonal	Hybrid	16	-19.1	-23.9
2 Rectilinear	LYGBP	22	37.9	22.1
2 Rectilinear	Hybrid	22	-16.4	16.4
2 Rectilinear/ 2 Orthogonal	LYGBP	38	40.1	14.8
2 Rectilinear/ 2 Orthogonal	Hybrid	38	-9.8	-9.8
1 Orthogonal/ 2 Rectilinear	LYGBP	24	11.2	-18.1
1 Orthogonal/ 2 Rectilinear	Hybrid	24	- 26.6	- 29.6
3 fan-beam	LYGBP	36	-30.5	-75.9
4 fan-beam	LYGBP	48	-21.8	-54.2

Table D.6 Estimated reconstruction errors: combination of optical attenuation model and signal conditioning

The complete set of results for the path length modelling for the full flow model is shown in Table D.7.

<i>Projections</i>	<i>Algorithm</i>	<i>No. of Sensors</i>	<i>Error % (no threshold)</i>	<i>Error % (Th > 0.5 × peak)</i>
2 Orthogonal	LYGBP	16	- 22.4	- 25.3
2 Orthogonal	Hybrid	16	- 22.4	- 25.3
2 Rectilinear	LYGBP	22	-14.7	-14.7
2 Rectilinear	Hybrid	22	-14.7	-14.7
2 Rectilinear/ 2 Orthogonal	LYGBP	38	-17.9	-17.9
2 Rectilinear/ 2 Orthogonal	Hybrid	38	-17.9	-17.9
1 Orthogonal/ 2 Rectilinear	LYGBP	24	- 16.2	- 16.9
1 Orthogonal/ 2 Rectilinear	Hybrid	24	- 16.2	- 16.9
3 fan-beam	LYGBP	36	- 49.6	- 68.3
4 fan-beam	LYGBP	48	- 46.8	- 64.5

Table D.7 Estimated reconstruction errors: path length model

The complete set of results for the optical attenuation modelling for the full flow model is shown in Table D.8.

<i>Projections</i>	<i>Algorithm</i>	<i>No. of Sensors</i>	<i>Error % (no threshold)</i>	<i>Error % (Th > 0.5 × peak)</i>
2 Orthogonal	LYGBP	16	-21.3	-25.9
2 Orthogonal	Hybrid		-21.3	-25.9
2 Rectilinear	LYGBP	16	-20.5	-26.2
2 Rectilinear	Hybrid	22	-20.5	-26.2%
2 Rectilinear/ 2 Orthogonal	LYGBP	38	-20.9	-26.1
2 Rectilinear/ 2 Orthogonal	Hybrid	38	-20.9	-26.1
1 Orthogonal/ 2 Rectilinear	LYGBP	24	-26.8	-31.7
1 Orthogonal/ 2 Rectilinear	Hybrid		-26.8	-31.7
3 fan-beam	LYGBP	36	-53.1	-70.4
4 fan-beam	LYGBP	48	-48.1	-62.3

Table D.8 Estimated reconstruction errors: optical attenuation model

The complete set of results for the combination of optical attenuation model and signal conditioning for the full flow model is shown in Table D.9.

<i>Projections</i>	<i>Algorithm</i>	<i>No. of Sensors</i>	<i>Error % (no threshold)</i>	<i>Error % (Th > 0.5 × peak)</i>
2 Orthogonal	LYGBP	16	-7.7	-7.7
2 Orthogonal	Hybrid	16	-7.7	-7.7
2 Rectilinear	LYGBP	22	- 6.9	- 6.9
2 Rectilinear	Hybrid	22	- 6.9	- 6.9
2 Rectilinear/ 2 Orthogonal	LYGBP	38	-6.7	-6.7
2 Rectilinear/ 2 Orthogonal	Hybrid	38	-6.7	-6.7
1 Orthogonal/ 2 Rectilinear	LYGBP	24	-24.7	-26.6
1 Orthogonal/ 2 Rectilinear	Hybrid	24	-24.7	-26.6
3 fan-beam	LYGBP	36	-57.5	-85.8
4 fan-beam	LYGBP	48	-49.6	-69.3

Table D.9 Estimated reconstruction errors: combination of optical attenuation model and signal conditioning

Appendix E MATLAB program to reconstruct image using layergram back-projection algorithm

```
% 2 orthogonal projections
% Programme to determine the concentration profile and velocity of bubbles
% Based on path length
```

```
% Calculate the voltage of the sensor
% Voltage= 5 volts * beam length in pixel (3,3) / 100 mm
```

```
% Single pixel flow - for pixels other than 3,3 the voltage is 0
```

```
v6=0.5
v11=0.5
```

```
% Two pixels flow
v3=0.5
v6=0.5
v11=0.5
v14=0.5
```

```
% For Half Flow
v1=0.95
v2=1.55
v3=1.75
v4=1.9875
v5=1.9875
v6=1.75
v7=1.55
v8=0.95
v9=1.9
v10=3.1
v11=3.5
v12=3.975
v13=0
v14=0
v15=0
v16=0
```

```
% For Full Flow
v1=1.9
v2=3.1
v3=3.5
v4=3.975
v5=3.975
v6=3.5
v7=3.1
v8=1.9
v9=1.9
v10=3.1
v11=3.5
v12=3.975
v13=3.975
v14=3.5
v15=3.1
v16=1.9
```

```
s1=[0 0 0 0 0 0 0 0;  
0 0 0 0 0 0 0 0;  
0 0 0 0 0 0 0 0;  
0 0 0 0 0 0 0 0;  
0 0 0 0 0 0 0 0;  
0 0 0 0 0 0 0 0;  
0 0 0 0 0 0 0 0;  
0 0 (9/74.4) (10/84) (10/84) (9/74.4) 0 0];
```

```
s2=[0 0 0 0 0 0 0 0;  
0 0 0 0 0 0 0 0;  
0 0 0 0 0 0 0 0;  
0 0 0 0 0 0 0 0;  
0 0 0 0 0 0 0 0;  
0 0 0 0 0 0 0 0;  
0 0 0 0 0 0 0 0;  
(1/18) (10/86.39) (10/100) (10/100) (10/100) (10/100) (10/86.39) (1/18);  
0 0 0 0 0 0 0 0];
```

```
s3=[0 0 0 0 0 0 0 0;  
0 0 0 0 0 0 0 0;  
0 0 0 0 0 0 0 0;  
0 0 0 0 0 0 0 0;  
0 0 0 0 0 0 0 0;  
(7/74.4) (10/100) (10/100) (10/100) (10/100) (10/100) (10/100) (7/74.4);  
0 0 0 0 0 0 0 0;  
0 0 0 0 0 0 0 0];
```

```
s4=[0 0 0 0 0 0 0 0;  
0 0 0 0 0 0 0 0;  
0 0 0 0 0 0 0 0;  
0 0 0 0 0 0 0 0;  
(9.5/84) (10/100) (10/100) (10/100) (10/100) (10/100) (10/100) (9.5/84);  
0 0 0 0 0 0 0 0;  
0 0 0 0 0 0 0 0;  
0 0 0 0 0 0 0 0];
```

```
s5=[0 0 0 0 0 0 0 0;  
0 0 0 0 0 0 0 0;  
0 0 0 0 0 0 0 0;  
(9.5/84) (10/100) (10/100) (10/100) (10/100) (10/100) (10/100) (9.5/84);  
0 0 0 0 0 0 0 0;  
0 0 0 0 0 0 0 0;  
0 0 0 0 0 0 0 0;  
0 0 0 0 0 0 0 0];
```

```
s6=[0 0 0 0 0 0 0 0;  
0 0 0 0 0 0 0 0;  
(7/74.4) (10/100) (10/100) (10/100) (10/100) (10/100) (10/100) (7/74.4);  
0 0 0 0 0 0 0 0;  
0 0 0 0 0 0 0 0;  
0 0 0 0 0 0 0 0;  
0 0 0 0 0 0 0 0;  
0 0 0 0 0 0 0 0];
```

s7=[0 0 0 0 0 0 0;
(1/18) (10/86.39) (10/100) (10/100) (10/100) (10/100) (10/86.39) (1/18);
0 0 0 0 0 0 0;
0 0 0 0 0 0 0;
0 0 0 0 0 0 0;
0 0 0 0 0 0 0;
0 0 0 0 0 0 0;
0 0 0 0 0 0 0];

s8=[0 0 (9/74.4) (10/84) (10/84) (9/74.4) 0 0;
0 0 0 0 0 0 0;
0 0 0 0 0 0 0;
0 0 0 0 0 0 0;
0 0 0 0 0 0 0;
0 0 0 0 0 0 0;
0 0 0 0 0 0 0;
0 0 0 0 0 0 0];

s9=[0 0 0 0 0 0 0 0;
0 0 0 0 0 0 0 0;
(9/74.4) 0 0 0 0 0 0 0;
(10/84) 0 0 0 0 0 0 0;
(10/84) 0 0 0 0 0 0 0;
(9/74.4) 0 0 0 0 0 0 0;
0 0 0 0 0 0 0 0;
0 0 0 0 0 0 0 0];

s10=[0 (1/18) 0 0 0 0 0 0;
0 (10/86.39) 0 0 0 0 0 0;
0 (10/100) 0 0 0 0 0 0;
0 (10/100) 0 0 0 0 0 0;
0 (10/100) 0 0 0 0 0 0;
0 (10/100) 0 0 0 0 0 0;
0 (10/86.39) 0 0 0 0 0 0;
0 (1/18) 0 0 0 0 0 0];

s11=[0 0 (7/74.4) 0 0 0 0 0;
0 0 (10/100) 0 0 0 0 0;
0 0 (10/100) 0 0 0 0 0;
0 0 (10/100) 0 0 0 0 0;
0 0 (10/100) 0 0 0 0 0;
0 0 (10/100) 0 0 0 0 0;
0 0 (10/100) 0 0 0 0 0;
0 0 (7/74.4) 0 0 0 0 0];

s12=[0 0 0 (9.5/84) 0 0 0 0;
0 0 0 (10/100) 0 0 0 0;
0 0 0 (10/100) 0 0 0 0;
0 0 0 (10/100) 0 0 0 0;
0 0 0 (10/100) 0 0 0 0;
0 0 0 (10/100) 0 0 0 0;
0 0 0 (10/100) 0 0 0 0;
0 0 0 (9.5/84) 0 0 0 0];

```
s13=[0 0 0 0 (9.5/84) 0 0 0;
0 0 0 0 (10/100) 0 0 0;
0 0 0 0 (10/100) 0 0 0;
0 0 0 0 (10/100) 0 0 0;
0 0 0 0 (10/100) 0 0 0;
0 0 0 0 (10/100) 0 0 0;
0 0 0 0 (10/100) 0 0 0;
0 0 0 0 (10/100) 0 0 0;
0 0 0 0 (9.5/84) 0 0 0];
```

```
s14=[0 0 0 0 0 (7/74.4) 0 0;
0 0 0 0 0 (10/100) 0 0;
0 0 0 0 0 (10/100) 0 0;
0 0 0 0 0 (10/100) 0 0;
0 0 0 0 0 (10/100) 0 0;
0 0 0 0 0 (10/100) 0 0;
0 0 0 0 0 (10/100) 0 0;
0 0 0 0 0 (10/100) 0 0;
0 0 0 0 0 (7/74.4) 0 0];
```

```
s15=[0 0 0 0 0 0 (1/18) 0;
0 0 0 0 0 0 (10/86.39) 0;
0 0 0 0 0 0 (10/100) 0;
0 0 0 0 0 0 (10/100) 0;
0 0 0 0 0 0 (10/100) 0;
0 0 0 0 0 0 (10/100) 0;
0 0 0 0 0 0 (10/86.39) 0;
0 0 0 0 0 0 (1/18) 0];
```

```
s16=[0 0 0 0 0 0 0 0;
0 0 0 0 0 0 0 0;
0 0 0 0 0 0 0 (9/74.4);
0 0 0 0 0 0 0 (10/84);
0 0 0 0 0 0 0 (10/84);
0 0 0 0 0 0 0 (9/74.4);
0 0 0 0 0 0 0 0;
0 0 0 0 0 0 0 0];
```

% Sum of product of voltage and area sensitivity

```
% Concentration=(s17*v17) + (s18*v18)+ (s19*v19) + (s4*v4) + (s5*v5)+(s6*v6)+(s7*v7) +(s8*v8)
% +(s9*v9)+(s10*v10)+(s11*v11)+(s12*v12)+(s13*v13)+(s14*v14)+(s15*v15)+(s16*v16)
```

% concentration profile for flow in pixel (3,3)

```
conc_33=[0 0 0.0470 0 0 0 0 0 0;
0 0 0.0500 0 0 0 0 0 0;
0.0470 0.0500 0.1000 0.0500 0.0500 0.0500 0.0500 0.0500 0.047;
0 0 0.0500 0 0 0 0 0 0;
0 0 0.0500 0 0 0 0 0 0;
0 0 0.0500 0 0 0 0 0 0;
0 0 0.0500 0 0 0 0 0 0;
0 0 0.0470 0 0 0 0 0 0];
```

% After thresholding > 0.5 x peak

```
th_33=[0 0 0 0 0 0 0 0 0;
0 0 0 0 0 0 0 0 0;
0 0 0.1 0 0 0 0 0 0;
0 0 0 0 0 0 0 0 0];
```

```

0 0 0 0 0 0 0 0;
0 0 0 0 0 0 0 0;
0 0 0 0 0 0 0 0;
0 0 0 0 0 0 0 0];

```

% Concentration profile for pixels (3,3) and (6,6)

```

conc_33_66=[0 0 0.0470 0 0 0.0470 0 0;
0 0 0.0500 0 0 0.0500 0 0;
0.0470 0.0500 0.1000 0.0500 0.0500 0.1000 0.0500 0.0470;
0 0 0.0500 0 0 0.0500 0 0;
0 0 0.0500 0 0 0.0500 0 0;
0.0470 0.0500 0.1000 0.0500 0.0500 0.1000 0.0500 0.0470;
0 0 0.0500 0 0 0.0500 0 0;
0 0 0.0470 0 0 0.0470 0 0];

```

% concentration profile for half flow

```

conc_half=[0 0.1722 0.4442 0.5626 0.1131 0.1149 0 0;
0.0861 0.5383 0.5050 0.5525 0.1550 0.1550 0.1794 0.0861;
0.3945 0.4850 0.5250 0.5725 0.1750 0.1750 0.1750 0.1647;
0.4510 0.5088 0.5488 0.5963 0.1988 0.1988 0.1988 0.2248;
0.4510 0.5088 0.5488 0.5963 0.1988 0.1988 0.1988 0.2248;
0.3945 0.4850 0.5250 0.5725 0.1750 0.1750 0.1750 0.1647;
0.0861 0.5383 0.5050 0.5525 0.1550 0.1550 0.1794 0.0861;
0 0.1722 0.4442 0.5626 0.1131 0.1149 0 0];

```

(5/0.5963)*conc_half

```

conc_halfa=[0 1.4439 3.7246 4.7174 0.9483 0.9634 0 0;
0.7220 4.5137 4.2344 4.6327 1.2997 1.2997 1.5043 0.7220;
3.3079 4.0667 4.4021 4.8004 1.4674 1.4674 1.4674 1.3810;
3.7817 4.2663 4.6017 5.0000 1.6669 1.6669 1.6669 1.8850;
3.7817 4.2663 4.6017 5.0000 1.6669 1.6669 1.6669 1.8850;
3.3079 4.0667 4.4021 4.8004 1.4674 1.4674 1.4674 1.3810;
0.7220 4.5137 4.2344 4.6327 1.2997 1.2997 1.5043 0.7220;
0 1.4439 3.7246 4.7174 0.9483 0.9634 0 0];

```

% concentration profile for full flow

```

conc_full=[0 0.1722 0.5591 0.6757 0.6757 0.5591 0.1722 0;
0.1722 0.7177 0.6600 0.7075 0.7075 0.6600 0.7177 0.1722;
0.5591 0.6600 0.7000 0.7475 0.7475 0.7000 0.6600 0.5591;
0.6757 0.7075 0.7475 0.7950 0.7950 0.7475 0.7075 0.6757;
0.6757 0.7075 0.7475 0.7950 0.7950 0.7475 0.7075 0.6757;
0.5591 0.6600 0.7000 0.7475 0.7475 0.7000 0.6600 0.5591;
0.1722 0.7177 0.6600 0.7075 0.7075 0.6600 0.7177 0.1722;
0 0.1722 0.5591 0.6757 0.6757 0.5591 0.1722 0];

```

% reciprocal of the full flow matrix

```

r = [ 0 5.8072 1.7886 1.4799 1.4799 1.7886 5.8072 0;
5.8072 1.3933 1.5152 1.4134 1.4134 1.5152 1.3933 5.8072;
1.7886 1.5152 1.4286 1.3378 1.3378 1.4286 1.5152 1.7886;
1.4799 1.4134 1.3378 1.2579 1.2579 1.3378 1.4134 1.4799;
1.4799 1.4134 1.3378 1.2579 1.2579 1.3378 1.4134 1.4799;
1.7886 1.5152 1.4286 1.3378 1.3378 1.4286 1.5152 1.7886;
5.8072 1.3933 1.5152 1.4134 1.4134 1.5152 1.3933 5.8072;
0 5.8072 1.7886 1.4799 1.4799 1.7886 5.8072 0];

```

```

% r.*conc_33

filter_33=[0    0 0.0841    0    0    0    0    0;
            0    0 0.0758    0    0    0    0 0;
            0.0841 0.0758 0.1429 0.0669 0.0669 0.0714 0.0758 0.0841;
            0    0 0.0669    0    0    0    0 0;
            0    0 0.0669    0    0    0    0 0;
            0    0 0.0714    0    0    0    0 0;
            0    0 0.0758    0    0    0    0 0;
            0    0 0.0841    0    0    0    0 0];

% r.*conc_33_66

filter_33_66=[0    0 0.0841    0    0 0.0841    0 0;
              0    0 0.0758    0    0 0.0758    0 0;
              0.0841 0.0758 0.1429 0.0669 0.0669 0.1429 0.0758 0.0841;
              0    0 0.0669    0    0 0.0669    0 0;
              0    0 0.0669    0    0 0.0669    0 0;
              0.0841 0.0758 0.1429 0.0669 0.0669 0.1429 0.0758 0.0841;
              0    0 0.0758    0    0 0.0758    0 0;
              0    0 0.0841    0    0 0.0841    0 0];

filter_half=[0 1.0000 0.7945 0.8326 0.1674 0.2055    0 0;
             0.5000 0.7500 0.7652 0.7809 0.2191 0.2349 0.2500 0.5;
             0.7056 0.7349 0.7500 0.7659 0.2341 0.2500 0.2652 0.2946;
             0.6674 0.7191 0.7342 0.7501 0.2501 0.2660 0.2810 0.3327;
             0.6674 0.7191 0.7342 0.7501 0.2501 0.2660 0.2810 0.3327;
             0.7056 0.7349 0.7500 0.7659 0.2341 0.2500 0.2652 0.2946;
             0.5000 0.7500 0.7652 0.7809 0.2191 0.2349 0.2500 0.5;
             0 1.0000 0.7945 0.8326 0.1674 0.2055    0 0];

for i=1:8
for j=1:8
Vxy(i,j)=0;
end
end

for i=1:8
for j=1:8
Vxy(i,j)=conc_33_66(i,j);
end
end

figure
% surfc(Vxy);
imagesc(Vxy);
caxis([0 1])

colormap(hot)
hold on
colorbar

```

```
grid, title('Concentration Profile')
```

```
% Cross-correlation programme
```

```
L=length(u);  
if length(y)~=L,  
error('kxcorr - arguments are not of the same length')  
end  
for i=1:L  
    if i==1,  
        ushft=u;  
    else  
        ushft=[ushft(L,1);ushft(1:L-1,1)];  
    end  
    x(i)=sum(y.*ushft)/L;
```

```
% dimensions of y and ushft must agree
```

```
end
```

```
plot(x)  
x=x';  
[z,it]=max(x)
```

```
title ('Cross correlogram')  
xlabel ('Parametric time shift')  
ylabel ('Cross correlation coefficient')
```

```
% 100 Hz  
v1=0.03/(it*0.01)
```

```
% 500 Hz  
v2=0.03/(it*0.002)
```

Appendix F C program for hybrid reconstruction algorithm

```
#include <stdio.h>
#include <conio.h>

#define SIZE 8
#define N_DIAGONALS ((SIZE * 2) - 1)
#define N_SENSORS SIZE * 2 + N_DIAGONALS
#define N_PROJECTIONS 3

int sensor[N_SENSORS];
int sensor_map[N_SENSORS][SIZE][SIZE];
int pixel[SIZE][SIZE];

void main()
{
    int i,j,k,l;
    int s;

    FILE *tomograf;
    tomograf=fopen("tomograf.dat","w");

    clrscr();
    /* Generate sensitivity maps */
    /* horiz sensor first */
    for(s = 0; s < SIZE; s++)
    {
        for (i=0;i<SIZE;i++)
        {
            for(j=0;j<SIZE;j++)
            {
                for(l=0;l<((SIZE*2)-1);l++)
                {
                    if ( i == s)
                        sensor_map[s][j][i] = 1;
                    else
                        sensor_map[s][j][i] = 0;
                }
            }
        }
    }

    /* Now vertical sensors*/
    for(s = SIZE; s < 2 * SIZE; s++)
    {
        for (i=0;i<SIZE;i++)
        {
            for(j=0;j<SIZE;j++)
            {
                for(l=0;l<((SIZE*2)-1);l++)
                {
                    if ( j == s - SIZE)
                        sensor_map[s][j][i] = 1;
                    else
                        sensor_map[s][j][i] = 0;
                }
            }
        }
    }
}
```



```

sensor[26] = 1;
sensor[27] = 1;
sensor[28] = 1;
sensor[29] = 1;
sensor[30] = 0;
sensor[31]=1;
sensor[32]=1;
sensor[33]=1;
sensor[34]=1;
sensor[35]=1;
sensor[36]=1;
sensor[37]=1;
sensor[38]=1;

for( j = 0; j < SIZE; j++)
{
    for( i = 0; i < SIZE; i++)
    {
        /* printf("Doing pixel %d,%d\n",i,j);
           printf("Looking at sensors %d and %d\n",i,j+SIZE);
        */
        if ((sensor[i] == 0) || (sensor[j+SIZE] == 0) || (sensor[SIZE*2+i+j] == 0 ))
        {
            pixel[i][j] = 0;
            /* printf("It's zero\n"); */
        }
        else
        {
            /*
                printf("Sensor %d, value = %d, map = %d\n",i,sensor[i],
sensor_map[i][j][i]);
                printf("Sensor %d, value = %d, map =
%d\n",j+SIZE,sensor[j+SIZE], sensor_map[j+SIZE][j][i]);
            */

            pixel[i][j] += sensor[i] * sensor_map[i][j][i];
            pixel[i][j] += sensor[j+SIZE] * sensor_map[j+SIZE][j][i];
            pixel[i][j] += sensor[SIZE*2+i+j]* sensor_map[SIZE*2+i+j][j][i];
            /* Not including diagonal in calculation ...Yet. */
        }
    }
}

printf("\nPixel map\n");

for(j = 0; j < SIZE; j++)
{
    for( i = 0; i < SIZE; i++)
    {
        printf("%d ",pixel[i][j]);

    }
    printf("\n");
}
}

```